

*Advances in Meteorology*

# Large-Scale Dynamics, Anomalous Flows, and Teleconnections 2018

Special Issue Editor in Chief: Anthony R. Lupo

Guest Editors: Andrew D. Jensen, Igor I. Mokhov, and Yafei Wang





---

**Large-Scale Dynamics, Anomalous Flows,  
and Teleconnections 2018**

Advances in Meteorology

---

**Large-Scale Dynamics, Anomalous Flows,  
and Teleconnections 2018**

Special Issue Editor in Chief: Anthony R. Lupo

Guest Editors: Andrew D. Jensen, Igor I. Mokhov, and Yafei Wang



---

Copyright © 2019 Hindawi. All rights reserved.

This is a special issue published in “Advances in Meteorology.” All articles are open access articles distributed under the Creative Commons Attribution License, which permits unrestricted use, distribution, and reproduction in any medium, provided the original work is properly cited.

## Editorial Board

José Antonio Adame, Spain  
Cesar Azorin-Molina, Sweden  
Marina Baldi, Italy  
Abderrahim Bentamy, France  
Stefania Bonafoni, Italy  
Gabriele Buttafuoco, Italy  
Dominique Carrer, France  
Annalisa Cherchi, Italy  
James Cleverly, Australia  
Roberto Coscarelli, Italy  
Panuganti CS Devara, India  
Alessia Di Gilio, Italy  
Paolo Di Girolamo, Italy  
Julio Diaz, Spain  
Stefano Dietrich, Italy  
Antonio Donateo, Italy  
Stefano Federico, Italy  
Enrico Ferrero, Italy  
Rossella Ferretti, Italy  
Helena A. Flocas, Greece  
Roberto Fraile, Spain  
Maria Ángeles García, Spain  
Herminia García Mozo, Spain  
Eduardo García-Ortega, Spain

Giacomo Gerosa, Italy  
Luis Gimeno, Spain  
Jorge E. Gonzalez, USA  
Ismail Gultepe, Canada  
Rafiq Hamdi, Belgium  
Adel Hanna, USA  
Hiroyuki Hashiguchi, Japan  
Tareq Hussein, Jordan  
Pedro Jiménez-Guerrero, Spain  
George Kallos, Greece  
Harry D. Kambezidis, Greece  
Theodore Karacostas, Greece  
Nir Y. Krakauer, USA  
Hisayuki Kubota, Japan  
Saro Lee, Republic of Korea  
Ilan Levy, Israel  
Margarida L. R. Liberato, Portugal  
Gwo-Fong Lin, Taiwan  
Anthony R. Lupo, USA  
Paolo Madonia, Italy  
Andreas Matzarakis, Germany  
Nicholas Meskhidze, USA  
Mario M. Miglietta, Italy  
Takashi Mochizuki, Japan

Francisco Molero, Spain  
Panagiotis Nastos, Greece  
Brian R. Nelson, USA  
Efthymios I. Nikolopoulos, USA  
Giulia Pavese, Italy  
Kyaw T. Paw, USA  
Federico Porcù, Italy  
Olivier P. Prat, USA  
Sara C. Pryor, USA  
Budong Qian, Canada  
Philippe Ricaud, France  
Tomeu Rigo, Spain  
Filomena Romano, Italy  
Haydee Salmun, USA  
Pedro Salvador, Spain  
Francisco J. Tapiador, Spain  
Yoshihiro Tomikawa, Japan  
Tomoo Ushio, Japan  
Rogier Van Der Velde, Netherlands  
Francesco Viola, Italy  
Alastair Williams, Australia  
Olga Zolina, France

# Contents

---

## **Large-Scale Dynamics, Anomalous Flows, and Teleconnections 2018**

Anthony R. Lupo , Andrew D. Jensen, Igor I. Mokhov, and Yafei Wang  
Editorial (2 pages), Article ID 3934195, Volume 2019 (2019)

## **Investigation of Vorticity during Prevalent Winter Precipitation in Iran**

Iman Rousta , Farshad Javadizadeh , Fatemeh Dargahian, Haraldur Ólafsson, Amin Shiri-Karimvandi, Sayed Hossein Vahedinejad, Mehdi Doostkamian, Edgar Ricardo Monroy Vargas, and Anayat Asadolahi  
Research Article (13 pages), Article ID 6941501, Volume 2018 (2019)

## **Links between Temperature Biases and Flow Anomalies in an Ensemble of CNRM-CM5.1 Global Climate Model Historical Simulations**

O. Lhotka  and A. Farda   
Research Article (10 pages), Article ID 4984827, Volume 2018 (2019)

## **A New Dynamical Index for India-Burma Trough**

Kui Liu, Jinlin Zha, Ruowen Yang , and Jilong Chen  
Research Article (10 pages), Article ID 5215093, Volume 2018 (2019)

## **Evaluating Linkages between Atmospheric Blocking Patterns and Heavy Rainfall Events across the North-Central Mississippi River Valley for Different ENSO Phases**

Jordan L. Rabinowitz , Anthony R. Lupo, and Patrick E. Guinan  
Research Article (7 pages), Article ID 1217830, Volume 2018 (2019)

## Editorial

# Large-Scale Dynamics, Anomalous Flows, and Teleconnections 2018

**Anthony R. Lupo** <sup>1</sup>, **Andrew D. Jensen**,<sup>2</sup> **Igor I. Mokhov**,<sup>3,4</sup> and **Yafei Wang**<sup>5</sup>

<sup>1</sup>*Atmospheric Science Program, School of Natural Resources, University of Missouri, 302 E. Anheuser Busch Natural Resources Building, Columbia, MO, USA*

<sup>2</sup>*Department of Mathematics and Meteorology, Northland College, Ashland, WI, USA*

<sup>3</sup>*A.M. Obukhov Institute of Atmospheric Physics, Russian Academy of Sciences, 3 Pyzhevsky, Moscow, Russia*

<sup>4</sup>*Department of Atmospheric Physics, Lomonosov Moscow State University, Moscow, Russia*

<sup>5</sup>*Chinese Academy of Meteorological Sciences, Beijing, China*

Correspondence should be addressed to Anthony R. Lupo; [lupoa@missouri.edu](mailto:lupoa@missouri.edu)

Received 8 November 2018; Accepted 11 November 2018; Published 10 January 2019

Copyright © 2019 Anthony R. Lupo et al. This is an open access article distributed under the Creative Commons Attribution License, which permits unrestricted use, distribution, and reproduction in any medium, provided the original work is properly cited.

The topic of large-scale dynamics, anomalous flows, and teleconnections (LDAT) continues to be of great interest to the weather and climate community, especially given recent changes in climate during the last few decades and projected climate changes [1]. The impact of climate change could be very complex, especially regarding its impacts on teleconnections (e.g., [1]), the occurrence and dynamics of severe weather events (e.g., [2]), or the occurrence and intensity of large-scale events associated with local temperature and precipitation variability such as blocking anticyclones. Additionally, research has shown that large-scale regional anomalies are associated with regional anomalies of radiatively important gasses such as water vapor or ozone or with the concentration of atmospheric aerosols.

Many recent studies continue to examine the behavior of teleconnective regimes in more detail than ever within various regions of the globe in order to understand how these might change in the near and far future. A better understanding of these phenomena and their local, regional, or global impacts will provide more information to the private and public sectors so that societies can be better prepared to meet their needs while minimizing their exposure to destructive phenomena.

Knowing the climatological and dynamic character of flow regimes that impact regional weather and climate is essential for long-range forecasting or constructing future scenarios. The study of I. Rousta et al. examined the nature

and distribution of atmospheric vorticity in the region of the Middle East and Asia during winter-season precipitation events occurring in Iran. Cluster analysis was used to identify the prevailing large-scale configuration of atmospheric pressure centers from 1961 to 2013 based on variables such as the occurrence of significant precipitation and vorticity at mandatory levels (1000, 850, 700, and 500 hPa). This study identified five different synoptic scenarios that were associated with more persistent precipitation events (low pressure over Iran and a strong Siberian High) as well as heavy precipitation events (high pressure over East Europe and low pressure over Iran). The latter scenario is similar to the flooding rains that occurred in the region in association with the strong blocking event that occurred over Eastern Europe and Western Russia during the summer of 2010. They also found that three of the patterns associated with winter precipitation events formed and decayed over the study region, while two of them originated outside the area. Additionally, they examined the dynamics that contributed to upward motions in these patterns.

It is of great importance that climate models should be evaluated based on their ability to simulate the general character of climate, as well as specific features of the general circulation. To this end, O. Lhotka and A. Farda investigated the relationship between flow anomalies and daily surface temperature and pressure biases in a climate model ensemble by using historical circulations and comparing them

to the National Oceanic and Atmospheric Administration (NOAA) Cooperative Institute for Research in Environmental Sciences (CIRES) twentieth-century reanalyses. The climate model used was the Centre National de Recherches Météorologiques (CNRM) Climate Model version 5.1 (CM5.1), and this model is part of the Coupled Model Intercomparison Project (CMIP). Three ensemble members were chosen for study with differing initial conditions using spatial resolution that is consistent with the reanalyses used. They found that, while the CNRM-CM5.1 model skillfully reproduces the general temperature patterns for the globe, this model has similar weaknesses to other CMIP models. The most relevant issues found in all three ensemble members are as follows: (a) warm (cold) biases in the South (North) Atlantic, (b) positive temperature and negative pressure biases in the South American and African upwelling regions, and (c) the frequency of zonal flow over North America resulting in warm temperature biases. Presumably, such temperature and pressure biases will be influential in the model's ability to simulate interannual variability.

In the observation and study of teleconnections, indexes are used to quantify the existence, phase, and intensity of the phenomenon in a simple and straightforward way using standard observations. Here, K. Liu et al. developed a dynamical index to quantify and understand the India-Burma Trough (IBT). Studying the IBT is important also to understand the behavior of Southeast Asian Monsoon over time. Additionally, the IBT is an important feature in providing moisture to societies that are impacted by this feature for agricultural production and drinking water. Their proposed index sums up vertical motions obtained from five pressure levels between 700 hPa and 500 hPa, inclusive, within the IBT geographic location. In order to obtain a positive number, the obtained value is multiplied by a negative one. They used the monthly Modern-Era Retrospective Analysis for Research and Application (MERRA) provided by the Goddard Earth Sciences Data and Information Services Center (GES DISC) from 1979 to 2012. As many studies of midlatitude cyclones demonstrate, the upward motion in the IBT region is associated with the advection or flux of vorticity and temperature. The new index, like others, also reflects the strength of the IBT and possesses an annual cycle. Changes in the strength of this index will also be the result of the strength and position of the synoptic patterns in adjacent regions.

Teleconnections and anomalous flows can be associated with extreme events on very local time and space scales. J. L. Rabinowitz et al. examined the correlation between atmospheric blocking occurring within the Pacific Ocean region and heavy rainfall for an agriculturally important region in the Midwest USA. Many authors have demonstrated the link between anomalous weather and blocking within the regions they impact and those areas up- and downstream of these events. While climate models project that the occurrence of blocking may not change appreciably in the future, such events will still be associated with extreme weather [1]. J. L. Rabinowitz et al. examined parameters such as block intensity, block size, block onset lead time, block duration, and

genesis location and found associations with heavy rainfall ( $>50.8 \text{ mm } 24 \text{ h}^{-1}$ ) in the mid-Mississippi River Valley since 1999. This study found that there was a greater propensity for Pacific Region blocking during La Nina years to be associated with heavy rainfall events in the study region. This is likely due to the impact of blocking on the storm track over this region. They also found that strong blocking events were associated with larger rainfalls. Additionally, blocking events that formed further west in the Pacific were associated with larger regional rainfalls.

In conclusion, these contributions to the topics examined in the LDAT series continue to provide insight into the unresolved issues related to large-scale meteorological phenomena. In doing so, the new information will be available to the operational community as they strive to provide improved forecast skill to the general public, as well as policy-makers.

## Conflicts of Interest

The editors declare that they have no conflicts of interest regarding the publication of this special issue.

## Acknowledgments

We would like to thank all the authors for their contributions to this special issue, as well as the reviewers for their comments, which help to make manuscripts stronger contributions. We would like to thank the Editorial Board for their continued support for this special issue series. The lead guest editor would like to thank the guest editors for their cooperation and hard work in making this special issue successful.

Anthony R. Lupo  
 Andrew D. Jensen  
 Igor I. Mokhov  
 Yafei Wang

## References

- [1] Intergovernmental Panel on Climate Change (IPCC), *Climate Change 2013: the Physical Scientific Basis: Contributions of Working Group I to the Fifth Assessment Report of the Intergovernmental Panel on Climate Change*, IPCC, Geneva, Switzerland, 2013, <http://www.ipcc.ch>.
- [2] Climate Science Special Report (CSSR), "Fourth National Climate Assessment (NCA4)," vol. 1, 2017, <https://science2017.globalchange.gov/>.

## Research Article

# Investigation of Vorticity during Prevalent Winter Precipitation in Iran

**Iman Rousta** <sup>1,2</sup>, **Farshad Javadizadeh** <sup>3</sup>, **Fatemeh Dargahian**,<sup>4</sup> **Haraldur Ólafsson**,<sup>5</sup> **Amin Shiri-Karimvandi**,<sup>6</sup> **Sayed Hossein Vahedinejad**,<sup>7</sup> **Mehdi Doostkamian**,<sup>6</sup> **Edgar Ricardo Monroy Vargas**,<sup>8</sup> and **Anayat Asadolahi**<sup>6</sup>

<sup>1</sup>Department of Geography, Yazd University, Yazd 8915818411, Iran

<sup>2</sup>Senior Researcher, Institute for Atmospheric Sciences, University of Iceland and Icelandic Meteorological Office (IMO), Bustadavegur 7, IS-108 Reykjavik, Iceland

<sup>3</sup>Department of Environment, Collage of Natural Resource, Bandar Abbas Branch, Islamic Azad University, Bandar Abbas, Iran

<sup>4</sup>Desert Research Division, Research Institute of Forests and Rangelands, Agricultural Research Education and Extension Organization (AREEO), Tehran, Iran

<sup>5</sup>Department of Physics, University of Iceland, Institute for Atmospheric Sciences and Icelandic Meteorological Office (IMO), Bustadavegur 7, IS-108 Reykjavik, Iceland

<sup>6</sup>Department of Geography, University of Zanjan, Zanjan 3879145371, Iran

<sup>7</sup>Department of Geography, University of Kharazmi, Tehran 1491115719, Iran

<sup>8</sup>Department of Civil Engineering, Universidad Catolica de Colombia, Bogotá, Colombia

Correspondence should be addressed to Iman Rousta; [irousta@yazd.ac.ir](mailto:irousta@yazd.ac.ir) and Farshad Javadizadeh; [javadizadeh2020@yahoo.com](mailto:javadizadeh2020@yahoo.com)

Received 20 February 2018; Revised 19 March 2018; Accepted 5 April 2018; Published 30 September 2018

Academic Editor: Andrew D. Jensen

Copyright © 2018 Iman Rousta et al. This is an open access article distributed under the Creative Commons Attribution License, which permits unrestricted use, distribution, and reproduction in any medium, provided the original work is properly cited.

In this study, precipitation data for 483 synoptic stations, and the U&V component of wind and HGT data for 4 atmospheric levels were respectively obtained from IRIMO and NCEP/NCAR databases (1961–2013). The precipitation threshold of 1 mm and a minimum prevalence of 50% were the criteria based on which the prevalent precipitation of Iran was identified. Then, vorticity of days corresponding to prevalent winter precipitation was calculated and, by performing cluster analysis, the representative days of vorticity were specified. The results showed that prevalent winter precipitation vorticity in Iran is related to the vorticity patterns of low pressure of Mediterranean-low pressure of Persian Gulf dual-core, low pressure closed of central Iran-high pressure of East Europe, Ural low pressure-Middle East High pressure, Saudi Arabia low pressure-Europe high pressure, and high-pressure belt of Siberia-low pressure of central Iran. At the same time, the most intense vorticity occurred when the climate of Iran was influenced by a massive belt pattern of Siberian high pressure-low pressure of central Iran. However, at the time of prevalent winter precipitation in Iran, an intense vorticity is drawn with the direction of Northeast and Northwest from the center of Iraq to the south of Iran.

## 1. Introduction

Changes in extreme weather and climate events have significant impacts and are among the most serious challenges to society in coping with a changing climate [1–9]. The most important factor in the formation and guidance of atmospheric systems is vorticity process [10–12]. In the middle latitudes, at the synoptic scale, the important dynamic properties are those which are related to rotating particles in the air [13]. Dessouky

and Jenkinson [14] and Jenkinson and Collison [15] are two examples of studies in different parts of the world focusing on the role of vorticity conditions and amount at different atmosphere levels in precipitation. Based on the general format of weather types identified by Lamb, Dessouky and Jenkinson investigated vorticity and the direction of flows in pressure systems producing severe storms in the UK, and systems producing drought and wet years in Egypt [14]. Jenkinson's method has been tested by many researchers in different areas

of the world. They showed that using this method can make it possible to identify weather types and quantitatively calculate their intensity and weakness. Since the convergence leads to upside movements, some studies have investigated vorticity advection, divergence, and vertical motions combined with high levels of atmosphere jet stream as an evidence for the development of surface low pressure [16–19]. In another study, Nakamura showed that high levels of jet stream simultaneously occur with divergence and relative positive vorticity advection [20]. Different case studies show that the presence and intensity of relative positive vorticity advection with the vertical arrangement of the wind caused by the jet stream changes provide favorable conditions for increasing vertical movements and uplink, and creating low surface pressure [21–23]. Vincent studied the development of cyclones in the South Pacific convergence zone using vorticity [24]. In another study, Wang examined the relative vorticity of ocean winds and its impact on the development of tropical cyclones in the South China Sea. He concluded that the winter tropical cyclone genesis in the South China Sea happens due to vertical shear of the horizontal winds and low-level atmospheric vorticity [25]. In other studies around the world, Alpert et al. investigated the horizontal distribution and the vertical profile of the relative vorticity over the Mediterranean region over a period of 5 years [26]. Bartzokas and Metaxas estimated the seasonal values of the geostrophic relative vorticity at four grid points in the Mediterranean by using pressure data for the period 1873–1988 [27]. Ruiz and Vargas studied the 500 hPa vorticity distribution over Argentina and its association with large-scale precipitation on a climatological basis [28]. Xoplaki et al. studied the wet season Mediterranean precipitation variability, and showed that since the mid-nineteenth century, precipitation steadily increased with a maximum in the 1960s and decreased since then [29]. There are a few climatological studies of vorticity in Iran. Golmohammadian and Pishvaie is one of the research projects concentrating on the relationship between vorticity and other synoptic indicators in Iran. This study used the model of area circulation to create monthly vorticity indicators in south of Iran for eight points on two surfaces of land and 500 hPa. The results showed that there is a trough in the East Mediterranean during all months of the year, and vorticity indicators with temperature are better than precipitation in analyzing the climatic responses to the selected station of Shiraz [30]. Alijani and Zahehi analyzed Azerbaijan precipitation to statistically and synoptically determine the types of air masses affecting this area. For this purpose, the daily precipitation data of the Tabriz station for the period of 1961–1995 and also pressure data at 12 am at ground level and 500 hPa were used. Consequently, 11 types of air masses in the precipitation of Azerbaijan were identified, with only 3 of them being high pressure [31]. In another study, Meshkati and Moradi examined the pressure trough of the Red Sea from the dynamic viewpoint, revealing that if the advection of relative positive vorticity takes place in the east of the Mediterranean or north of the Red Sea, the pressure trough of the Red Sea moves to the east of the

Mediterranean Sea and influences the west and northwest of Iran. On the other hand, if the advection of relative positive vorticity occurs in the northeast of the Red Sea, small low-pressure cells are separated from the trough of pressure on the Red Sea and move towards the northeast and affect the west, southwest, and south of Iran [32]. In contrast, Mofidi et al. investigating fall precipitation in the northern coast of Iran, showed that a high-pressure center on the west of the Caspian Sea and negative vorticity on the sea in lower levels of the atmosphere combined with strong currents and prevailing in the north-south direction are the main factors causing heavy and extreme fall precipitation in all the synoptic patterns of the Caspian [33].

The objective of this study is to investigate the vorticity over the prevalent winter precipitation in Iran, for a period of 53 years, along with its seasonal variations. This study, thus, seeks to understand from a climatological point of view the dynamic background of the troposphere over the regions that have an effect on the occurrence of prevalent winter precipitation in the study area. Furthermore, it is intended to gain a better insight into the dynamic mechanisms responsible for this kind of precipitation in Iran. Since prevalent and extreme precipitation is a dangerous phenomenon that will have environmental damages, especially in areas with small amounts of annual precipitation (e.g. Iran), it is critical to study the dynamic features that can help to better identify such precipitation. According to studies conducted by researchers inside and outside Iran, it is crucial to review the vorticity status of the atmosphere in prevalent winter precipitation in Iran. This can lead to an understanding of the relationship between atmospheric rotations and the surface environment of land in order to recognize different states of vorticity and their impact on convergence and divergence at different levels of the atmosphere, leading to the identification of prevalent precipitation in Iran. Therefore, in this study, we have tried to study the vorticity patterns leading to prevalent winter precipitation in Iran.

## 2. Materials and Methods

This study sought to examine the vorticity status of the atmosphere during prevalent winter precipitation in Iran. To this end, winter precipitation data of 483 stations were gathered from the Meteorological Organization of Iran (IRIMO). The spatial distribution of stations is shown in Figure 1. After sorting, a database with the size of  $7187 \times 4383$  was formed for a period of 53 years. Then, prevalent winter precipitation data were extracted from precipitation data with a minimum amount of a millimeter.

After the formation of database, three criteria were taken into account to determine the days with prevalent precipitation:

- (1) A minimum precipitation of one mm during the specific day
- (2) A precipitation lasting for at least two consecutive days
- (3) A precipitation covering at least 50% of the area (spatial continuity condition)

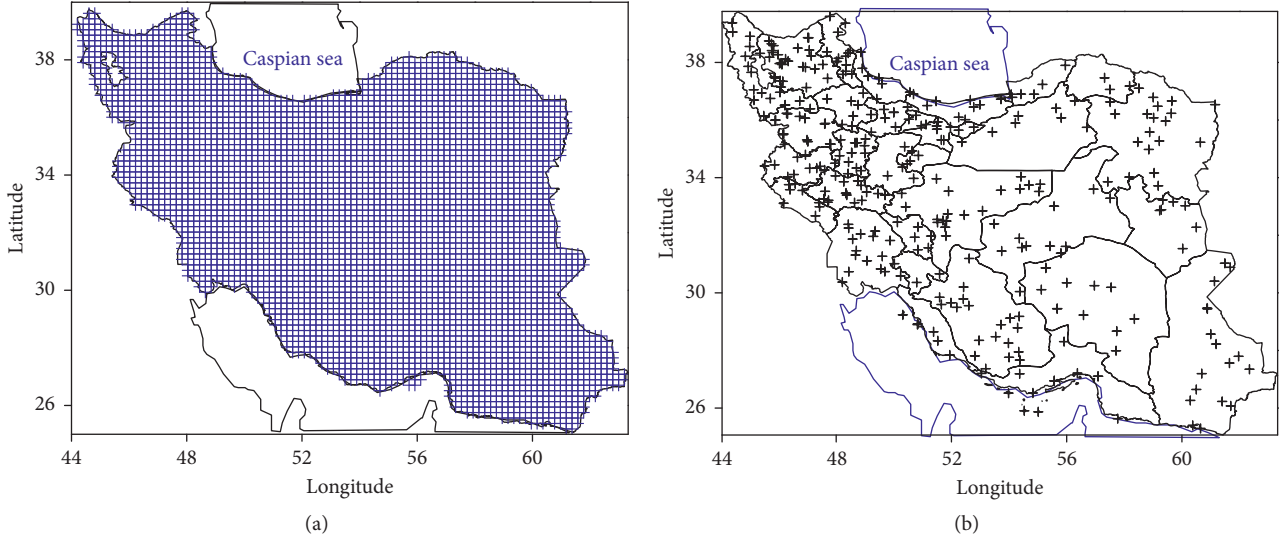


FIGURE 1: Regular grid of the precipitation database (a) and spatial distribution of studied stations (b).

By setting the conditions, just prevalent precipitation were selected for each of the cells studied and the relative concept of prevalent precipitation was observed for different regions of the country. The second criterion was having the precipitation for at least 2 consecutive days. Using this criterion, we were able to make a distinction between precipitation with a systematic (synoptic) origin and local precipitation that occurred due to convection or topography. After extracting the prevalent winter precipitation, pressure and U&V wind component data corresponding to the prevalent rainy days were extracted from NCEP/NCAR database with a spatial resolution of  $2.5 \times 2.5$  degree [34]. Finally, using the programming in GrADS software [35], vorticities of 1000, 850, 700, and 500 hPa for the days with prevalent precipitation were calculated

The vorticity is a vector quantity defined as the curl (cross-product) of the velocity vector. The relative vorticity is given as follows [36]:

$$\vec{U} = \nabla \times \vec{V} = \left( \frac{\partial w}{\partial y} - \frac{\partial v}{\partial z} \right) \hat{i} + \left( \frac{\partial u}{\partial z} - \frac{\partial w}{\partial x} \right) \hat{j} + \left( \frac{\partial v}{\partial x} - \frac{\partial u}{\partial y} \right) \hat{k}. \quad (1)$$

In Cartesian coordinates, a large fraction of the rotating fluid systems with which we are interested exhibit rotation in the horizontal plane (i.e., midlatitude cyclones, hurricanes, and tornadoes). Consequently, dynamic meteorology is most often, though not exclusively, interested in the vertical component of the relative vorticity. It is generally expressed as follows [36]:

$$\zeta = \hat{k} \cdot \vec{u} = \hat{k} \cdot \nabla * \vec{V} = \frac{\partial v}{\partial x} - \frac{\partial u}{\partial y}. \quad (2)$$

In the northern hemisphere, a positive vorticity indicates a cyclonic motion and a negative vorticity demonstrates an anticyclonic motion. Anticlockwise and clockwise movements are respectively called cyclonic and anticyclonic movement [32,37–40].

Subsequently, cluster analysis of 1000 hPa vorticity was used in order to identify vorticity patterns of prevalent winter precipitation in Iran. In the next step, the result of this cluster analysis was obtained with the aim of classifying the atmospheric vorticity data and detecting representative days. Cluster analysis is a method where the variables are classified based on the characteristics desired in certain groups. The aim of cluster analysis is to find out the real groups of people and reduce the volume of data. In other words, the aim is to identify a smaller number of groups so that similar data are grouped together in a way that within-group variation is minimized and between-group variation is maximized. In this method, data are grouped based on the distance or similarity between them. There are several ways to measure the distance between the data. One of the most popular methods is the Euclidean distance [7]. Lund correlation method was used in order to choose the representative days of groups derived from classifying data on atmospheric vorticity. Thus, a representative day of a particular group is the one with the highest similarity to the maximum number of days in the group. The correlation coefficient indicates the degree of similarity of patterns of two maps. But a certain correlation coefficient threshold must be determined. The correlation coefficient value in such cases typically varied between 0.5 and 0.7 [41]. In the current study, the cut-off point for identifying the representative days was a correlation coefficient of 0.5. Thus, the day with the highest number of correlation coefficient values greater than 0.5 with other days of the same group was regarded as the representative day.

### 3. Results and Discussion

Five patterns were identified as a result of the implementation of cluster analysis on 1000 hPa data with prevalent winter precipitation. The results are displayed in Figure 2 and Table 1.

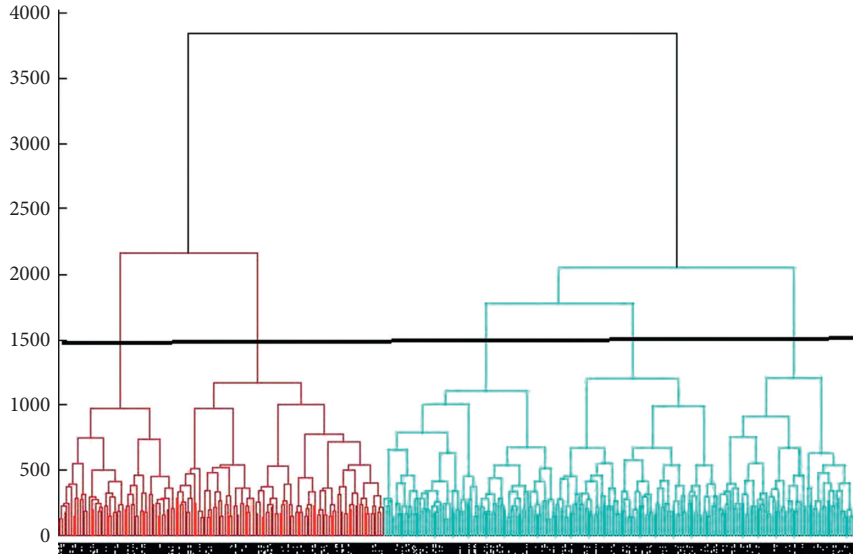


FIGURE 2: Dendrogram of cluster analysis on the Earth's surface pressure data.

TABLE 1: Some of the characteristics of identified patterns of prevalent winter precipitation in Iran.

1000 hPa vorticity patterns	Prevalence percentage	Overall precipitation	Frequency
Mediterranean low pressure-low-pressure dual-core Persian Gulf	50.132	3603	77
Iran closed low pressure-high pressure of east Europe	81.035	5824	73
Low pressure of Ural-high pressure of the Middle East	56.992	4096	60
European high pressure-low pressure of Saudi Arabia	58.314	4191	52
High-pressure belt of Siberia-low pressure of central Iran	55.322	3976	93

It is observed that the longest winter precipitation pattern in Iran (with a frequency of 93 days) occurred when the Siberian high-pressure belt-central Iran low pressure prevailed over Iran. On the other hand, the largest amount of overall precipitation in Iran happened when the low pressure of central Iran-high pressure of East Europe dominated the country (Table 1). However, at the time of the precipitation pattern of low pressure of the Mediterranean-low pressure of the Persian Gulf dual-core, the overall amount of precipitation reached 3603 mm.

In what follows, we provide a detailed description of the experimental results, present our interpretation, and draw a number of experimental conclusions.

**3.1. The First Pattern: Low Pressure of Persian Gulf Dual-Core-Low Pressure of East Mediterranean.** As illustrated in

Figure 3(a), the pressure and vorticity is 1000 hPa on Iran, and because of the exposure to dual-core low pressure in the Persian Gulf, the wind velocity is lower in the pole part; finally, in the eastern part of the low-pressure system, mass and density increase, and by increasing pressure, convergence will occur. While in its western part, due to the reduction of input mass from the north and increasing output mass from the southern part in the middle band, the mass and density are reduced and thus divergence will occur. However, the divergence of airflow in the low-pressure west of the Persian Gulf caused decreased airflow on the surface and vorticity advection of  $-2.5 \times 10^{-5}$  (m/s) on Iran's southern half. However, Lashkari showed that in a low-pressure flow, depending on the density of air and the input flow of air to its east, convergence occurs, and in its western part, divergence occurs due to the high speed of airflow [42–45]. Such a situation is clearly shown in Figure 3(a). On the other hand, the exposure of the west and northwest of the country to the East Mediterranean low pressure (wave front) caused a vertical rise and the convergence of airflow from a lower width at 1000 hPa (Figure 3(a)). So, the position of the low-pressure systems is critical because the systems usually have the strongest winds and the greatest waves [46]. With this interpretation, at the level of 850 hPa (Figure 3(b)) on Iran, positive vorticity advection of  $-2.5 \times 10^{-5}$  can be seen, which represents the planetary flows and vertical movements in the balance. As observed, vorticity minimum area on the north of the Black Sea can be detected coinciding with the full-height center of 1540 geopotential  $m$  that flows downward in a clockwise manner onto the northwest regions of the country.

Considering the amount of vorticity at 850 hPa, positive vorticity advection causes the flow of convergence on the lower level and intensification of flow of divergence in the upper level of the atmosphere [47]. On the other hand, at the levels of 700 and 500 hPa (Figures 3(c) and 3(d)), in accordance with the model 850 hPa, low-height center of 2960

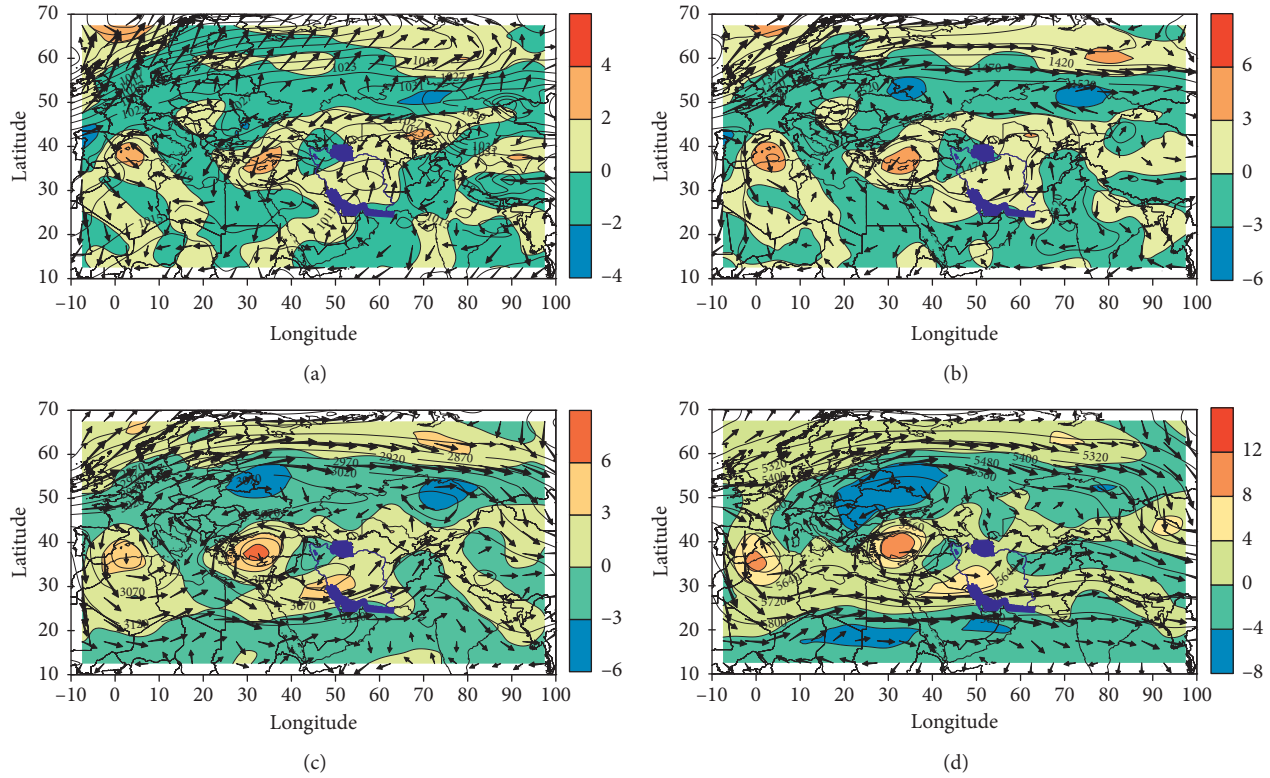


FIGURE 3: (a) 1000 hPa height (contours), vorticity ( $5 \times 10^{-5} s^{-1}$ ) (shaded), and wind flow (m/s) (vectors). (b) 850 hPa height, vorticity ( $5 \times 10^{-5} s^{-1}$ ), and wind flow (m/s). (c) 700 hPa height, vorticity ( $5 \times 10^{-5} s^{-1}$ ), and wind flow (m/s). (d) 500 hPa height, vorticity ( $5 \times 10^{-5} s^{-1}$ ), and wind flow (m/s).

geopotential meters is placed on the south of Turkey and East Mediterranean. The altitude trough is seen on the southwest and the Persian Gulf as positive vorticity advection on Iran causes a rise in the undercurrent convergence and vertical velocity of the air at the upper levels. At the 500 hPa level in Figure 3(d) on the southwest of the country, the altitude trough with positive vorticity advection of  $8 \times 10^{-5} s^{-1}$  shows convergence of rising flows of lower levels and upper level divergence. As a result of these conditions, the ground low pressure is constantly strengthened and deepened especially if it is accompanied with adequate moisture. After forming along the southwestern-northeast, the flows of the trough move to higher latitudes [48] and are converted to a dynamic mode and cause prevalent precipitation on Iran. In this pattern, the cyclone located on Iran is a dynamic system that synchronizes with the synoptic system of the middle levels of the atmosphere. This synoptic arrangement on Iran, with the supply of moisture from the Mediterranean and the Persian Gulf, has had a particular dynamic situation in the incidence of prevalent precipitation.

**3.2. The Second Pattern: Central Iran Closed Low Pressure-High Pressure of Europe.** In this model, according to Figure 4(a) on a map of 1000 hPa level, a low-pressure area with centrality of 1010 hPa and 1000 hPa as an inverse pressure trough is completely placed on the central plateau

of Iran. The stretch of the south flows towards the low-pressure north on Iran and causes the reduction of airflow and airflow divergence on Iran and negative vorticity advection of  $-3 \times 10^{-5} s^{-1}$ . On the other hand, on Central Europe, the high-pressure trough of 1022 hPa passes over the Black Sea and the Mediterranean and moves towards the lower latitudes in the central region of the Red Sea. This pressure arrangement is associated with the transmission of high-latitude cold and wet weather. In the upper level of 850 hPa (Figure 4(b)), we see low-height center of the Urals that is placed at a high level and west of the low-pressure center of land surface.

Moving up from the ground level, the low-height center of the upper level tends to move toward the northwest. In this level, convergence of degradation flows is observed behind the low-height trough where the negative vorticity advection of  $-3 \times 10^{-5} s^{-1}$  is placed to the north of the Red Sea and East Mediterranean. In contrast, the southern and eastern half of the country is placed on the elevation range of the trough and positive vorticity advection on the axis of the trough derived from the Urals low-height center on the west and southwest of  $3 \times 10^{-5} s^{-1}$ , causing the highest amount of convergence at 850 hPa. On the other hand, studying the maps of the higher levels of 700 and 500 hPa shows that, similar to 850 hPa of height, a trough with centrality of 2980 geopotential meter is placed on the border to the west of the country and the Persian Gulf (Figures 4(c) and 4(d)). Positive vorticity advection of  $5 \times 10^{-5} s^{-1}$  per second coincides

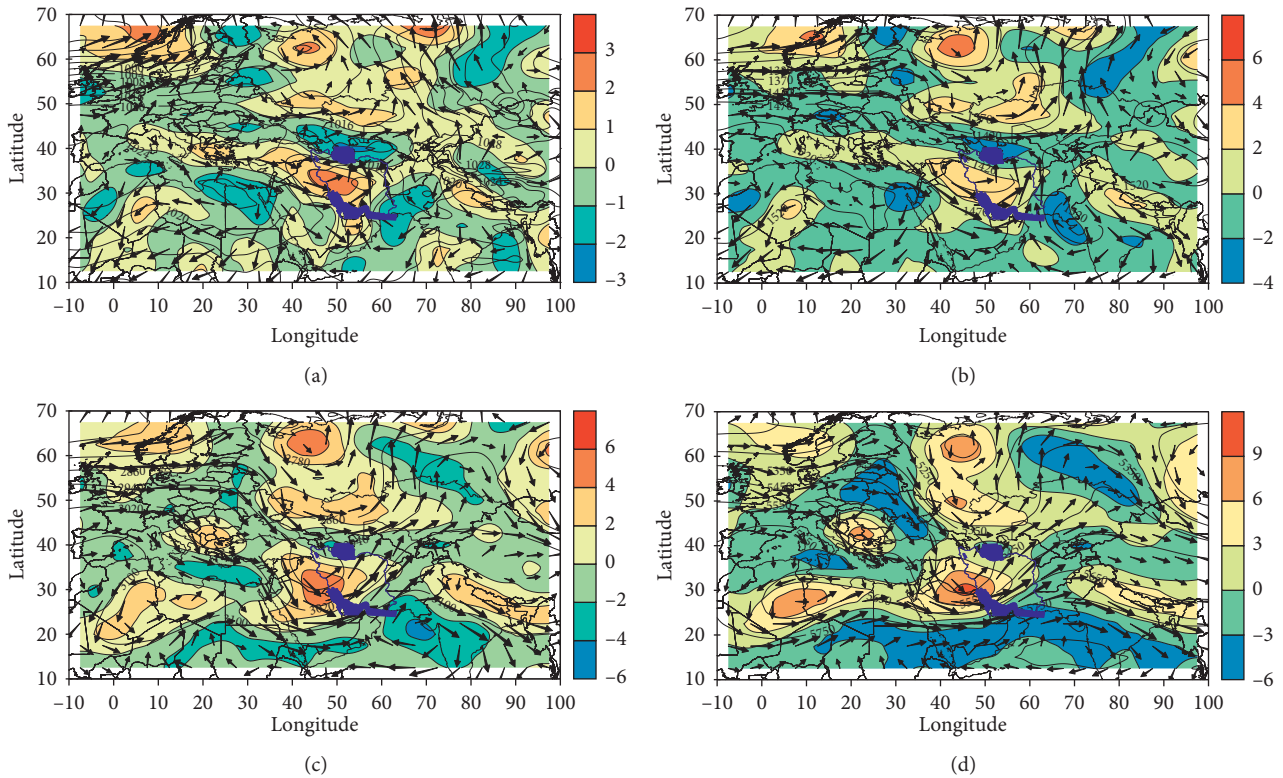


FIGURE 4: (a) 1000 hPa height (contours), vorticity ( $5 \times 10_{S^{-1}}^{-5}$ ) (shaded), and wind flow (m/s) (vectors). (b) 850 hPa height, vorticity ( $5 \times 10_{S^{-1}}^{-5}$ ), and wind flow (m/s). (c) 700 hPa height, vorticity ( $5 \times 10_{S^{-1}}^{-5}$ ), and wind flow (m/s). (d) 500 hPa height, vorticity ( $5 \times 10_{S^{-1}}^{-5}$ ), and wind flow (m/s).

with the axis of the trough. The convergence of subsurface flows and maximum upside cyclonic movements in 700 hPa all over of Iran were observed at 500 hPa level as its two lower levels. The axis of low height trough with centrality 5440 geopotential meter and positive vorticity advection with amount of  $7 \times 10_{S^{-1}}^{-5}$  coincide with the low height axis is placed on Iraq and Saudi Arabia. Convergence and descending of northern cold flows in the western slope are clearly observed. It is observed that, in the higher layers of the atmosphere, just above the surface low-pressure center on Iran, the weather is divergent and air climbing from the lower layer is extended and exits from the rising air. The low-height center of the levels of 850, 700, and 500 hPa are placed under the area of upper level divergence. As a result, the deep divergence in the upper layers caused the forced air vertically in lower layers. As a result, low-pressure system of ground is strengthened and positive vorticity advection and convergence of airflow occur in lower levels and continue up to 500 hPa in Iran in lower levels and continues up to 500 hPa on Iran. In this pattern, there was a short wave at the middle level, and positive vorticity at the lower level of the atmosphere. These dynamic systems have provided ascending conditions. Eventually, with the provision of moisture by the Oman Sea and the Persian Gulf, the dynamic system has caused prevalent precipitation in Iran.

**3.3. The Third Pattern: Low Pressure of the Urals-High Pressure of the Middle East.** According to Figure 5(a), at the 1000 hPa level, a very strong low-pressure center of 990 hPa with several closed curves is placed on the west of Russia widely. Two pressure tongues are derived from it; one is with pressure of 1010 hPa in a southwesterly direction drawn through the Black Sea to the Mediterranean. The other tongue is in the southeast, crossing the Caspian to central areas of Iran (1014 hPa). This situation has led to taking sufficient moisture by passing through the Caspian Sea and transferring it to the central regions of Iran. As a result of such action, widespread precipitation has occurred especially in areas to the southeast of the country. In addition, on the northeast of Africa, Egypt, Syria, Iraq, and Saudi Arabia, a wide area of relatively high pressure of 1022 hPa is observed that in accordance with the low-pressure tongue of the Urals causes positive vorticity advection of  $2 \times 10_{S^{-1}}^{-5}$  on the west and northwest of Iran.

At the level of 850 hPa in Figure 5(b), which matches the pressure pattern of 1000 hPa, the Ural low-pressure center is placed on west of Russia with centrality of 1200 geopotential meter. An elevation trough is observed in East Europe and the Mediterranean and on Iran passing from the Caspian Sea to the Persian Gulf. The cold weather of Scandinavia and

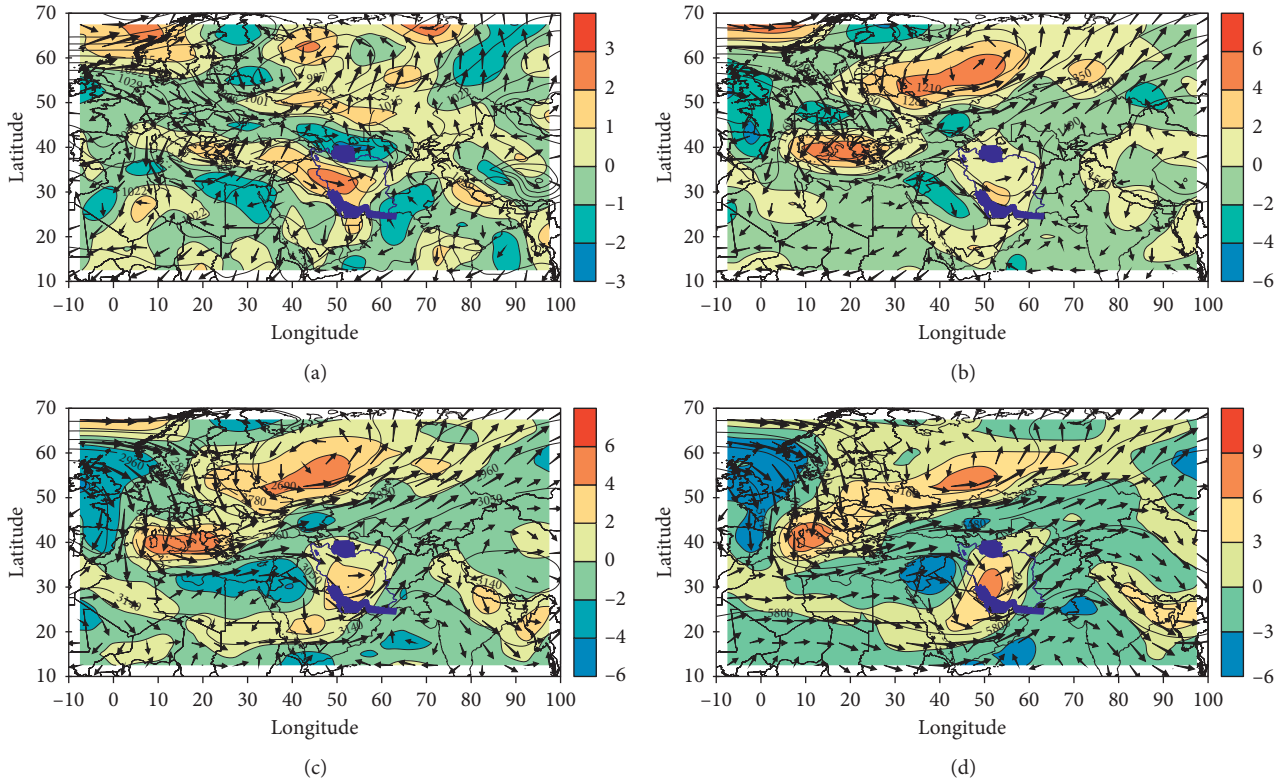


FIGURE 5: (a) 1000 hPa height (contours), vorticity ( $5 \times 10_{S-1}^{-5}$ ) (shaded), and wind flow (m/s) (vectors). (b) 850 hPa height, vorticity ( $5 \times 10_{S-1}^{-5}$ ), and wind flow (m/s). (c) 700 hPa height (hPa), vorticity ( $5 \times 10_{S-1}^{-5}$ ), and wind flow (m/s). (d) 500 hPa height, vorticity ( $5 \times 10_{S-1}^{-5}$ ), and wind flow (m/s).

Siberia transfers to lower latitudes by the low height centrality and its convergence with wet flows of Mediterranean and the Black Sea from the trough of the Mediterranean and its transfer to Iran by a relatively deep trough, based on the center of the country. In its movement from stack to the trough, the air has downward movement and with convergence, so the trough is the center of positive vorticity advection with amount of  $2 \times 10_{S-1}^{-5}$  and the maximum of convergence located on the trough axis [5, 47]. At the levels of 700 and 500 hPa, Figures 5(c) and 5(d), an elevation model of 850 hPa can also be clearly observed. Negative vorticity advection of  $-4.5 \times 10_{S-1}^{-5}$  is placed on East Mediterranean and the east of Iraq and Jordan. It causes reduction and air convergence at the trough axis and rising flows in front of the trough at this level. On the other hand, vorticity advection at the 700 hPa level of  $3 \times 10_{S-1}^{-5}$  on the trough axis is centered on Iran and its eastern slope of elevation. Convergence of cyclonic flows and rising air masses in these areas, especially the eastern half of the country, can be observed. As it can be observed, on the upper level (i.e., 500 hPa), the trough axis based on Iran is drawn with slight change to the below layers on the southwest areas of the Persian Gulf and lower latitudes to Saudi Arabia. The deepening trough above leads to durable stability and convergence of the flows related to Mediterranean, northern parts of the Red Sea, the Persian Gulf, and the Sea of Oman. As in front of the trough (its east range), positive vorticity advection of  $6 \times 10_{S-1}^{-5}$  leads to the severe divergence of

uppermost level, convergence of undercurrent, and thus, the formation of heavy precipitation, especially on the eastern half and south of the country. In fact, the areas are placed in front of the warm front. This convergence in the upper layers leads to the accumulation of air, which is dropped over the high-pressure of its bottom surface. The weather descended is replaced by diverged air at ground level, and even if the thickness of the layer of convergence at higher levels on the thickness of the low-level divergence is more, or in other words, the trough level is closer to the Earth's surface, the high pressure of Middle East is amplified. As a result, this pressure arrangement at different atmospheric levels strengthens the pressure trough on Iran and expands the front part of trough and maximum wind vorticity at the levels of 850, 700, and 500 hPa, and the upper-level divergence on the eastern half of Iran and required dynamic conditions for prevalent precipitation on Iran. In this pattern, a relatively deep trough in the middle level of the atmosphere has been formed on Iran. The establishment of the above situation created and strengthened the Ural low pressure and the high pressure of the east and west of Iran and subsequently made the northern-southern flows intense at the surface and the lower levels of the atmosphere. Therefore, the above two systems flew the cold and moist air from the Caspian Sea, Black Sea, and Mediterranean Sea to Iran. When this cold air crosses the warmer seas, it causes prevalent precipitation in Iran.

*3.4. The Fourth Pattern: Low-Pressure of Saudi Arabia and High-Pressure Europe.* According to Figure 6(a), at the level of 1000 hPa, a very broad area of high pressure 1030 hPa can be seen on Europe from parts of Scandinavia to the Mediterranean in the south and the east of the borders of Russia. The high-pressure tongue enters the country from the northwest and the Caspian Sea. The establishment of this high-pressure center dramatically increases the circulation in the lower levels of the atmosphere over the entire Caspian Sea region. As it moves into northern parts of the Caspian Sea, the cyclonic circulation increases, and the maximum negative vorticity is observed at the northern end of the Caspian Sea. On the other hand, a broad low-pressure center of 1010 hPa is entirely placed on Saudi Arabia, Iraq, and the Persian Gulf. The high pressure of Europe has created a strong gradient on the Black Sea, Turkey, Iraq, and especially the northern half of the country, and positive vorticity advection of  $2.5 \times 10_{S-1}^{-5}$  winds on the country's northwest. The pressure arrangement leads to warm air advection of lower latitudes in the northern half of the country and diffusion of very cold weather in northern Europe to the region. At the 850 hPa level in Figure 6(b), the high height center of 1580 geopotential meters is located perfectly on Europe and its tongue of 1520 geopotential meters on the northern strip. On the other hand, low height center with the amount of 1400 geopotential meters is placed on the north of Kazakhstan with its troughs from the northeast influencing the borders of the country. This height situation led to a convergence of very cold flows of northern Europe and Siberia and its precipitation on the northern regions of the country. On the other hand, the very strong height trough with several contours at 1440 geopotential meters is placed on Iraq and Saudi Arabia. The situation follows the advection of warm and moist currents from the Mediterranean and the Red seas to the Persian Gulf on Iran. Hence, that vorticity advection in the eastern tongue of a low height of  $3 \times 10_{S-1}^{-5}$  corresponding to intense flows of north leads to increase of mass and density and increasing convergence pressure in the level above the country.

At the 850 hPa level, the high height of 1580 geopotential meters (Figure 6(b)) is entirely located on Europe, and a tongue of it drawn on the northern strip of Iran (1520 geopotential meters). The deployment of this high pressure leads to a widespread and continuous north-northeast flow in the lower levels on the northern half of Iran. On the other hand, a low-height center of 1,400 geopotential meters is located in northern Kazakhstan, with its tongue infiltrating from the northeast of the borders of Iran. This height features led to the convergence of the very cold currents of northern Europe and Siberia and its downfall over the northern regions of Iran. Besides, a very strong trough is located in Iraq and Saudi Arabia and this situation has led to the convergence of hot and humid currents from the Mediterranean Sea, Red Sea, and Persian Gulf on Iran ( $3 \times 10_{S-1}^{-5}$ ). In these conditions, the vorticity convergence of the eastern tongue of low height has been adapted to the northward currents on Iran. As

a result, all of these situations lead to increase in mass and density of airflow on the country, which has resulted in an increase in pressure and convergence at the 850 hPa level.

At the 700 hPa level in Figure 6(c), the height arrangement of the lower level is affected by the south elevation trough, whose center of 3000 geopotential meters is placed on southern Turkey, Iraq, Syria, and East Mediterranean. Transfer of moisture from the Mediterranean Sea, the Red Sea, and the Persian Gulf, especially positive vorticity advection of  $2.5 \times 10_{S-1}^{-5}$ , can be observed on the eastern slopes of the trough. At the 500 hPa level in Figure 6(d), the lower level of the axis of the southern trough, perfectly on the Red Sea and the middle of it, is drawn. The positive vorticity advection area corresponding to the trough with amount of  $7 \times 10_{S-1}^{-5}$  intensifies the divergence in upper levels and convergence in the lower levels. Saudi Arabia has low-pressure condition, and there are enhanced uplink moves in Iran and the Middle East by intensity of divergence in higher levels. Due to the establishment of a relatively deep trough at the midlevels between the Caspian Sea and the Aral Lake, the vorticity on the northern regions, especially the eastern parts of the Caspian Sea, are mostly positive, and in the surface map, a low pressure or cyclonic circulation dominated on the Aral Lake. In contrast, at the surface, a dynamic high pressure has been established on the whole region of the southern part of the Caspian Sea and the regions between the Caspian Sea and the Black Sea [49]. These conditions and the location of the low pressure of Saudi Arabia on the southern half of Iran have led to a fairly severe vorticity convergence at the lower and middle levels of the Iran's atmosphere. These features provided the climbing conditions, especially in the northern half of the country, and have caused the widespread precipitation in Iran.

In the precipitation pattern, with the outbreak of widespread precipitation on Iran leading to the release of latent heat of vaporization of rain, it added to the intensity of flotation and uplink movements. By intensifying uplink movements and expansion of air, the vorticity of the system is further increased, and by intensifying the vorticity of low height centers on the Middle East, it added to the severity of divergence in the upper levels of the atmosphere. In this pattern, at the middle level of the atmosphere, the front part of the trough with direction of northeast-southwest is located on Iran. The southward expansion of this trough has strengthened the surface low pressure. Therefore, with the availability of ascending conditions and with the humidity advection from the Mediterranean Sea and the Persian Gulf water resources caused the prevalent precipitation of Iran.

*3.5. The Fifth Pattern: High Pressure Belt of Siberia-Central Iran Low Pressure.* According to Figure 7(a), the low pressure of central Iran with pressure of the central core of 1010 hPa is placed in Iran in the northeast direction, whose south tongue with north side caused the rising of wet flows from the Sea of Oman and the Persian Gulf on Iran. Negative vorticity advection on Iran of  $-1.5 \times 10_{S-1}^{-5}$  can be seen due to the placement of the western part of low pressure on the country and reducing input airflow from north and

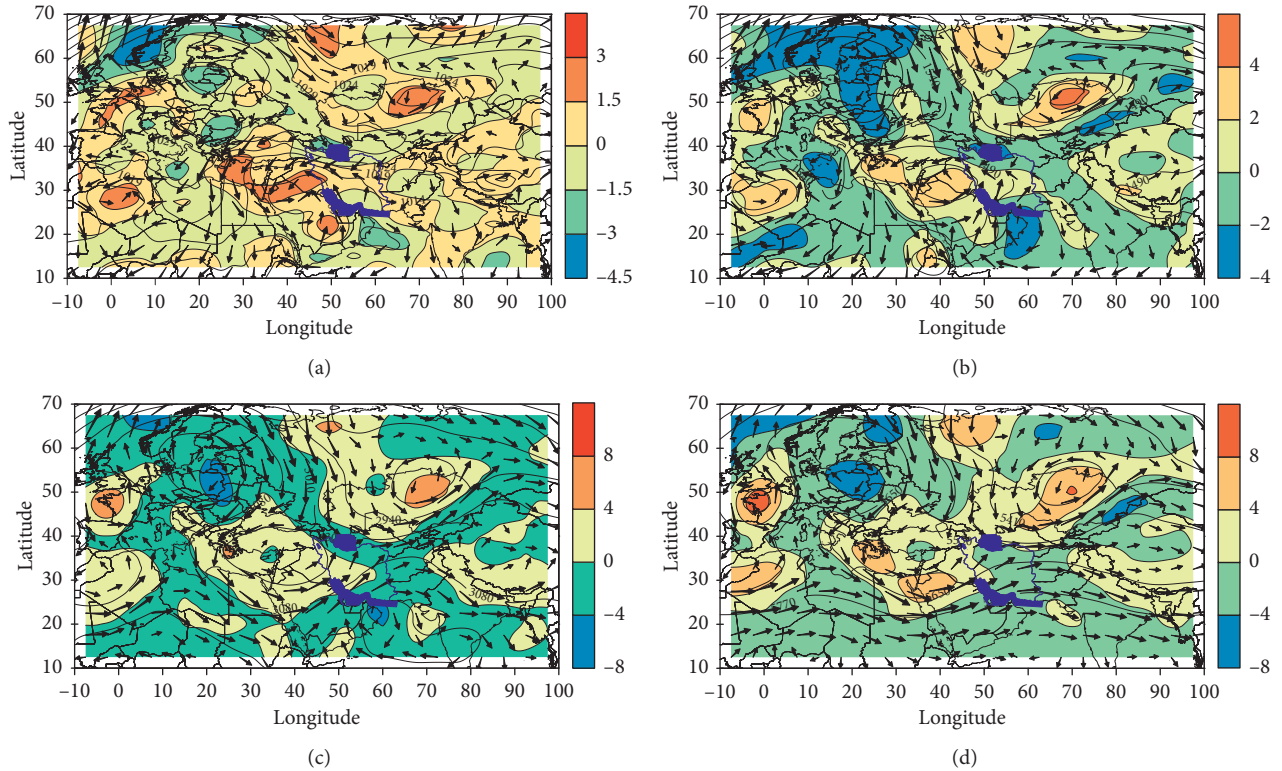


FIGURE 6: (a) 1000 hPa height (contours), vorticity ( $5 \times 10_{S^{-1}}^{-5}$ ) (shaded), and wind flow (m/s) (vectors). (b) 850 hPa height, vorticity ( $5 \times 10_{S^{-1}}^{-5}$ ), and wind flow (m/s). (c) 700 hPa height, vorticity ( $5 \times 10_{S^{-1}}^{-5}$ ), and wind flow (m/s). (d) 500 hPa height, vorticity ( $5 \times 10_{S^{-1}}^{-5}$ ), and wind flow (m/s).

increasing output mass in the south part of low pressure, reducing mass and the density of pressure, leading to divergence. On the other hand, the Siberian high pressure is reinforced and its range expanded to the northern half of the country causing the loss of cold air, decreasing airflow into the country, and exacerbating the divergence on the surface of the ground. Pressure arrangement of two low-pressure centers in the Persian Gulf and Siberian high pressure caused a sharp pressure and exacerbating instability on the northeastern areas of the country. At 850 hPa in Figure 7(b) as well as sea level, the low-height belt of central Iran with a central height of 1360 and 1400 geopotential meters is placed on Iran and the northeast. Positive vorticity advection on Iran of  $3 \times 10_{S^{-1}}^{-5}$ , matching the central core of low height, can be seen on Iran. However, this value in northwest reaches  $2 \times 10_{S^{-1}}^{-5}$ . On the map, at the pressure of 700 and 500 hPa in Figures 7(c) and 7(d), the axis of the trough is placed in the East and Southeast of Iran, and vorticity advection with the amount of  $5 \times 10_{S^{-1}}^{-5}$  can be seen in this area. Considering that the placing of low pressure of central Iran in below levels caused the rise and convergence at lower levels of the atmosphere on the eastern and southeastern part and on the northwest of Iran at 700 hPa level, a low height center with center based at 2960 geopotential meters causes rising and convergence in the lower layers of the atmosphere. Positive vorticity advection resonance indicates rising and positive convergence at the levels of 700 and 500 hPa. In this pattern, in the higher layers, air density is

reduced, and reducing density increases vertical airflow in the lower layers of the atmosphere. In such a case, the flow of cold weather cools down due to adiabatic flow and causes the column of airflow on low pressure of central Iran to be colder than the surrounding environment, and the thickness of the column of airflow is reduced. Therefore, due to the decrease in the density of the air column at the levels of 850 and 700 hPa, curves at lower altitude are placed at surrounding area and can be seen on maps of 850, 700, and 500 hPa as low height cores (Figures 7(b)–7(d)). According to the process of turning at low pressure on the surface of the Earth (counterclockwise rotation), the flow of cold air is placed behind the low pressure [48, 50]. In other words, the western half of the low pressure of central Iran is colder than the eastern half, so the low-pressure of central Iran is stronger and axis of low pressure with increasing height at the levels of 850, 700, and 500 hPa inclined to the colder weather in the west, and the low-pressure system on Iran extended to southeast-northwest. This pressure arrangement at different atmospheric levels and placement of trough axis on Iran causes the intensity of vorticity advection and vertical rising of air at levels of 1000, 850, 700, and 500 hPa and divergence of air in the upper levels of the atmosphere. In this pattern, the trough axis positioning on the southern half of the country and low pressure on the surface has strengthened the upstream flow and exacerbated the instability in the region. These dynamic conditions have resulted in humidity advection from the Persian Gulf and

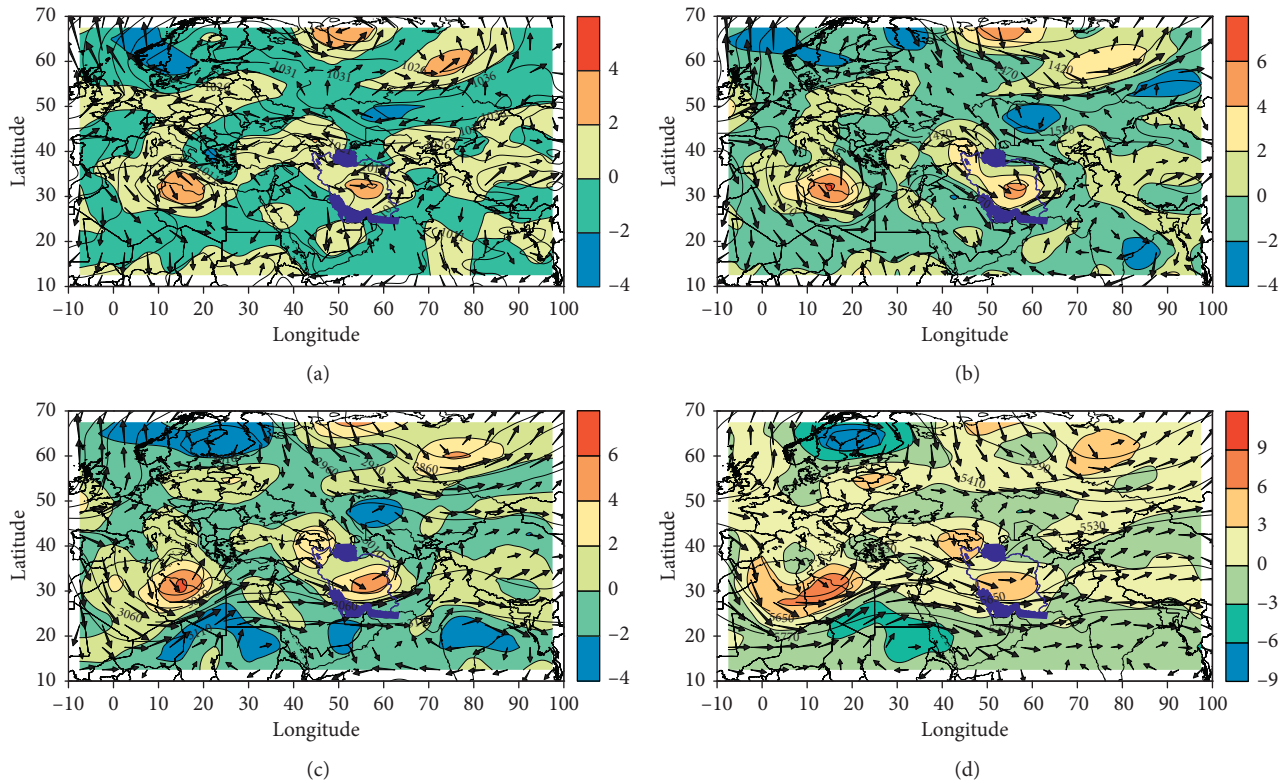


FIGURE 7: (a) 1000 hPa height (contours), vorticity ( $5 \times 10^{-5} s^{-1}$ ) (shaded), and wind flow (m/s) (vectors). (b) 850 hPa height, vorticity ( $5 \times 10^{-5} s^{-1}$ ), and wind flow (m/s). (c) 700 hPa height, vorticity ( $5 \times 10^{-5} s^{-1}$ ), and wind flow (m/s). (d) 500 hPa height, vorticity ( $5 \times 10^{-5} s^{-1}$ ), and wind flow (m/s).

the Oman Sea to Iran and the formation of prevalent precipitation.

Low-pressure systems have played a major role in the occurrence of winter-prevalent precipitation in Iran in all patterns. By creating instability in the atmosphere, these systems have led to the formation of baroclinic states, especially in the lower level of atmosphere. In the common mechanism of the occurrence of prevalent precipitation in all patterns was the role of midlatitude's trough (such as the Mediterranean trough) in strengthening low-pressure systems of lower levels of atmosphere, as well as the water resources such as the Persian Gulf, the Oman Sea, the Mediterranean Sea, the Caspian Sea, and the Black Sea in the provision of required humidity for that dynamic systems.

#### 4. Conclusion

In this study, the status of vorticity of the atmosphere of pressure centers on Iran and the mechanisms of climate changes on widespread winter precipitation in Iran were investigated. For this purpose, the data of prevalent winter precipitation in Iran were identified on the basis of a millimeter precipitation threshold. After extracting prevalent winter precipitation in Iran, the U&V wind component and pressure data corresponding to the widespread rainy days were extracted from the databases of NCEP/NCAR and vorticities of these days were calculated. Then, by the implementation of cluster analysis, representative days for

each group were specified. The results of this study showed that the atmospheric vorticity status during prevalent winter precipitation in Iran is influenced by the interaction of low-pressure patterns of the Persian Gulf double core-low pressure of the East Mediterranean, central Iran closed low pressure-high pressure of Europe, low pressure of the Urals-high-pressure of the Middle East, low pressure of the Urals-high-pressure of Europe, and the high-pressure belt of Siberia-low pressure of central Iran.

In addition, the placement of the low pressure of dual-core of the Persian Gulf-East Mediterranean low pressure on Iran at levels of 850, 700, and 500 hPa of maximum positive vorticity caused rising and convergence of airflow at higher levels and the bottom surfaces. As a result of such conditions, the low pressure of land surface with moisture injected from the Persian Gulf and the Oman Sea and trough on Iran in high levels have strengthened its atmosphere. Positive vorticity advection on Iran is continued up to 500 hPa. In this regard, Alijani et al. investigated Iran's low-pressure role in the intensification of positive vorticity. The results of this study showed that this low pressure was the main cause of moisture transmission and the occurrence of precipitation in the first decade of July 1994 in the southeast of Iran [51]. The formation of this low pressure on the northern side of the Persian Gulf, while increasing the cyclonic motion in the southern part of the country, by creating suitable southern streams in the southeast of Iran and transferring the moisture content of the Oman Sea in a thin layer to the

studied area caused the extreme precipitation in south-eastern Iran.

However, at the time of central Iran closed low pressure-high pressure of Europe, the center of low pressure on Iran caused convergence and rising airflow to higher latitudes. The placement of trough axis at levels of 850, 700, and 500 hPa caused increased positive vorticity advection on Iran and rising air in the lower atmosphere layers and divergence in the upper levels of the atmosphere. Therefore, the positive vorticity maximum is continued up to 500 hPa. In fact, the high pressure on the Middle East and the influence of the low-pressure tongue of the Urals on Iran and closing of the surface of trough to the Earth's surface caused the high pressure of Middle East to strengthen.

As a result of this pressure arrangement at different levels of the atmosphere, the pressure trough on Iran is strengthened. These conditions exacerbated dynamic conditions for the occurrence of widespread precipitation on Iran. On the other hand, the influence of the low-pressure tongue in Saudi Arabia on Iran at the ground level caused positive vorticity advection and influenced north flowing towards Iran. The low pressure of Saudi on Earth strengthened itself by the exposure to the wave of west wind at higher levels and exacerbated the divergence, leading to strengthened rising movements on Iran. Latent heat of vaporization of precipitation led to strengthening the uplink flow on Iran with these conditions increasing by strengthening the uplink flows and expansion and vorticity of the system, causing divergence in the upper levels of atmosphere. Vorticity state of the atmosphere during the formation of the central Iran low pressure made the flow of cold weather in the western half of low pressure placed on Iran colder than its eastern half. This strengthens the central Iran low pressure and causes the inclination of the low-pressure axis at levels of 850, 700, and 500 hPa in the western and northwestern areas in Iran. Pressure arrangement in different atmospheric levels and placing trough axis on Iran led to intensifying the positive vorticity advection on Iran. In the studies of Golmohammadian and Pishvaei about the production of daily rotation index and its effect on the temperature and precipitation of the northeastern part of Iran, it has been concluded that during the warm seasons, a ridge pattern has an absolute sovereignty in this region, which represents the emergence of a tropical belt on the area. As a result, Mashhad has a warm and dry climate in the warm seasons, while this cannot be seen in the cold seasons [52]. The average monthly vorticity indicator in the coldest half of the year has the highest value, indicating the frequency of cyclonic systems. In most cases, increasing the vorticity rate in one region leads to a decrease in temperature and an increase in precipitation. The major difference between the third and fourth patterns with other patterns is that the low-pressure systems of these patterns have an origin from the outside of the Iran. But in the first, second, and fifth patterns, the core of the low-pressure systems has been formed inside Iran.

### Conflicts of Interest

The authors declare that they have no conflicts of interest.

### Acknowledgments

This work was supported by Vedurfelagid, Rannis, and Rannsóknastofa I Vedurfrædi. Iman Rousta is deeply grateful to his supervisor (Haraldur Olafsson, Professor of Atmospheric Sciences, Department of Physics, University of Iceland, Institute for Atmospheric Sciences and Icelandic Meteorological Office), for his great support, kind guidance, and encouragement.

### References

- [1] I. Rousta, M. Nasserzadeh, M. Jalali et al., "Decadal spatial-temporal variations in the spatial pattern of anomalies of extreme precipitation thresholds (case study: northwest Iran)," *Atmosphere*, vol. 8, no. 12, p. 135, 2017.
- [2] C. Data, *Guidelines on Analysis of Extremes in a Changing Climate in Support of Informed Decisions for Adaptation*, World Meteorological Organization, Geneva, Switzerland, 2009.
- [3] A. Taimor, A. Qhasem, and I. Rousta, "Analyzing of 500 hpa atmospheric patterns in the incidence of pervasive and sectional rainfall in Iran," *Planning and arrangement of space*, vol. 16, no. 4, pp. 1–24, 2012.
- [4] M. Soltani, I. Rousta, and S. S. M. Taheri, "Using Mann-Kendall and time series techniques for statistical analysis of long-term precipitation in gorgan weather station," *World Applied Sciences Journal*, vol. 28, no. 7, pp. 902–908, 2013.
- [5] I. Rousta, M. Doostkamian, E. Haghighi, H. R. G. Malamiri, and P. Yarahmadi, "Analysis of spatial autocorrelation patterns of heavy and super-heavy rainfall in Iran," *Advances in Atmospheric Sciences*, vol. 34, no. 9, pp. 1069–1081, 2017.
- [6] I. Rousta, M. Soltani, W. Zhou, and H. H. N. Cheung, "Analysis of extreme precipitation events over central plateau of Iran," *American Journal of Climate Change*, vol. 5, no. 3, p. 297, 2016.
- [7] M. Soltani, P. Laux, H. Kunstmann et al., "Assessment of climate variations in temperature and precipitation extreme events over Iran," *Theoretical and Applied Climatology*, vol. 126, no. 3, pp. 775–795, 2016.
- [8] I. Rousta, M. Doostkamian, A. Taherian, E. Haghighi, H. G. Malamiri, and H. Ólafsson, "Investigation of the spatio-temporal variations in atmosphere thickness pattern of Iran and the middle east with special focus on precipitation in Iran," *Climate*, vol. 5, no. 4, p. 82, 2017.
- [9] I. Rousta, M. Doostkamian, E. Haghighi, and B. Mirzakhani, "Statistical-synoptic analysis of the atmosphere thickness pattern of Iran's pervasive frosts," *Climate*, vol. 4, no. 3, p. 41, 2016.
- [10] J. R. Harman, *Synoptic Climatology of the Westerlies: Process and Patterns*, Association of American Geographers, Washington, DC, USA, 1991.
- [11] L. A. Mofor and C. Lu, "Generalized moist potential vorticity and its application in the analysis of atmospheric flows," *Progress in Natural Science*, vol. 19, no. 3, pp. 285–289, 2009.
- [12] N. R. Council, *The Atmospheric Sciences: Entering the Twenty-First Century*, The National Academies Press, Washington, DC, USA, 1998.
- [13] M. Soltani, P. Zavar-Reza, F. Khoshakhlagh, and I. Rousta, "Mid-latitude cyclones climatology over Caspian Sea Southern Coasts–North of Iran," in *Proceedings of 21st Conference on Applied Climatology*, pp. 1–7, American Meteorological Society (AMS), London, UK, 2014, <https://ams>.

- confex.com/ams/21Applied17SMOI/webprogram/Paper246601.html.
- [14] T. Dessouky and A. Jenkinson, "An objective daily catalogue of surface pressure, flow, and vorticity indices for Egypt and its use in monthly rainfall forecasting," *Meteorological Research Bulletin, Egypt*, vol. 11, pp. 1–25, 1975.
- [15] A. Jenkinson and F. Collison, "An initial climatology of gales over the North Sea," *Synoptic Climatology Branch Memorandum*, vol. 62, p. 18, 1977.
- [16] D. Conway and P. Jones, "The use of weather types and air flow indices for GCM downscaling," *Journal of Hydrology*, vol. 212, pp. 348–361, 1998.
- [17] P. Jones, M. Hulme, and K. Briffa, "A comparison of Lamb circulation types with an objective classification scheme," *International Journal of Climatology*, vol. 13, no. 6, pp. 655–663, 1993.
- [18] R. M. Trigo and C. C. DaCAMARA, "Circulation weather types and their influence on the precipitation regime in Portugal," *International Journal of Climatology*, vol. 20, no. 13, pp. 1559–1581, 2000.
- [19] I. Phillips and G. McGregor, "The relationship between synoptic scale airflow direction and daily rainfall: a methodology applied to Devon and Cornwall, South West England," *Theoretical and Applied Climatology*, vol. 69, no. 3, pp. 179–198, 2001.
- [20] H. Nakamura, "Horizontal divergence associated with zonally isolated jet streams," *Journal of the atmospheric sciences*, vol. 50, no. 14, pp. 2310–2313, 1993.
- [21] M. R. Sinclair, "A diagnostic study of the extratropical precipitation resulting from Tropical Cyclone Bola," *Monthly Weather Review*, vol. 121, no. 10, pp. 2690–2707, 1993.
- [22] C. Mattocks and R. Bleck, "Jet streak dynamics and geostrophic adjustment processes during the initial stages of lee cyclogenesis," *Monthly Weather Review*, vol. 114, no. 11, pp. 2033–2056, 1986.
- [23] R. A. Maddox and C. A. Doswell, "An examination of jet stream configurations, 500 mb vorticity advection and low-level thermal advection patterns during extended periods of intense convection," *Monthly Weather Review*, vol. 110, no. 3, pp. 184–197, 1982.
- [24] D. G. Vincent, "Cyclone development in the south pacific convergence zone during fgge, 10-17 January 1979," *Quarterly Journal of the Royal Meteorological Society*, vol. 111, no. 467, pp. 155–172, 1985.
- [25] G. Wang, J. Su, Y. Ding, and D. Chen, "Tropical cyclone genesis over the South China Sea," *Journal of Marine Systems*, vol. 68, no. 3, pp. 318–326, 2007.
- [26] P. Alpert, B. Neeman, and Y. Shay-El, "Climatological analysis of Mediterranean cyclones using ECMWF data," *Tellus A: Dynamic Meteorology and Oceanography*, vol. 42, no. 1, pp. 65–77, 1990.
- [27] A. Bartzokas and D. Metaxas, *Climatic Fluctuation of Temperature and Air Circulation in the Mediterranean*, Commission of the European Communities (CEC), Europe, 1991.
- [28] N. Ruiz and W. Vargas, "500 hPa vorticity analyses over Argentina: their climatology and capacity to distinguish synoptic-scale precipitation," *Theoretical and Applied Climatology*, vol. 60, no. 1–4, pp. 77–92, 1998.
- [29] E. Xoplaki, J. F. González-Rouco, J. Luterbacher, and H. Wanner, "Wet season Mediterranean precipitation variability: influence of large-scale dynamics and trends," *Climate dynamics*, vol. 23, no. 1, pp. 63–78, 2004.
- [30] G. Hadis and P. Mohammad Reza, "Daily vorticity index and its impacts on precipitation and temperature in Khorassan region in 1948-2010," *Journal of Applied Researches in Geographical Sciences*, vol. 13, no. 29, pp. 217–236, 2013.
- [31] B. Alijani and M. Zahehi, "Statistical and synoptic analysis of Azerbaijan area rainfall," *Iranian Journal of Research in Geography*, pp. 65–66, 2002.
- [32] M. Mohammad Hossain and M. Mohammad, "investigating pressure trough of Red Sea from the perspective of the dynamic," *Nivar*, vol. 52, pp. 67–74, 2004.
- [33] A. Mofidi, A. Zarrin, and G. R. J. Ghobadi, "Determining the synoptic patterns of autumn-time extreme and severe precipitation over the southern coasts of Caspian Sea," *Journal of the Earth and Space Physics*, vol. 33, no. 3, p. 30, 2008.
- [34] E. Kalnay, M. Kanamitsu, R. Kistler et al., "The NCEP/NCAR 40-year reanalysis project," *Bulletin of the American Meteorological Society*, vol. 77, no. 3, pp. 437–471, 1996.
- [35] B. E. Doty and J. L. I. Kinter, *Geophysical Data Analysis and Visualization Using the Grid Analysis and Display System*, National Aeronautics and Space Administration, Washington, DC, USA, 1995.
- [36] J. E. Martin, *Mid-Latitude Atmospheric Dynamics: a First Course*, John Wiley & Sons, Hoboken, NJ, USA, 2013.
- [37] M. R. Kaviani and B. Alijani, *Principles of Climatology*, SAMT Press, Tehran, Iran, 1st edition, 2001.
- [38] K. E. Trenberth, "Recent observed interdecadal climate changes in the Northern Hemisphere," *Bulletin of the American Meteorological Society*, vol. 71, no. 7, pp. 988–993, 1990.
- [39] B. J. Hoskins and K. I. Hodges, "New perspectives on the Northern Hemisphere winter storm tracks," *Journal of the Atmospheric Sciences*, vol. 59, no. 6, pp. 1041–1061, 2002.
- [40] E. K. Chang and D. B. Yu, "Characteristics of wave packets in the upper troposphere. Part I: Northern Hemisphere winter," *Journal of the Atmospheric Sciences*, vol. 56, no. 11, pp. 1708–1728, 1999.
- [41] B. Alijani, J. O'Brien, and B. Yarnal, "Spatial analysis of precipitation intensity and concentration in Iran," *Theoretical and Applied Climatology*, vol. 94, no. 1, pp. 107–124, 2008.
- [42] H. Lashkari, Z. Mohammadi, and G. Keikhosravi, "Annual fluctuations and displacements of inter tropical convergence zone (ITCZ) within the range of Atlantic Ocean-India," *Open Journal of Ecology*, vol. 7, no. 1, p. 12, 2017.
- [43] E. Haghghi, S. Jahanbakhsh, M. R. Banafshe, and I. Rousta, "The study relationship between large-scale circulation patterns of sea level and snow phenomenon in the North West of Iran," *Territory*, vol. 12, no. 48, pp. 19–35, 2016, in Persian.
- [44] G. Azizi, H. Mohammadi, M. Karimi Ahmadabad, A. Shamsipour, and I. Rousta, "Identification and analysis of the north atlantic blockings," *International Journal of Current Life Sciences*, vol. 5, no. 4, pp. 577–581, 2015.
- [45] G. Azizi, H. Mohammadi, M. Karimi Ahmadabad, A. Shamsipour, and I. Rousta, "The relationship between the Arctic oscillation and North Atlantic blocking frequency," *Open Journal of Atmospheric and Climate Change*, vol. 1, pp. 1–9, 2015.
- [46] P. D. Williams, "A proposed modification to the Robert-Asselin time filter," *Monthly Weather Review*, vol. 137, no. 8, pp. 2538–2546, 2009.
- [47] Y. G. Rahimi, *Synoptic Analysis with GrADS Software*, vol. 2, SAHA Danesh Press, Tehran-Iran, 1st edition, 2016, in Persian.
- [48] G. Keykhosrowi and H. Lashkari, "Analysis of the relationship between the thickness and height of the inversion and the severity of air pollution in Tehran," *Journal of Geography and Planning*, vol. 18, no. 9, pp. 231–257, 2014.

- [49] G. R. Janbaz Ghobadi, A. Mofidi, and A. Zarrin, "Identify synoptic patterns of heavy rainfall in the summer on the southern shores of the Caspian Sea," *Geography and Planning*, vol. 22, no. 2, pp. 23–39, 2011.
- [50] I. Rousta, F. K. Akhlagh, M. Soltani, and S. S. M. Taheri, "Assessment of blocking effects on rainfall in northwestern Iran," in *Proceedings of COMECAP 2014*, p. 291, Crete University Press, Heraklion, Greece, 2014.
- [51] B. Alijani, A. Mofidi, Z. Jafarpour, and A. Aliakbari-Bidokhti, "Atmospheric circulation patterns of the summertime rainfalls of southeastern Iran during July 1994," *Earth and Space physics*, vol. 37, no. 3, pp. 205–227, 2012.
- [52] H. Golmohammadian and M. R. Pishvaei, "Production of daily rotation index and its effect on temperature and precipitation of Khorasan region in the period of 1948-2010," *Journal of Applied researches in Geographical Sciences*, vol. 13, no. 29, pp. 217–236, 2013.

## Research Article

# Links between Temperature Biases and Flow Anomalies in an Ensemble of CNRM-CM5.1 Global Climate Model Historical Simulations

O. Lhotka <sup>1,2</sup> and A. Farda <sup>1</sup>

<sup>1</sup>Global Change Research Institute, Czech Academy of Sciences, Brno, Czech Republic

<sup>2</sup>Institute of Atmospheric Physics, Czech Academy of Sciences, Prague, Czech Republic

Correspondence should be addressed to O. Lhotka; [lhotka.o@czechglobe.cz](mailto:lhotka.o@czechglobe.cz)

Received 14 February 2018; Revised 6 June 2018; Accepted 24 June 2018; Published 19 July 2018

Academic Editor: Anthony R. Lupo

Copyright © 2018 O. Lhotka and A. Farda. This is an open access article distributed under the Creative Commons Attribution License, which permits unrestricted use, distribution, and reproduction in any medium, provided the original work is properly cited.

The aim of this study was to evaluate temperature and sea-level pressure (SLP) fields and to analyse a related anomalous flow over midlatitudes simulated by the CNRM-CM5.1 global climate model (GCM). Simulated flow over midlatitudes of the Northern Hemisphere was assessed through flow indices, classified into 11 circulation types. Reference data were taken from the NOAA-CIRES 20th Century Reanalysis, version 2c. CNRM-CM5.1 exhibited analogous temperature biases to those reported for the mean of the CMIP5 GCMs' ensemble. The most prominent features were an erroneous temperature dipole pattern in the Atlantic Ocean and a warm bias over regions of deep water upwelling (locally exceeding 5°C). The latter feature was associated with negative SLP biases in those regions. Too low pressure was found over midlatitudes of the Northern Hemisphere, and CNRM-CM5.1 simulated too frequent zonal flow in these latitudes. The usage of three ensemble members with different initial conditions did not improve model's outputs because the bias is found to be considerably larger compared to the ensemble members' spread. The study showed that temperature and SLP biases are connected in certain regions, suggesting that improvement of GCMs and development of bias correction methods should be carried out with a complex insight.

## 1. Introduction

Projections of a possible future climate and advanced understanding of the climate system largely depend on global climate models (GCMs). Although considerable effort has been made on their improvement over past decades, current generation of GCMs still suffers from errors that lower the credibility of their simulations and bring considerable uncertainties in future climate projections [1, 2]. Wang et al. [3] reported that CMIP5 GCMs tend to underestimate an intensity of Atlantic meridional overturning circulation (AMOC) [4] and linked this deficiency to cold biases in the Northern Hemisphere and warm biases over the Southern Ocean. Majahan [5] suggested that the decreased AMOC is related to an increased sea ice extent in the Arctic and may have contributed to a too slow decline of the Arctic sea ice since 1979 simulated by

CMIP5 GCMs [6]. In addition, CMIP5 GCMs are not able to reproduce the changes of a sea ice around the Antarctic properly [7].

Possible connections between these large-scale oceanic factors and climate in distant regions have been widely analysed. Many studies assessed possible links between the observed rapid Arctic sea ice loss and modified atmospheric circulation in the Northern midlatitudes [8–10], with consequent impacts on wintertime temperatures [11, 12]. European temperatures seem to be also related to sea surface temperature (SST) anomalies in the North Atlantic Ocean [13], and even a more distant connection was found by Zhou and Wu [14] who concluded that heat waves over Eurasia are influenced also by El Niño-Southern Oscillation.

Differences in SST among individual GCMs can explain the majority of the intermodel variability in intensity

changes of Walker and Hadley circulation cells [15]. This uncertainty propagates to projections of atmospheric circulation and other meteorological variables, such as precipitation and temperature. Moreover, Shepherd [16] concluded that the effect of increased global temperature on atmospheric circulation is not clear, suggesting that climate change in certain regions may possibly be dominated rather by circulation changes than background warming.

Besides these models' drawbacks, climate projections are affected by uncertainties originating from the choice of the emission scenario and from the internal variability of climate [17]. Emission scenarios represent possible ways of human society's development that alter the radiative forcing on climate [18], mainly through a modification of atmospheric chemistry and land-cover changes. In midlatitudes, the uncertainty related to the internal climate variability is primarily associated with atmospheric dynamics, dominated by teleconnection modes [19], such as the North Atlantic Oscillation [20].

The aim of this study was to evaluate global patterns of sea-level pressure (SLP) in relation to a simulated temperature bias. In order to better understand possible dynamic causes of biases in temperature over Northern midlatitudes, we also analysed differences between observed and simulated flow indices over three regions there. Historical simulations of the CNRM-CM5.1 GCM [2] were used, and spatial characteristics of SLP and temperature fields are investigated in three ensemble members (initial condition ensemble), which allows analysing the natural variability simulated by the model. Simulated flow and temperature characteristics are evaluated against the NOAA-CIRES 20th Century Reanalysis, version 2c, which is available since 1851.

## 2. Data and Methods

**2.1. CNRM-CM5.1 Global Climate Model.** CNRM-CM5.1 GCM simulations performed by the Czech Hydrometeorological Institute were used. The simulations are available for the extended 1740–2005 period at 6-hour temporal resolution. We used daily means of SLP (averaged 4 daily values) and monthly means of air temperature 2 meters above the surface. The CNRM-CM5.1 GCM was developed by CNRM-GAME (Centre National de Recherches Météorologiques-Groupe d'études de l'Atmosphère Météorologique) and Cerfacs (Centre Européen de Recherche et de Formation Avancée). The GCM contains the ARPEGE-Climat atmosphere component, the NEMO oceanic model, and the GELATO sea-ice component. Three ensemble members of the ARPEGE-Climat atmosphere model with different initial conditions are used. Their horizontal spatial resolution is roughly 150 km (T127) with global coverage, and the model has 31 vertical levels. Although the model performs considerably better compared to its predecessor, substantial errors in seasonal precipitation and cloud radiative forcing are still present, including the double intertropical convergence zone, the critical underestimation of low clouds on the eastern side of the tropical ocean basins, or

the lack of cloudiness over the Northern Hemisphere continents [2]. In addition, Huszar et al. [21] revealed too large Arctic sea ice extent in this GCM. More detailed information about CNRM-CM5.1 is available in the study by Voltaire et al. [2].

**2.2. NOAA-CIRES 20th Century Reanalysis.** Model simulations were evaluated against the NOAA-CIRES 20th Century Reanalysis V2c. It provides a global analysis of the most likely state of the atmosphere since 1851 at 6-hourly temporal resolution, and it is available in the  $192 \times 94$  Gaussian grid [22]. Identical variables (temperature 2 meters above the surface and SLP) were taken in order to evaluate the CNRM-CM5.1 simulations. Seasonal and annual averages of SLP and temperature from CNRM-CM5.1 were interpolated to the aforementioned  $192 \times 94$  Gaussian grid using the ordinary kriging method, allowing a direct comparison with the reanalysis.

**2.3. Assessment of Model Biases and Circulation Types.** We analysed both annual and seasonal global patterns of SLP and temperature bias for the 50-year-long 1956–2005 period. Moreover, globally averaged temperature biases for various time periods (since 1851) were also calculated. Besides the biases, differences among individual ensemble members were also visualised.

SLP biases were associated with anomalous flows in the simulated data, which were quantified through flow indices (flow strength, direction, and vorticity) [23, 24]. The flow indices were calculated identically for both CNRM-CM5.1 and NOAA-CIRES 20th Century Reanalysis V2c using SLP in 16 points, evenly distributed over analysed regions (North America, Europe, and East Asia; Figure 1).

The flow strength (STR) is a vector sum of zonal ( $w$ ) and meridional ( $s$ ) flow components (1), and  $f$  represents the latitude of the centre ( $50^\circ\text{N}$ ). SLP values (hPa) in individual points from Figure 1 are indicated by  $p1$ – $p16$  in the following equations:

$$\begin{aligned} \text{STR} &= \sqrt{w^2 + s^2}, \\ w &= 0.5 \times (p4 + p5) - 0.5 \times (p12 + p13), \\ s &= \frac{1}{\cos(\varphi \times (\pi/180))} \times (0.25 \times (p13 + 2 \times p9 + p5) \\ &\quad - 0.25 \times (p12 + 2 \times p8 + p4)). \end{aligned} \quad (1)$$

The flow direction (DIR) is calculated using an  $\text{arctg2}(w, s)$  function (2). It is similar to the inverse tangent, except that the signs of both arguments ( $w, s$ ) are used to determine the quadrant of the result:

$$\text{DIR} = \text{arctg2}\left(\frac{w}{s}\right). \quad (2)$$

Finally, the total vorticity (VORT) is the sum of its zonal ( $zw$ ) and meridional ( $zs$ ) components of vorticity (3):

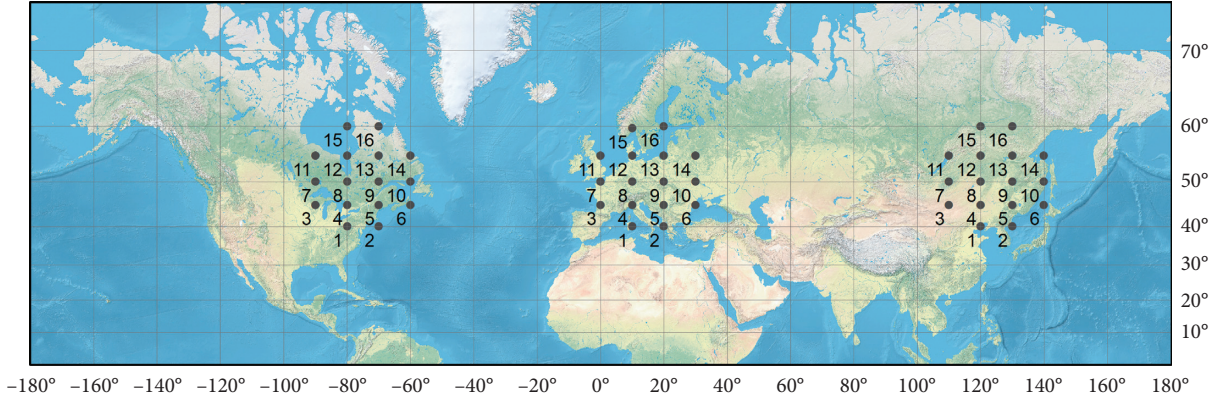


FIGURE 1: Location of grid points used for the calculation of flow indices over North America, Europe, and East Asia.

$$\text{VORT} = zw + zs,$$

$$zw = \frac{\sin(\varphi \times (\pi/180))}{\sin((\varphi - 5) \times (\pi/180))} \times (0.5 \times (p1 + p2) - 0.5 \times (p8 + p9)) - \frac{\sin(\varphi \times (\pi/180))}{\sin((\varphi + 5) \times (\pi/180))} \times (0.5 \times (p8 + p9) - 0.5 \times (p15 + p16)),$$

$$zs = \frac{1}{2 \times (\cos(\varphi \times (\pi/180)))^2} \times (0.25 \times (p14 + 2 \times p10 + p6) - 0.25 \times (p13 + 2 \times p9 + p5) - 0.25 \times (p12 + 2 \times p5 + p4) + 0.25 \times (p11 + 2 \times p7 + p3)).$$

(3)

Based on these indices, 11 circulation types were calculated. If the STR (flow strength) and the absolute value of VORT (total vorticity) are lower than 3, a pressure pattern is unclassified (U). When the absolute value of VORT is at least four times larger compared to STR, a pressure pattern is classified as cyclonic (C, if the vorticity is positive) or anticyclonic (A, if the vorticity is negative). When the aforementioned conditions are not met, the pressure pattern is classified based on DIR (the flow direction) into one of the 8 directional types (N, NE, E, SE, S, SW, W, and NW).

### 3. Global Patterns of Temperature and Sea-Level Pressure Biases

The negative bias of annual global temperature in CNRM-CM5.1 (approximately 2.8°C) was found during all examined time periods (Table 1), and its magnitude was almost identical among the individual ensemble members.

Spatial patterns of annual temperature in CNRM-CM5.1 for the 1956–2005 period are shown in Figure 2(a).

TABLE 1: Annual global temperature (°C) in the NOAA-CIRES 20th Century Reanalysis (V2c), in the CNRM-CM5.1 ensemble mean, and in its individual ensemble members (E1–E3) during four time periods.

Period	20th Century Reanalysis V2c (°C)	CNRM-CM (°C)	E1 (°C)	E2 (°C)	E3 (°C)
1980–2005	14.7	12.0 (–2.7)	11.9	12.0	12.0
1956–2005	14.6	11.8 (–2.8)	11.8	11.8	11.8
1906–2005	14.4	11.6 (–2.8)	11.6	11.6	11.6
1851–2005	14.3	11.5 (–2.8)	11.5	11.5	11.5

Temperature biases in the CNRM-CM5.1 ensemble mean are shown in brackets.

Compared to the NOAA-CIRES 20th Century Reanalysis, the CNRM-CM5.1 ensemble mean captured main features reasonably well, but biases were too pronounced in certain regions (Figure 2(b)). Over land, a negative bias prevails, especially over polar regions (both the Arctic and Antarctic) and high-altitude areas. The magnitude of this bias was roughly 5°C, but it reached 10°C in several grid points over the Tibetan Plateau and the Antarctic. Larger terrestrial areas with a positive bias (1–3°C) were present only over eastern parts of North America. Oceans generally exhibit a cold bias in the Northern Hemisphere and a warm bias in the south. The largest positive bias (around 3°C, locally exceeding 5°C) was found over the eastern Pacific Ocean, the southeastern Atlantic Ocean, and the Southern Ocean and in the Baffin and Hudson Bays. A bias with a similar magnitude but opposite sign was located over northern Pacific Ocean, northern Atlantic Ocean, and Arctic Ocean. The described overall temperature biases were similar for all ensemble members, especially in the Tropics, where the difference between the “warmest” and “coldest” ensemble members was only 0.1–0.3°C (Figure 2(c)). The agreement among the ensemble members was somewhat weaker in the midlatitudes, but differences larger than 1°C were still quite rare. The largest variability was found over polar regions, mainly in the Arctic where the difference between the “warmest” and “coldest” ensemble members exceeded 3°C in the Barents Sea.

Turning to SLP, CNRM-CM5.1 was able to simulate locations of atmospheric action centres (Figure 3(a)) quite

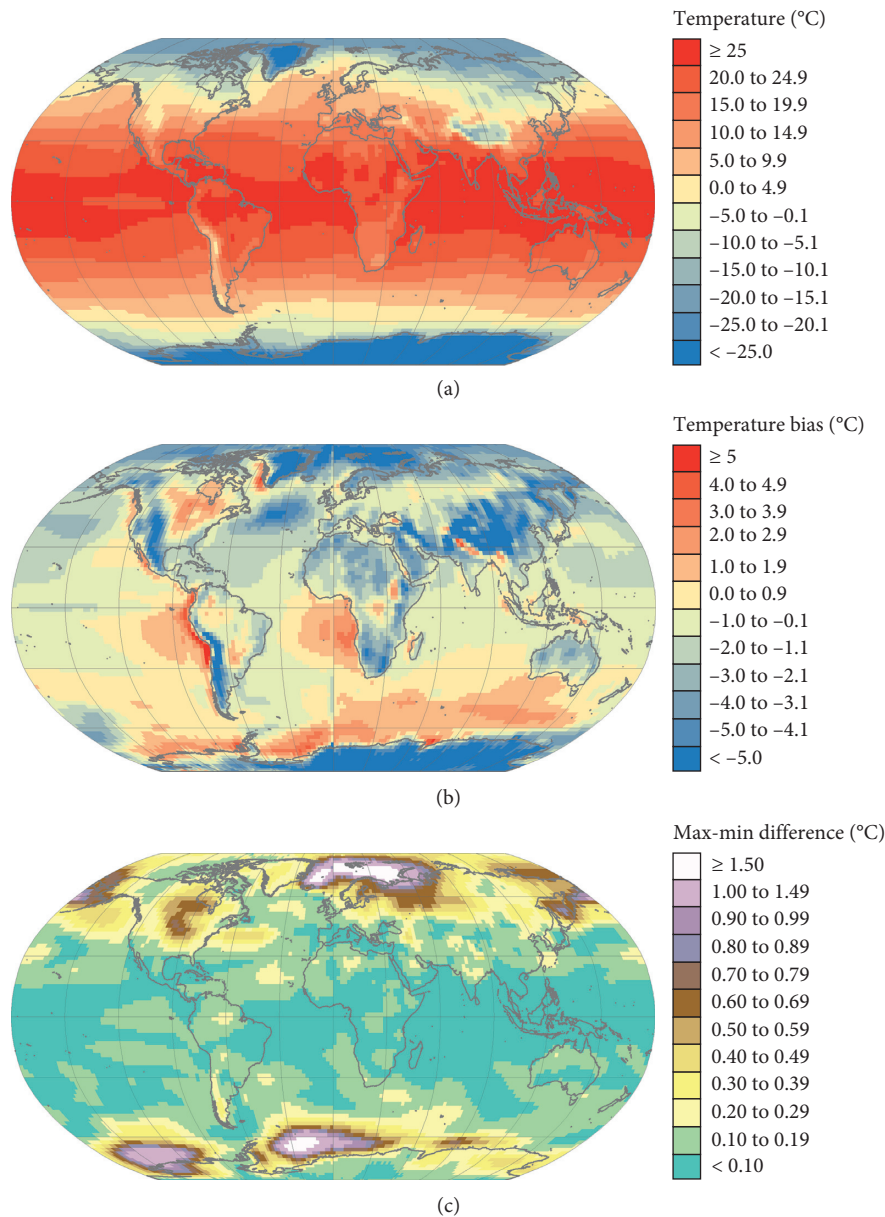


FIGURE 2: (a) Average annual 2 m temperature in the CNRM-CM5.1 ensemble mean, (b) its bias against the NOAA-CIRES 20th Century Reanalysis, version 2c, and (c) differences between “warmest” and “coldest” ensemble members in individual grid points. All maps represent the 1956–2005 period.

well; however, some notable biases were found. Over land, negative SLP bias was located in midlatitudes of the Northern Hemisphere (analysed in more detail in Section 4) and in the Antarctic (Figure 3(b)). The most distinctive negative SLP biases over oceans were found in the eastern Pacific Ocean and the southeastern Atlantic Ocean, and the biases were related to overestimated temperature in these regions. By contrast, positive SLP bias was found over western parts of the United States, Mexico, the Tibetan Plateau, the Arctic Ocean, and the Southern Ocean. Differences between ensemble members with highest/lowest SLP (in individual grid points; Figure 3(c)) are analogous to those obtained from temperature output (Figure 2(c)). The best agreement between individual ensemble members

was found in the Tropics (especially over the Indian Ocean), while the largest differences were over polar regions and in Azores and North Pacific anticyclones.

Focusing on individual seasons, the smallest global temperature bias was found during the boreal summer ( $-2.4^{\circ}\text{C}$  in the 1980–2005 period; Table 2). In the remaining seasons, the biases were somewhat larger (roughly  $-2.9^{\circ}\text{C}$ ) and quite similar. Analogously to the annual bias, seasonal biases were stable during different time periods and comparable among individual ensemble members.

The global pattern of temperature bias varied across individual seasons (Figure 4). The substantial negative bias in Greenland and Arctic, which was especially pronounced in boreal spring and winter (Figures 4(a) and 4(d)), almost

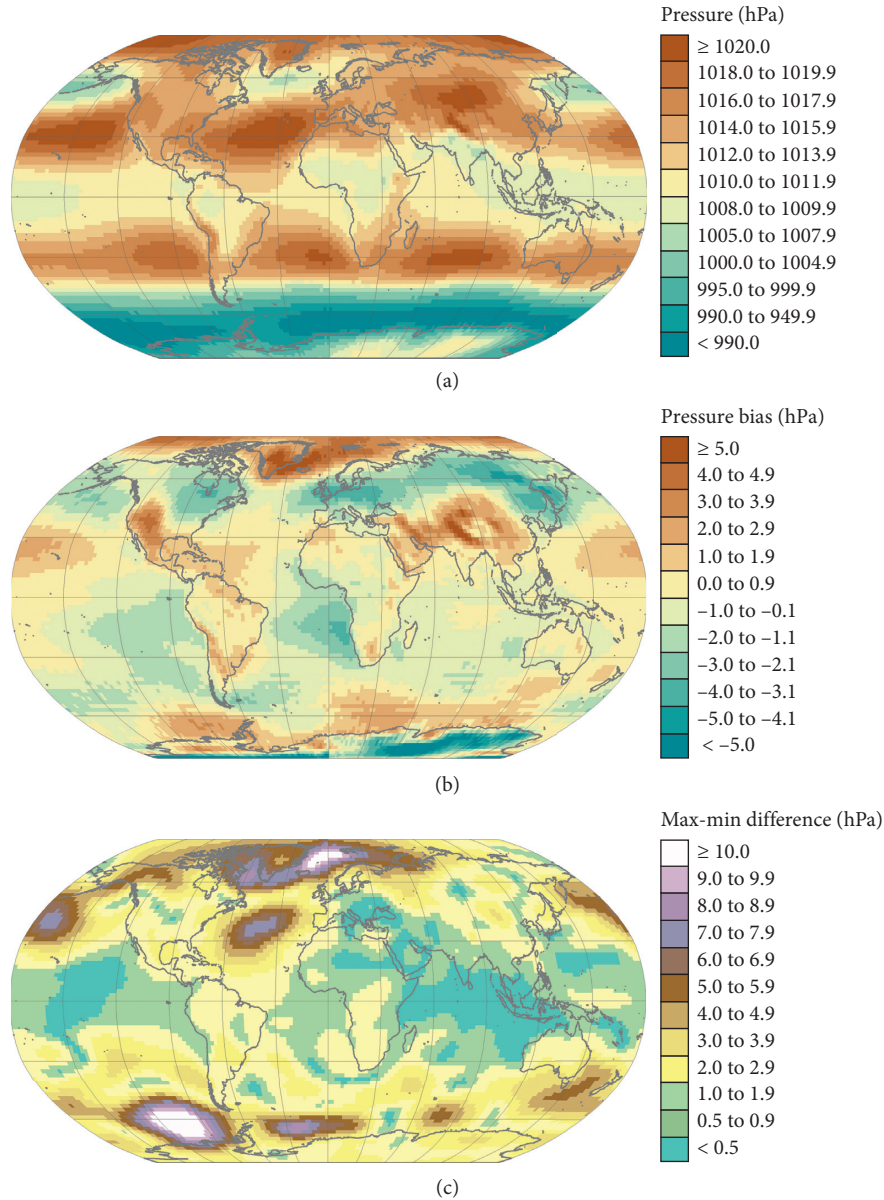


FIGURE 3: (a) Average annual sea-level pressure in the CNRM-CM5.1 ensemble mean, (b) its bias against the NOAA-CIRES 20th Century Reanalysis, version 2c, and (c) differences between ensemble members with the highest/lowest sea-level pressure value in individual grid points. All maps represent the 1956–2005 period.

TABLE 2: Seasonal temperature biases ( $^{\circ}\text{C}$ ) in the CNRM-CM5.1 ensemble mean during four time periods.

Period	MAM ( $^{\circ}\text{C}$ )	JJA ( $^{\circ}\text{C}$ )	SON ( $^{\circ}\text{C}$ )	DJF ( $^{\circ}\text{C}$ )
1980–2005	–2.9	–2.4	–2.8	–2.8
1956–2005	–2.9	–2.6	–2.9	–2.9
1906–2005	–2.9	–2.5	–2.9	–2.9
1851–2005	–2.9	–2.6	–3.0	–2.9

MAM: March 1–May 31; JJA: June 1–July 31; SON: September 1–November 30; DJF: December 1–February 28.

disappeared during boreal summer (Figure 4(b)). Analogously to the Arctic, the strong negative bias over the Antarctic was reduced in austral summer (Figure 4(d)). The aforementioned positive bias over eastern North America

was most pronounced during the boreal autumn, when its values exceeded  $5^{\circ}\text{C}$  in some grid points. The oceanic temperature bias dipole was least distinctive during boreal autumn. On the contrary, the eastern Pacific Ocean and the southeastern Atlantic Ocean regions with warm biases were relatively stable during all seasons.

No considerable differences in the magnitude of the SLP bias were found among individual seasons, except for the Antarctic Ocean and the Southern Ocean (Figure 5). The underestimated SLP in Northern midlatitudes and over the upwelling regions in the eastern Pacific Ocean and the southeastern Atlantic Ocean was also fairly stable during the year. The positive SLP bias over the western parts of the United States, Mexico, and the Tibetan Plateau was

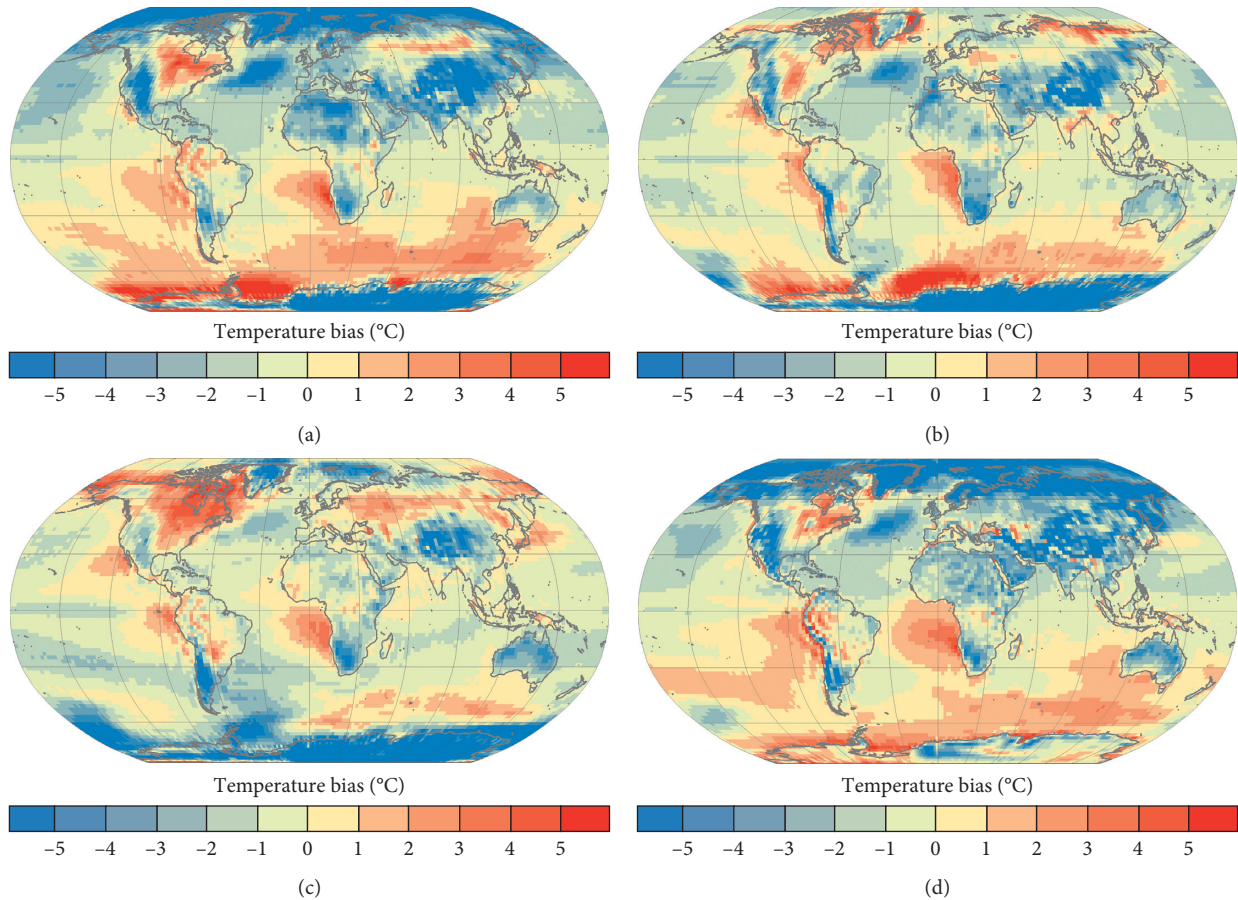


FIGURE 4: Average seasonal 2 m temperature bias in the CNRM-CM5.1 ensemble mean for the 1956–2005 period: (a) boreal spring (March–May), (b) boreal summer (June–August), (c) boreal autumn (September–November), and (d) boreal winter (December–February).

a year-round feature; however, it was least distinctive during the boreal summer.

#### 4. Northern Hemispheric Wintertime Circulation Types over Midlatitudes

In this section, we evaluated the capability of CNRM-CM5.1 to simulate seasonal frequencies of flow types over three midlatitude regions (North America, Europe, and East Asia). Over North America during winter and spring, the most frequent northerly advection (occurring on about one-fifth of days) was underestimated in all three model integrations, in which the frequency of the northern circulation type varied between 15% and 17% (Figure 6(a)). The occurrence of the types with advection from northeast was also suppressed in the simulations. By contrast, advection from west and northwest and the frequency of the cyclonic type were overestimated, indicating a too frequent zonal flow in simulated data during these seasons. These synoptic-scale anomalies can be clearly linked to biases in the mean SLP gradient over North America, that is, to the positive SLP bias over western parts of the United States and Mexico and the negative bias over Alaska and Canada (Figures 5(a) and 5(d)). Furthermore, these errors in atmospheric dynamics can be linked to positive winter temperature biases

(Figure 4(d)), since the types that are associated with the advection of relatively cold Arctic air or the development of cold continental stagnant air occur with lower frequency in the model outputs. The underestimation of northerly types was found also during summer and autumn. By contrast, CNRM-CM5.1 simulated too frequent easterly, south-easterly, and southerly advection in these seasons (Figure 6(a)). The largest temperature anomaly during autumn was not clearly related to biases in large-scale flow, and this error would be possibly associated with land-atmosphere interactions.

Too frequent westerly advection was also found over Europe (except during the summer season; Figure 6(b)). Its observed frequency during winter (20%) was considerably overestimated in CNRM-CM5.1, ranging from 25% to 27%. This overestimation is less pronounced in the transient seasons (spring and autumn), and the summertime frequency of the westerly flow type is underestimated in CNRM-CM5.1. The model also simulated too frequent south-westerly advection, while the frequency of easterly and south-easterly circulation types was underestimated (except in summer). Interestingly, these errors did not result in a notable wintertime positive temperature bias over Europe, probably due to underestimated temperature in the North Atlantic Ocean in the model simulations.

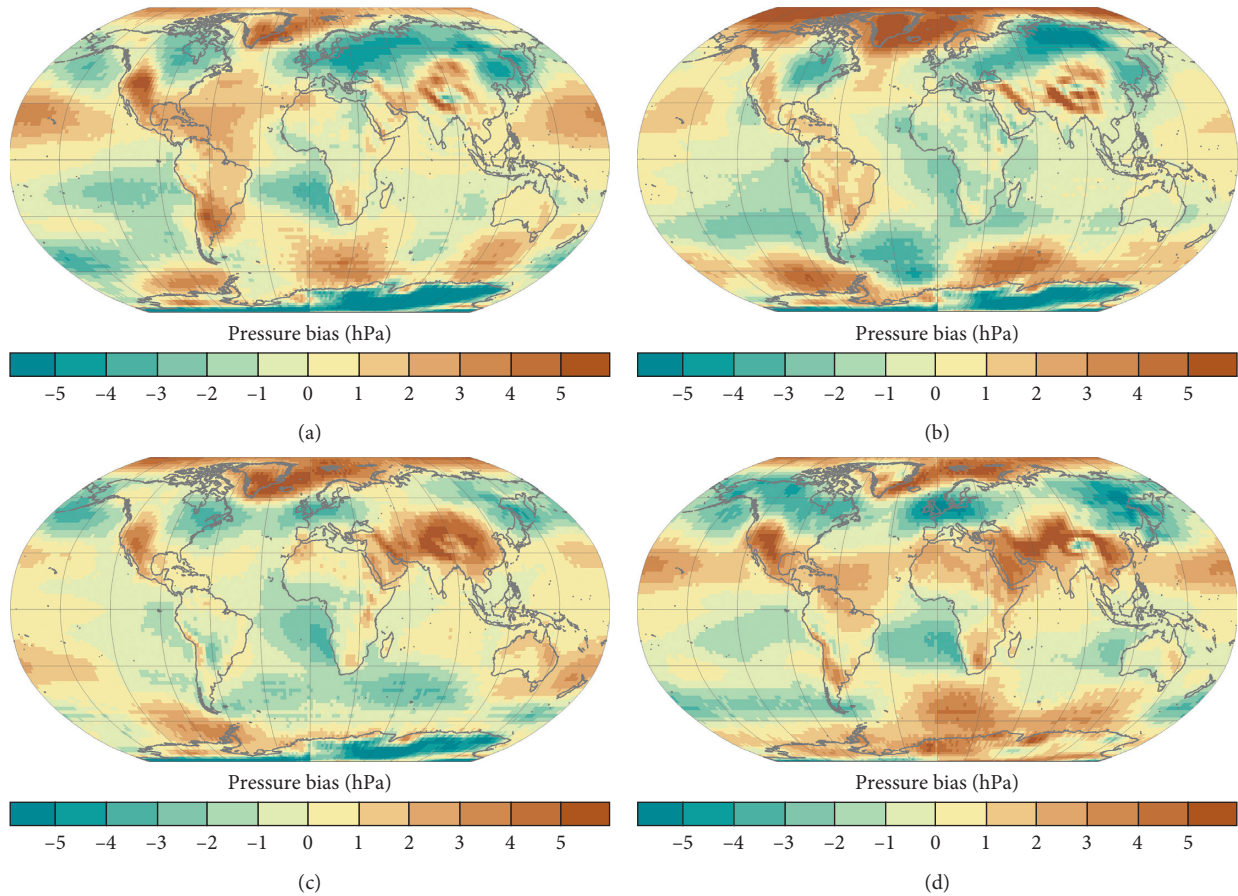


FIGURE 5: Average seasonal sea-level pressure bias in the CNRM-CM5.1 ensemble mean for the 1956–2005 period: (a) boreal spring (March–May), (b) boreal summer (June–August), (c) boreal autumn (September–November), and (d) boreal winter (December–February).

Over East Asia, CNRM-CM5.1 simulated the prevailing wintertime monsoon-related northerly advection quite well (Figure 6(c)); however, the frequencies of the northwestern and western circulation types were markedly overestimated at the expense of the northeastern circulation type. The latter is linked to the bias in the zonal SLP gradient (Figure 5(d)). By contrast, CNRM-CM5.1 failed to simulate the prevailing southerly advection associated with monsoon during summer. The frequency of the southerly type was almost halved in CNRM-CM5.1 compared to the reanalysis.

In all, too frequent zonal flow was found across the Northern midlatitudes. This bias is clearly associated with overestimated/underestimated SLP in two belt-shaped patterns, one between about 20 and 30°N and the other around about 55°N (Figure 5(d)). Furthermore, the underestimated SLP in midlatitudes is linked to the overestimated (underestimated) frequency of strongly cyclonic (anticyclonic) circulation types in all examined regions (Figure 6).

## 5. Discussion

CNRM-CM5.1 exhibited similar temperature biases as have been shown for the CMIP5 multimodel mean, with respect to their spatial patterns and magnitude [25]. Pronounced warm biases were found over upwelling regions in the

southeastern Atlantic Ocean and Pacific Ocean. This bias was already reported for the CMIP3 GCMs, and it was linked to erroneous southward displacement of the intertropical convergence zone, subsequent modification of westerly winds, and deepened thermocline, which reduce upwelling of cold water. In addition, the bias is related also to improper simulation of low-altitude clouds in these regions [26]. An analogous issue was reported for CMIP5 simulations [27], and Wang et al. [3] revealed other interhemispheric links between these warm biases and distant large-scale factors, such as weaker monsoons in the Northern Hemisphere. Therefore, a reduction of these biases cannot be based on correction of regional processes only but has to be carried out with a complex insight.

Another notable deficiency of CMIP5 GCMs (including CNRM-CM5.1) is the oceanic bias dipole, probably originating from a weakened northward heat transport due to a reduced AMOC [3], resulting in the warmer Southern Ocean and the colder North Atlantic Ocean compared to the reference data. The cold bias over the North Atlantic may possibly be related to the persisting negative phase of Atlantic multidecadal oscillation [28] in the model outputs. CMIP3 GCMs, however, have difficulties to simulate this feature, mainly due to a low signal-to-noise ratio and a long period of oscillation [29], and it is possible that

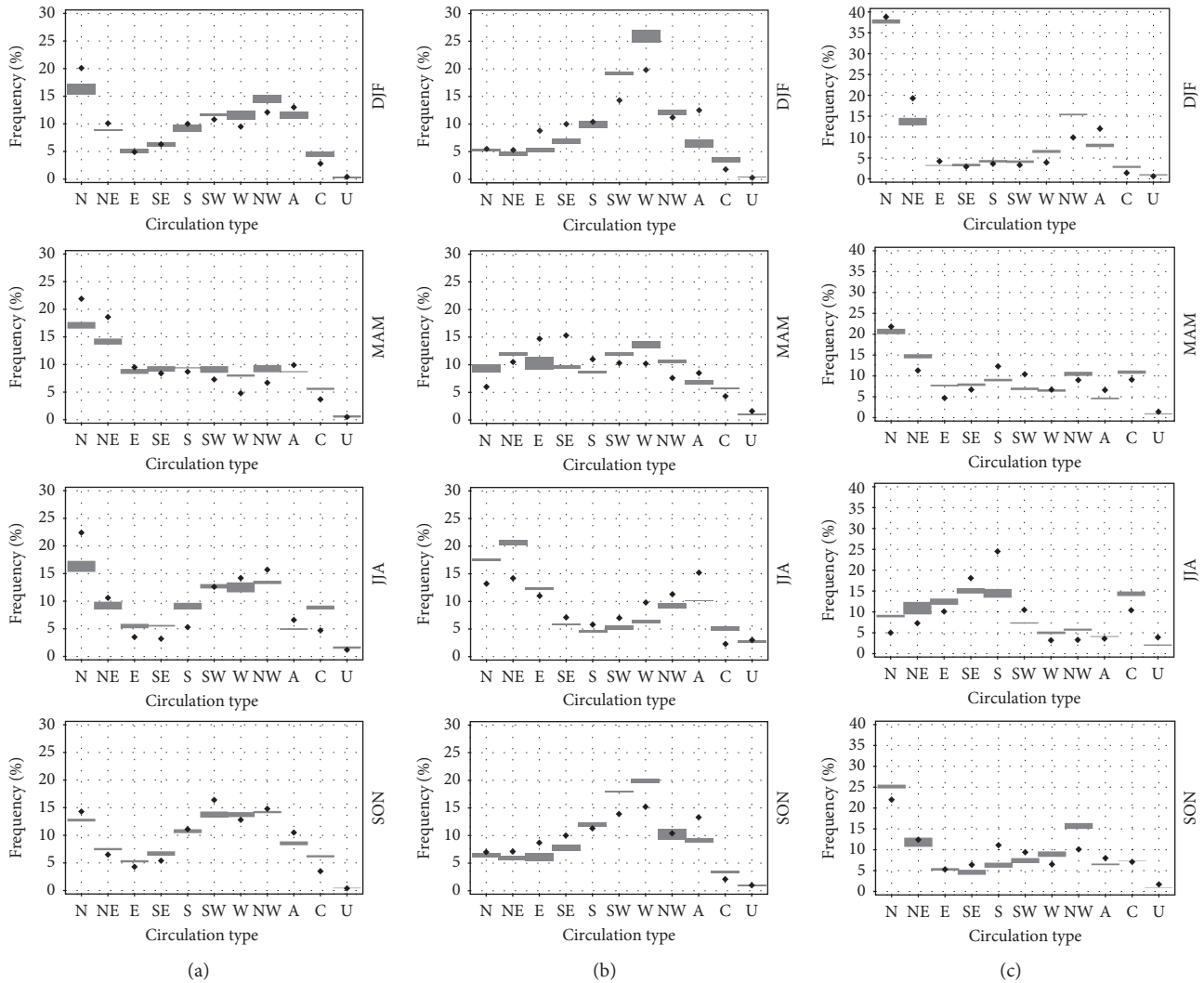


FIGURE 6: Mean wintertime frequency of circulation types in NOAA-CIRES 20th Century Reanalysis (black dots) over (a) North America, (b) Europe, and (c) East Asia. Grey bands indicate a span between individual ensemble members in CNRM-CM5.1 for each circulation type.

CNRM-CM5.1 suffers from the same deficiency as well. The negative temperature bias in northern Atlantic and Europe may also possibly be linked to improper simulation of Gulf Stream, which carries warm water erroneously towards the Canadian Archipelago with consequent impacts on the simulated North American climate. Huszar et al. [21] reported an overestimated sea ice extent in the CNRM-CM5.1, which may explain the strong cold bias over the Arctic Ocean in spring and winter found in our study.

Besides polar regions, considerable negative temperature biases over land were found over mountainous areas, which is in accordance with IPCC [25] and Su et al. [30] who evaluated the performance of CMIP5 GCMs over the Tibetan Plateau and suggested that the negative bias may be linked to snow-cover feedback processes in the models. Besides these physical processes, however, the bias may be affected by a simple representation of orography or a lack of observed data in these remote areas that affects the performance of the reanalysis. In addition, it should be noted that the magnitude of biases may be influenced by a selection

of reference data (i.e., the NOAA-CIRES 20th Century Reanalysis V2c), inasmuch as Stryhal and Huth [31] showed that the choice of different reanalyses can have a profound effect on GCM validation over Europe in winter.

Temperature differences between individual ensemble members are relatively small on the global scale, which is in accordance with Kharin et al. [32], who showed that a spread between individual GCMs was larger compared to the difference between ensemble members of one particular GCM. In our study, the difference between the ensemble members in simulating temperature was smallest over equatorial areas and gradually increased poleward. The largest discrepancies were found over polar oceans, in accordance with Kharin et al. [32], and may be related to different boundaries of sea ice extent in individual ensemble members that would considerably alter a surface climate.

Small differences among the individual ensemble members were found also when assessing differences in sea-level pressure fields (except polar regions) and frequencies of circulation types over North America, Europe,

and East Asia. The common deficiency in these three regions was an overestimated frequency of zonal flow, which is probably associated with the known issue of GCMs not being able to correctly simulate the occurrence of atmospheric blocking [33, 34].

## 6. Conclusions

We evaluated temperature and SLP biases and frequency of circulation types in three historical ensemble members of CNRM-CM5.1 GCM against the NOAA-CIRES 20th Century Reanalysis. The main conclusions are summarised as follows:

- (i) The CNRM-CM5.1 model had a relatively good skill in reproducing global temperature patterns; however, it exhibited drawbacks similar to those reported for other CMIP5 GCMs. An oceanic bias dipole pattern is present in CNRM-CM5.1, resulting in a too warm Southern Ocean and an excessively cold North Atlantic Ocean and Arctic Ocean.
- (ii) Another deficiency shared with the majority of CMIP5 models is a positive temperature bias in upwelling regions along western coasts of Africa and Southern America (locally exceeding 5°C). This temperature bias was associated with too low sea-level pressure in these regions.
- (iii) The most apparent biases were present in all three ensemble members, regardless of the member's initial conditions, and, therefore, are rather a result of model errors than simulated natural variability. This holds not only for mean seasonal and annual temperature and SLP patterns but even for the considerably more chaotic and variable synoptic-scale circulation over three northern midlatitude regions.
- (iv) CNRM-CM5.1 overestimated the frequency of zonal flow over North America, Europe, and East Asia. The considerable positive wintertime temperature bias in North America was associated with suppressed northerly advection of cold air from the Arctic in CNRM-CM5.1 and was found in all ensemble members.

## Data Availability

The outputs of the CNRM-CM5.1 global climate model can be obtained from the ESFG data node (<https://esg-dn1.nsl.liu.se/projects/esgf-liu/>). NOAA-CIRES 20th Century Reanalysis V2c is available through the ESRL website ([https://www.esrl.noaa.gov/psd/data/gridded/data.20thC\\_ReanV2c.html](https://www.esrl.noaa.gov/psd/data/gridded/data.20thC_ReanV2c.html)).

## Conflicts of Interest

The authors declare that there are no conflicts of interest regarding the publication of this article.

## Acknowledgments

This work was supported by the Ministry of Education, Youth and Sports of the Czech Republic within the National Sustainability Program I (NPU I), Grant no. LO1415. The authors acknowledge the CNRM-CM5.1 global climate model developed by CNRM-GAME (Centre National de Recherches Météorologiques-Groupe d'études de l'Atmosphère Météorologique) and Cerfacs (Centre Européen de Recherche et de Formation Avancée). The authors also acknowledge the Twentieth Century Reanalysis Project version 2c dataset that is provided by the U.S. Department of Energy, Office of Science Biological and Environmental Research (BER), and by the National Oceanic and Atmospheric Administration Climate Program Office. The authors thank Jan Stryhal, Institute of Atmospheric Physics, Prague, for his valuable comments on the draft of the paper.

## References

- [1] J. Sillmann, V. V. Kharin, X. Zhang, F. W. Zwiers, and D. Bronaugh, "Climate extremes indices in the CMIP5 multimodel ensemble: part 1. Model evaluation in the present climate," *Journal of Geophysical Research: Atmospheres*, vol. 118, no. 4, pp. 1716–1733, 2013.
- [2] A. Voldoire, E. Sanchez-Gomez, D. Salaz y Mélia et al., "The CNRM-CM5.1 global climate model: description and basic evaluation," *Climate Dynamics*, vol. 40, no. 9–10, pp. 2091–2121, 2013.
- [3] C. Wang, L. Zhang, and S. Lee, "A global perspective on CMIP5 climate model biases," *Nature Climate Change*, vol. 4, no. 3, pp. 201–205, 2014.
- [4] K. E. Taylor, R. J. Stouffer, and G. A. Meehl, "An overview of CMIP5 and the experiment design," *Bulletin of the American Meteorological Society*, vol. 93, no. 4, pp. 485–498, 2012.
- [5] S. Majahan, "Impact of the Atlantic meridional overturning circulation (AMOC) on Arctic surface air temperature and sea ice variability," *Journal of Climate*, vol. 24, no. 24, pp. 6573–6581, 2011.
- [6] J. C. Stroeve, V. Kattsov, A. Barrett et al., "Trends in Arctic sea ice extent from CMIP5, CMIP3 and observations," *Geophysical Research Letters*, vol. 39, no. 16, pp. 1–7, 2012.
- [7] J. Turner, T. J. Bracegirdle, T. Phillips et al., "An initial assessment of Antarctic sea ice extent in the CMIP5 models," *Journal of Climate*, vol. 26, no. 5, pp. 1473–1484, 2013.
- [8] R. Jaiser, K. Dethloff, D. Handorf et al., "Impact of sea ice cover changes on the Northern Hemisphere atmospheric winter circulation," *Tellus A: Dynamic Meteorology and Oceanography*, vol. 64, no. 1, p. 11595, 2012.
- [9] J. Screen, I. Simmons, C. Deser, and R. Tomas, "The atmospheric response to three decades of observed Arctic sea ice loss," *Journal of Climate*, vol. 26, no. 4, pp. 1230–1248, 2012.
- [10] J. A. Francis, S. J. Vavrus, and J. Cohen, "Amplified Arctic warming and mid-latitude weather: new perspectives on emerging connections," *Wiley Interdisciplinary Reviews: Climate Change*, vol. 8, no. 5, p. e474, 2017.
- [11] S. Yang and J. H. Christensen, "Arctic sea ice reduction and European cold winters in CMIP5 climate change experiments," *Geophysical Research Letters*, vol. 39, no. 20, article L20707, 2012.
- [12] Q. Tang, X. Zhang, X. Yang, and J. A. Francis, "Cold winter extremes in northern continents linked to Arctic sea ice loss,"

- Environmental Research Letters*, vol. 8, no. 1, article 014036, 2013.
- [13] R. T. Sutton and B. Dong, "Atlantic Ocean influence on a shift in European climate in the 1990s," *Nature Geoscience*, vol. 5, no. 11, pp. 788–792, 2012.
- [14] Y. Zhou and Z. Wu, "Possible impacts of mega-El Niño/Southern Oscillation and Atlantic multidecadal oscillation on Eurasian heatwave frequency variability," *Quarterly Journal of the Royal Meteorological Society*, vol. 142, no. 697, pp. 1647–1661, 2016.
- [15] J. Ma and S. P. Xie, "Regional patterns of sea surface temperature change: a source of uncertainty in future projections of precipitation and atmospheric circulation," *Journal of Climate*, vol. 26, no. 8, pp. 2482–2501, 2013.
- [16] T. G. Shepherd, "Atmospheric circulation as a source of uncertainty in climate change projections," *Nature Geoscience*, vol. 7, no. 10, pp. 703–708, 2014.
- [17] E. Hawkins and R. Sutton, "The potential to narrow uncertainty in regional climate predictions," *Bulletin of the American Meteorological Society*, vol. 90, no. 8, pp. 1095–1107, 2009.
- [18] R. H. Moss, J. A. Edmonds, K. A. Hibbard et al., "The next generation of scenarios for climate change research and assessment," *Nature*, vol. 463, no. 7282, pp. 747–756, 2010.
- [19] C. Deser, A. Phillips, V. Bourdette, and H. Teng, "Uncertainty in climate change projections: the role of internal variability," *Climate Dynamics*, vol. 38, no. 3-4, pp. 527–546, 2012.
- [20] J. W. Hurrell and C. Deser, "North Atlantic climate variability: the role of the North Atlantic Oscillation," *Journal of Marine Systems*, vol. 79, no. 3-4, pp. 231–244, 2010.
- [21] P. Huszar, H. Teyssède, M. Michou et al., "Modeling the present and future impact of aviation on climate: an AOGCM approach with online coupled chemistry," *Atmospheric Chemistry and Physics*, vol. 13, no. 19, pp. 10027–10048, 2013.
- [22] G. P. Compo, J. S. Whitaker, P. D. Sardeshmukh et al., "The twentieth century reanalysis project," *Quarterly Journal of the Royal Meteorological Society*, vol. 137, no. 654, pp. 1–28, 2011.
- [23] A. F. Jenkinson and F. P. Collison, *An Initial Climatology of Gales over the North Sea*, Synoptic Climatology Branch Memorandum No. 62, Meteorological Office, Bracknell, UK, 1977.
- [24] S. Blenkinsop, P. D. Jones, S. R. Dorling, and T. J. Osborn, "Observed and modelled influence of atmospheric circulation on central England temperature extremes," *International Journal of Climatology*, vol. 29, no. 11, pp. 1642–1660, 2009.
- [25] International Panel on Climate Change (IPCC), *Climate Change 2013: The Physical Science Basis*, Cambridge University Press, Cambridge, UK, 2013.
- [26] I. Richter and S.-P. Xie, "On the origin of equatorial Atlantic biases in coupled general circulation models," *Climate Dynamics*, vol. 31, no. 5, pp. 587–598, 2008.
- [27] I. Richter, S.-P. Xie, S. K. Behera et al., "Equatorial Atlantic variability and its relation to mean state biases in CMIP5," *Climate Dynamics*, vol. 42, no. 1-2, pp. 171–188, 2014.
- [28] Y. Peings, G. Simpkins, and G. Magnusdottir, "Multidecadal fluctuations of the North Atlantic Ocean and feedback on the winter climate in CMIP5 control simulations," *Journal of Geophysical Research: Atmospheres*, vol. 121, no. 6, pp. 2571–2592, 2016.
- [29] A. Stoner, K. Hayhoe, and D. Wuebbles, "Assessing general circulation model simulations of atmospheric teleconnection patterns," *Journal of Climate*, vol. 22, no. 16, pp. 4348–4372, 2009.
- [30] F. Su, X. Duan, D. Chen et al., "Evaluation of the global climate models in the CMIP5 over the Tibetan Plateau," *Journal of Climate*, vol. 26, no. 10, pp. 3187–3208, 2013.
- [31] J. Stryhal and R. Huth, "Classifications of winter Euro-Atlantic circulation patterns: an intercomparison of five atmospheric reanalyses," *Journal of Climate*, vol. 30, no. 19, pp. 7847–7861, 2017.
- [32] V. V. Kharin, F. W. Zwiers, X. Zhang, and G. C. Hegerl, "Changes in temperature and precipitation extremes in the IPCC ensemble of global coupled model simulations," *Journal of Climate*, vol. 20, no. 8, pp. 1419–1444, 2007.
- [33] A. A. Scaife, T. Woollings, J. Knight et al., "Atmospheric blocking and mean biases in climate models," *Journal of Climate*, vol. 23, no. 23, pp. 6143–6152, 2010.
- [34] M. Rohrer, M. Croci-Maspoli, and C. Appenzeller, "Climate change and circulation types in the Alpine region," *Meteorologische Zeitschrift*, vol. 26, no. 1, pp. 83–92, 2017.

## Research Article

# A New Dynamical Index for India-Burma Trough

Kui Liu,<sup>1,2</sup> Jinlin Zha,<sup>1</sup> Ruowen Yang ,<sup>1</sup> and Jilong Chen<sup>2</sup>

<sup>1</sup>Department of Atmospheric Science, Yunnan University, Kunming 650091, China

<sup>2</sup>Center for Monsoon System Research, Chinese Academy of Sciences, Beijing 100089, China

Correspondence should be addressed to Ruowen Yang; yangruowen@ynu.edu.cn

Received 3 September 2017; Revised 5 February 2018; Accepted 28 February 2018; Published 3 May 2018

Academic Editor: Anthony R. Lupo

Copyright © 2018 Kui Liu et al. This is an open access article distributed under the Creative Commons Attribution License, which permits unrestricted use, distribution, and reproduction in any medium, provided the original work is properly cited.

Based on the vertical velocity field of reanalysis datasets, this study defines a new dynamical index for the India-Burma trough and supports this index's advantages by analyzing reanalysis and observational datasets. For a convenient understanding, the vertical velocities of 5 levels ranging from 700 hPa to 500 hPa within the area of 15.625°N–24.375°N and 90.625°E–100.625°E are multiplied by  $-1$  and summed up into a time series involving each year from 1979 to 2012. The standardized value of the time series is defined as the index of India-Burma trough (IIBT). IIBT can reflect the characteristics of the annual strength and the interdecadal variation of the India-Burma trough. IIBT can also well reveal the relationship between the India-Burma trough and its upstream teleconnection. What is more, through a correlation analysis on the grid point precipitation field, respectively, with the IIBT and the India-Burma trough indices defined with vorticity and geopotential height, over southern Asia the correlation pattern between the IIBT and the precipitation field is found to nearly be the sum of the correlation patterns of the latter 2 indices with the precipitation. To the south of the TP, the correlation field between the IIBT and the grid point precipitation shows dipolar distribution, which is consistent with the correlation patterns of the IIBT with the vertical velocity, specific humidity, and the mid-level geopotential height in the same spatial location. IIBT is beneficial for more accurate study of the impact of the India-Burma trough on the associated weather and climate.

## 1. Introduction

The TP splits and merges the tropospheric westerlies. When westerlies meet the TP, the anticyclonically curved flow to the north side forms the dynamic high pressure ridge, whereas the other branch flow to the south cyclonically shapes the dynamic low pressure trough, which is named as the southern branch trough or the India-Burma trough [1]. Qin et al. [2] indicated that the India-Burma trough, also known as the subtropical westerly trough, is closely related to the upstream teleconnection and the Arabian Sea trough. The India-Burma trough appears in all seasons throughout a whole year, especially in the winter half year (December–May in the next year) with the highest frequencies [2]. From the perspective of climate, Suo and Ding [3] studied the structure and evolution characteristics of the subtropical south branch trough in the winter half year and pointed out that the India-Burma trough is the semipermanent trough of low pressure, appearing in the subtropical south branch westerly to the south of the plateau, in more detail which is over BOB in the winter half

year. The India-Burma trough is established in October over the northern BOB, which intensifies in winter and becomes active in spring and then transforms into the BOB trough in June.

The India-Burma trough is one of the most important synoptic systems affecting southern China in winter [4], whose impact on the weather and the short-term climate may even extend to the eastern China and Japan [5]. Qin et al. [2] revealed that the onset of the rainy season in southwestern China is caused by the interaction between the India-Burma trough and the cold air from high latitudes. He et al. [6] believed that the burst of the South China Sea monsoon is associated with the India-Burma trough. It supplies most of the moisture from BOB when the moisture from the western North Pacific (WNP) is interrupted to a large extent [7, 8]. Previous studies also expounded the relationship between the India-Burma trough and El Niño, through which Li et al. [9] exhibited the reason for the drought in northern and northwestern China. Zhao et al. [10] deemed that the number of days of spring sand-dust storm in northwestern China is

also linked to the India-Burma trough. Suo and Ding [3] pointed out that the India-Burma trough is connected to the onset of the summer monsoon in China. Since the India-Burma trough has an important influence on the weather and climate, it is one of the important factors for the weather forecast in China.

In order to study the India-Burma trough and its effects on the weather and climate, many scholars have defined the India-Burma trough index from different perspectives.

Zhang et al. [11] defined the India-Burma index with the averaged geopotential height in the area of 15°N–27.5°N and 80°E–100°E at 500 hPa and pointed out that the India-Burma trough was relatively strong in the winter half year from the 1950s to the 1970s. Especially in the 1960s, the trough was the strong, and after that it began to weaken. The strength of the India-Burma trough is not all the same in different periods, with quasi 17-year oscillation in the low frequency band, and quasi 3-year and quasi 8-year cycle in the medium-high frequency band [11]. Wang et al. [12] defined the India-Burma index with the averaged vorticity in the area of 15°N–25°N and 80°E–100°E at 700 hPa and pointed out that the index defined with vorticity is better than that defined by geopotential height. They pointed out the increasing tendency of the India-Burma trough strength after 1978 and further studied the differences of the India-Burma trough's impacts on the climate of South and East Asia between 1949–1977 and 1978–2010. Lu and Ren [13] agreed with the conclusion of Wang et al. [12] and further explore the fact that SST forcing is an important factor for IIBT interdecadal deepening. The India-Burma trough indices defined from different perspectives could not give an unified answer whether the trough grows stronger or weaker after 1978. Compared to other weather and climate systems of southwestern China and South Asia, the India-Burma trough is relatively active in winter and spring, and it becomes more and more important for the annual prediction of the temperature and precipitation (including drought) there. The drought occurring in the low-latitude highlands in southwestern China is frequent and widespread [14]. From the winter of 2009 to the spring in 2010, the most serious drought since 1951 occurred there [15–21]. Many researches had shown that the weak India-Burma trough resulted in less water vapor transportation from the BOB to the highlands [22–25], which is one important reason of this drought event. The variety of definitions for the India-Burma trough index illustrates that no particular physical parameter fully describes it. Therefore, the researchers could not well study its real weather and climate significance in South Asia and southwestern China, which this manuscript investigates. The data and methods used for the study are presented in Section 2. Section 3 describes the results and analysis. Conclusion and discussion are given in Section 4.

## 2. Data and Methods

For our analyses, the monthly Modern-Era Retrospective Analysis for Research and Applications (MERRA) atmospheric circulation data provided by Goddard Earth Sciences Data and Information Sciences Center (GES DISC) and

Global Modeling and Assimilation Office (GMAO) is used. MERRA is a reanalysis for the satellite era using a major new version of the Goddard Earth Observing System Data Assimilation System Version 5 (GEOS-5), which helps to study the meteorological phenomena of weather and climate time scales. The data spans from 1979 to present, with spatial resolution  $1.25^\circ \times 1.25^\circ$ , and the meteorological elements used are geopotential height, vertical velocity, horizontal wind field, and specific humidity. The precipitation data used is the Global Precipitation Climate Center (GPCC) monthly precipitation data (V6 and V4), with spatial resolution  $1^\circ \times 1^\circ$  spanning from 1979 to 2012. The monthly precipitation data of 148 stations in low-latitude highlands from 1979 to 2012 is also used, which is provided by the Climate Center of Yunnan Meteorological Administration. All the datasets are only used during winter half year (winter and spring). The correlation analysis, normalization of time series, Mann-Kendall (M-K), and Empirical Orthogonal Function (EOF) approaches are employed. We introduce the special calculation of normalization and M-K methods in the following [26].

If  $x$  series has  $n$  samples, we can get the normalization  $y$  by three steps:

$$\begin{aligned}\bar{x} &= \frac{1}{n} \sum_{i=1}^n x_i, \\ S &= \sqrt{\frac{1}{n} \sum_{i=1}^n (x_i - \bar{x})^2}, \\ y_i &= \frac{x_i - \bar{x}}{S}.\end{aligned}\quad (1)$$

For M-K method, suppose that the  $x$  series has  $n$  samples, and then construct a rank.

$$s_k = \sum_{i=1}^k r_i, \quad k = 2, 3, \dots, n, \quad (2)$$

$$r_i = \begin{cases} +1, & \text{if } (x_i > x_j) \\ 0, & \text{if } (x_i \leq x_j) \end{cases}, \quad j = 1, 2, \dots, i, \quad (3)$$

$$UF_k = \frac{[s_k - E(s_k)]}{\sqrt{\text{var}(s_k)}}, \quad k = 1, 2, \dots, n. \quad (4)$$

In formula (4)  $UF_1 = 0$ .  $E(s_k)$  and  $\text{var}(s_k)$  are the average value and variance of  $s_k$ :

$$\begin{aligned}E(s_k) &= \frac{k(k-1)}{4}, \\ \text{var}(s_k) &= \frac{k(k-1)(2k+5)}{72}, \\ &k = 2, 3, \dots, n.\end{aligned}\quad (5)$$

Then reverse  $x$ , repeat above steps, and make sure that

$$\begin{aligned}UB_k &= -UF_k \quad (k = n, n-1, \dots, 1), \\ UB_1 &= 0.\end{aligned}\quad (6)$$

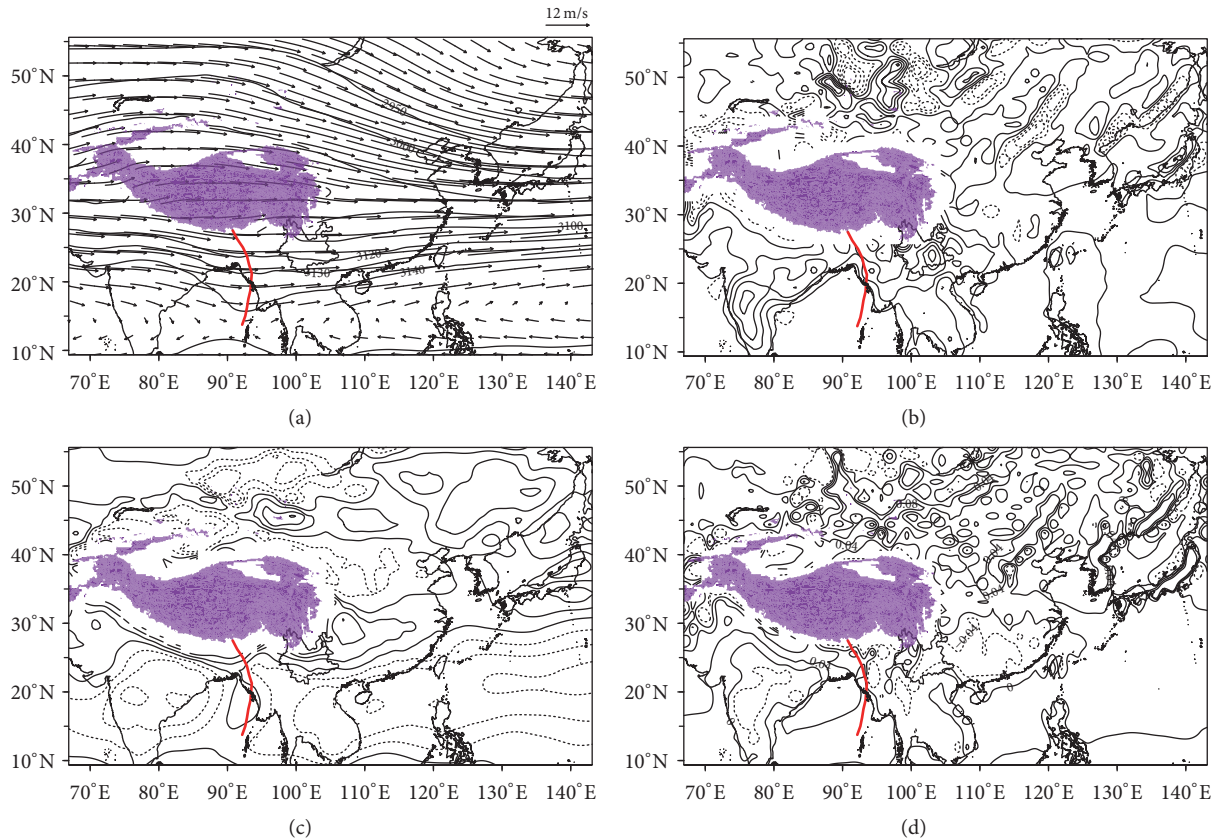


FIGURE 1: (a) The geopotential height (unit: gpm) and wind (unit:  $\text{m s}^{-1}$ ), (b) the divergence field (contour interval:  $2e - 6 \text{ s}^{-1}$ ), (c) vorticity (interval:  $5e - 6 \text{ s}^{-1}$ ), and (d) vertical velocity (interval:  $0.05 \text{ Pa s}^{-1}$ ) over 700 hPa in winter half year (from December to the next May) from 1978/1979 to 2011/2012 (written as 1979–2012). The violet area is the TP, and red line denotes trough axis (same for the following context).

The critical value of 95% significance is 1.96 and the  $UF > 0$  ( $UF < 0$ ) indicates the upward (downward) trend of the serial, with exceeding the critical value denoting the significant upward (downward) trend. The intersection point between the critical lines represents the point of mutation.

### 3. Results Analysis

**3.1. The Analysis of the Meteorological Elements in the India-Burma Trough Region.** TP is the most important topographic feature of the Asian continent. As shown in Figure 1(a), the westerlies form a northern branch to the north of TP and a southern branch in the other side, with a ridge and a trough (India-Burma trough), respectively. The India-Burma trough stretches southward from the southern hill of TP to the north of the BOB (near  $15^\circ\text{N}$ ). The trough region is located in the northern part (near  $20^\circ\text{N}$ ) of the BOB, and there is a high pressure ridge due to the terrain blocking effects on the air current over the India peninsula. When the air flow in front of the India-Burma trough enters Yunnan province, a weak ridge is formed by the terrain effects. As portrayed in Figure 1(b), at 700 hPa the divergence in front and back of the trough above the land is positive, which means divergence. Maybe because of the blocking effect of the Deccan Plateau in India on the air flow, a stationary anticyclone is located in the back of the trough (seen from Figure 1(a)), which leads to

the appearance of divergence in the back of trough, although there exists convergence in the back of trough in general, whereas the divergence over BOB is negative, displaying a convergent state. In Figure 1(c), the climatological mean of the vorticity on 700 hPa is negative to the west of the trough axis, positive at the trough axis, and negative east of the trough axis in the southern part of Yunnan. Regarding 700 hPa vertical motion (Figure 1(d)), upward vertical motion is evident east of the trough axis and sinking motion west of the trough axis. It can be seen from the distribution of the trough lines in Figure 1 that the India-Burma trough can be discerned in various meteorological element fields at 700 hPa, with obvious ascending motion in front of the trough and a clear separation of the negative (ascending) area in front of the trough and the positive (sinking) area in the trough region, in view of which the definition of the India-Burma index based on the vertical velocity in front of the trough can be a good one.

**3.2. Defining the India-Burma Trough Index with Vertical Velocity.** Wang et al. [12] defined the India-Burma trough index with the 700 hPa vorticity to study the India-Burma trough's influence on climate anomalies in East and South Asia. However, Wang et al. [12] also suggested that the India-Burma trough index could also be defined by vertical velocity downstream of the trough axis.

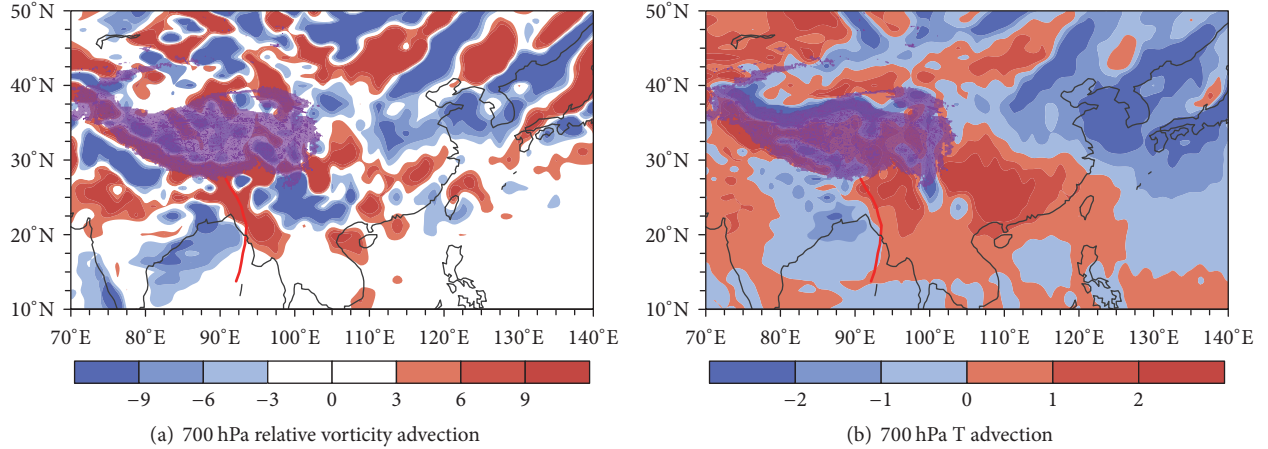


FIGURE 2: Same as Figure 1, but for 700 hPa (a) relative vorticity advection (unit:  $1e-11 \text{ s}^{-2}$ ) and (b) temperature advection (unit:  $1e-5 \text{ K s}^{-1}$ ).

As depicted in Figure 2(a), there exists strong negative relative vorticity in the back of the trough and positive vorticity advection in front of the trough at 700 hPa, the latter of which is in favor of the occurrence of ascending motion. And, in front of the trough (Figure 2(b)), there is positive temperature advection, which also supports the occurrence of rising motion. For example, Li et al. [9] pointed out that the ground thermal effects of the TP can affect the strength of the India-Burma trough. The vertical motion not only reflects the relative vorticity, but also includes the influence of the temperature advection; therefore the vertical motion is used to measure the India-Burma trough.

**3.3. The India-Burma Trough Index and Its Connection with Various Meteorological Elements.** As shown in Figure 1(d), the region in front of the India-Burma trough covers  $15.625^{\circ}\text{N}-24.375^{\circ}\text{N}$  and  $90.625^{\circ}\text{E}-100.625^{\circ}\text{E}$ . For the rest of the manuscript, vertical velocity is multiplied by  $-1$ . As the India-Burma trough appears mainly in the mid-low layers of the troposphere [12], the vertical velocity in front of the trough region on a total of 5 layers from 700 hPa to 500 hPa is summed up in each year from 1979 to 2012 into a sequence, whose standardized series are used to define the index of India-Burma trough (IIBT).

$$\text{IIBT} = -\text{Norm} \left[ \prod_{700 \text{ hPa}}^{500 \text{ hPa}} \text{sum} (\omega (15.625^{\circ}-24.375^{\circ}\text{N}, 90.625^{\circ}-100.625^{\circ}\text{E})) \right], \quad (7)$$

where sum indicates sum-up,  $\prod_{700 \text{ hPa}}^{500 \text{ hPa}}$  represents sum-up from 700 hPa to 500 hPa, and Norm means normalization.

Wang et al. [23] argued that the weak India-Burma trough is one of the reasons for the most severe drought event since 1951 in southwestern China from the winter of 2009 to spring of 2010 [22, 27]. Figure 3(a) illustrates that IIBT is strongly negative for the extreme drought year of 2010. However, this drought persists to year 2012 (e.g., [28]), even though IIBT is no longer strongly negative. However, other droughts correspond well to negative IIBT values exceeding one standard deviation (e.g., 1982, 2005, 2009, and 2010 in Figure 3(a)). These illustrate that IIBT can well depict the characteristics of the India-Burma trough strength in the years with extreme climate events generally. Figure 3(b) shows multiple intersections between the UF and the UB curves before 1984, which indicates that annual variation exists for the India-Burma trough before 1984. After the year 1984, the India-Burma trough strength has an increasing tendency, and the trend becomes significant around 2000, exceeding 95% confidence level. Figure 4 demonstrates the

EOF analyses of the precipitation of 148 stations in low-latitude highlands, located in front of the India-Burma trough. The correlation coefficient between IIBT and the PCI of the 1st EOF mode of the precipitation of these 148 stations is 0.55, and the value in nearly all the spatial field of the 1st EOF mode is consistently positive or negative (Figure 4(a)). So, IIBT not only reflects annual variation characteristics of the India-Burma trough, but also reveals its interdecadal variation characteristics. IIBT also embodies the close relationship between India-Burma trough and related-area precipitation.

As shown in Figure 5(a), there is, respectively, one trough in the Arabian Sea and in the northern BOB on 700 hPa, which are called the Arabian Sea trough and the India-Burma trough. In the back of each trough, there exists one anticyclone, each being a part of the South Asia high. The Arabian Sea trough vorticity and IIBT are negatively related, while the anticyclone vorticity in the east of South Asia high is positively related to IIBT. As the Arabian Sea trough becomes weak, the downstream anticyclone in the east of the South Asia high is weak, and the IIBT increases, indicating

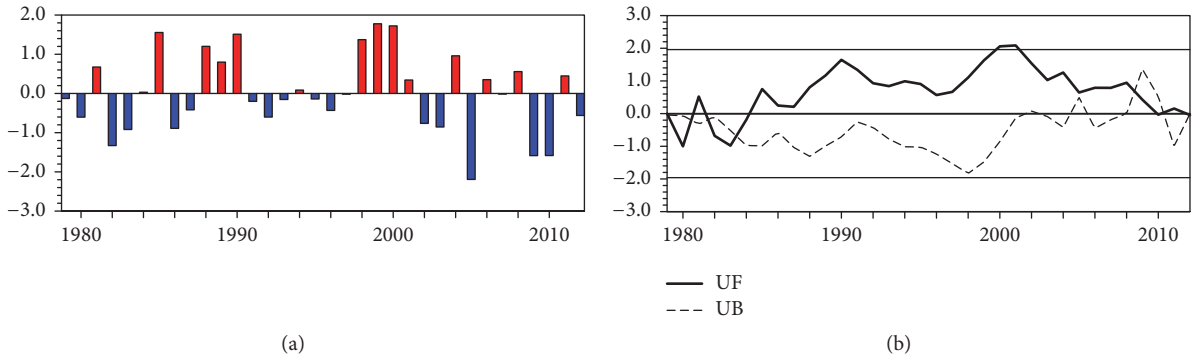


FIGURE 3: (a) Time series of IIBT and (b) M-K analysis of IIBT; straight line indicates the critical value of 95% significance  $t$ -test.

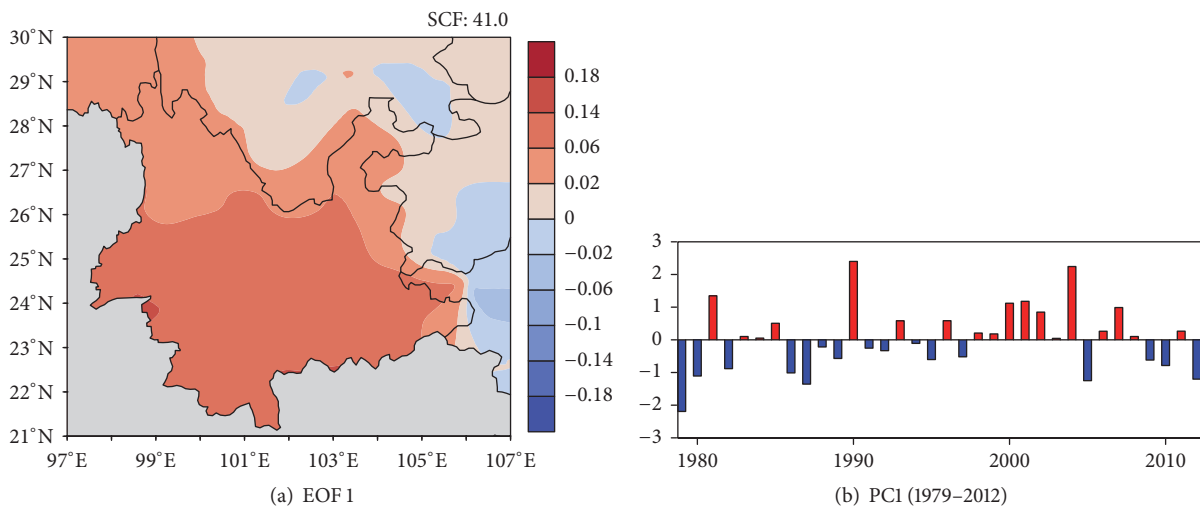


FIGURE 4: (a) The first EOF mode of observational precipitation of 148 stations in winter half year over low-latitude highlands and (b) its corresponding standardized temporal serial PCI.

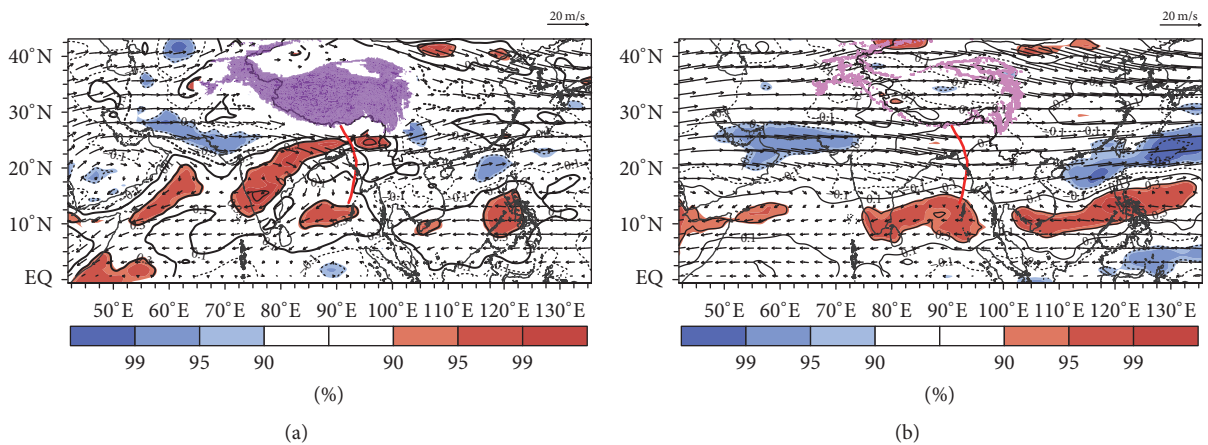


FIGURE 5: The correlation between vorticity and IIBT (contour) and the mean wind field of the winter half year (unit:  $m s^{-1}$ ). (a) For 700 hPa and (b) for 500 hPa. The different shadings from light to dark have passed the significance test with more than 90%, 95%, and 99% confidence level, respectively; the red (blue) areas denote positive (negative) correlation areas, and the area encircled by yellow line is the TP (the same for the following context).

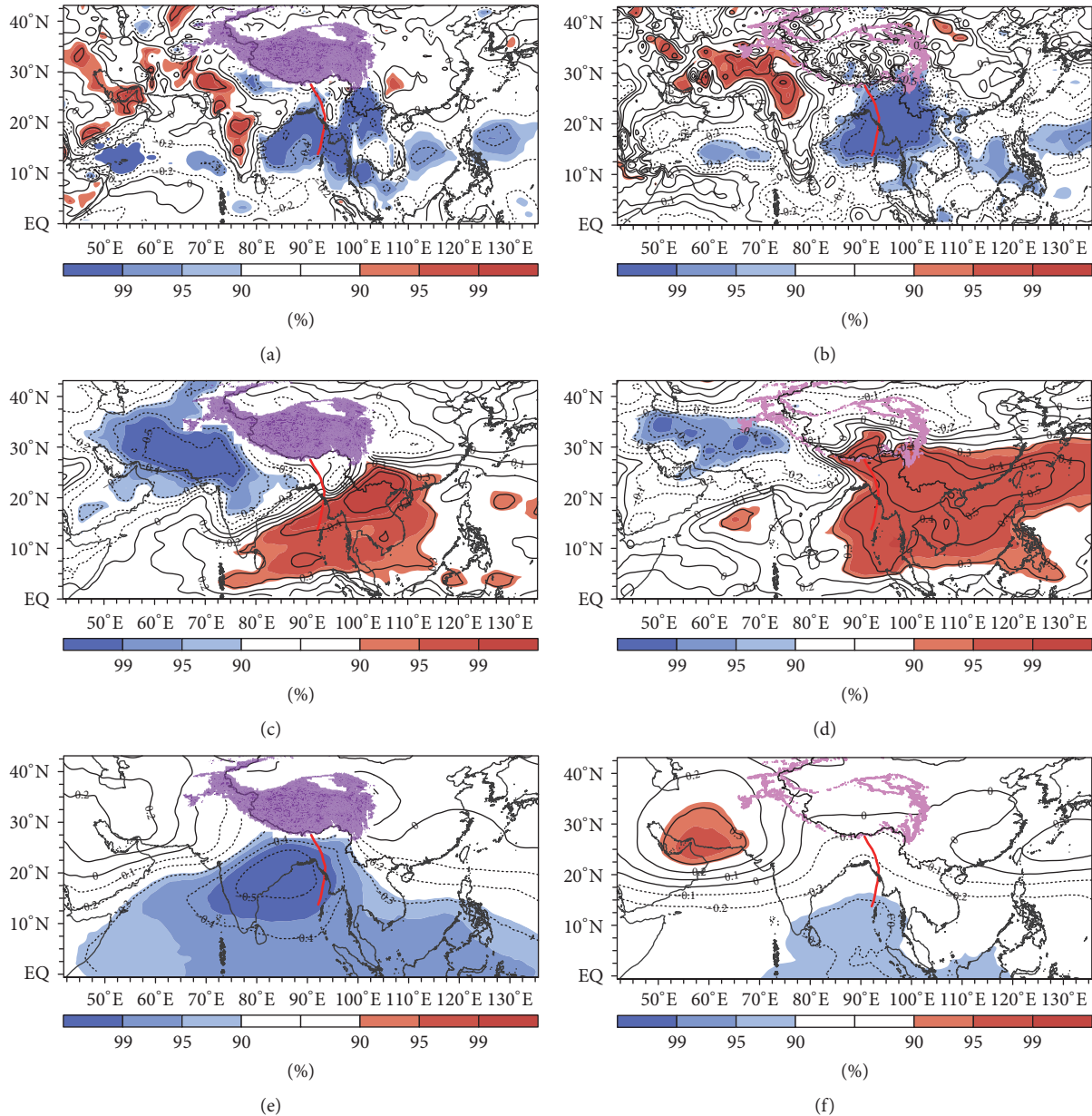


FIGURE 6: The correlation between the vertical velocity (a, b), specific humidity (c, d), geopotential height (e, f), and IIBT ((a), (c), and (e) for 700 hPa; (b), (d), and (f) for 500 hPa) in winter half year. Additionally, the different shadings from light to dark have passed the significance test with more than 90%, 95%, and 99% confidence level, respectively; the red (blue) areas denote the positive (negative) correlation areas, respectively.

that the trough becomes stronger, and vice versa. From the 500 hPa analysis (Figure 5(b)), it can also be seen that when the upstream anticyclone in the west of the South Asia high becomes strong (or the Arabian Sea trough becomes weak), the zonal air flow along the periphery of the high is more likely to turn into northerlies, and meanwhile the anticyclone in the east becomes weak and the India-Burma trough grows strong when the peripheral air flow of the subtropical high near 100°E–130°E along 10°N becomes weak. According to the method provided by Yang and Sun [29] and considering the average position of the subtropical high in the research time span, the meridional position index of the subtropical high

is calculated with the averaged relative vorticity over 500 hPa within 14°N–24°N and 110°E–135°E, whose correlation coefficient with IIBT is 0.28, indicating passing 90% significance test. This illustrates that when the India-Burma trough grows strong, the subtropical high moves eastward, which causes weak air flow along the subtropical high periphery near the India-Burma trough. IIBT reflects the relationship between the India-Burma trough activity and the upstream fluctuation of the south branch westerly and its connection with the South Asia high and the subtropical high.

As shown in Figure 6(a), it can be seen that when the India-Burma trough grows strong, at 700 hPa, the vertical

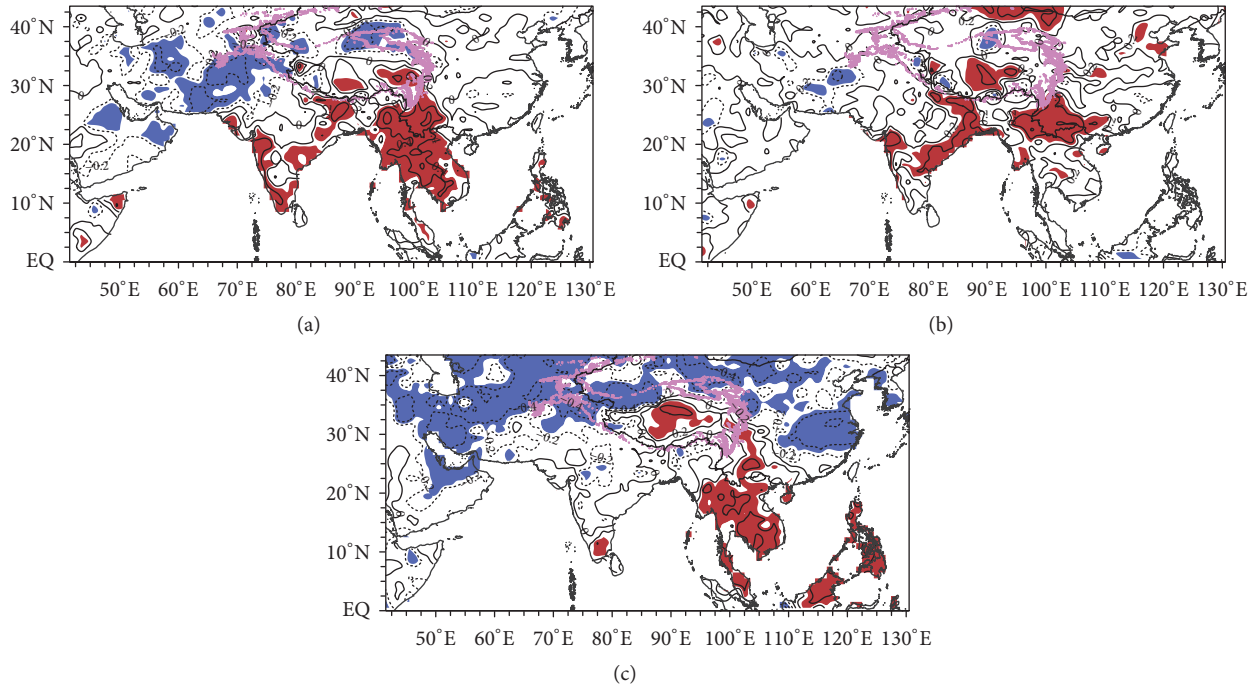


FIGURE 7: The correlation between IIBT (a), the India-Burma trough index defined with vorticity (b), the India-Burma trough index defined with geopotential height (c), and the grid point GPCP precipitation in winter half year, respectively. The shaded areas pass significance test more than 90% confidence level, where the red (blue) areas denote the areas of more (less) rainfall when the India-Burma trough is strong.

ascending motion is enhanced in the zonal circulation between 10°N and 20°N. The descending motion in the back of the Arabian Sea trough is enhanced, and the vertical motion in front of the India-Burma trough obviously becomes strong. The 500 hPa contour (Figure 6(b)) also shows the above features, but with less negative correlation area and more positive correlation area whose center moves to the Iran plateau. Li et al. [9] pointed out that as the India-Burma trough strengthens, the convective activity near the BOB becomes more vigorous, which is reflected by IIBT. In addition, from both 700 hPa and 500 hPa in Figures 6(c) and 6(d), it can be seen that as the India-Burma trough index increases the specific humidity values in front of the trough increase, with more water vapor from the tropical ocean, whereas the air flow turns drier in the Iran plateau in the India-Burma trough upstream. When the India-Burma trough grows strong, the vertical motion becomes vigorous, with the water vapor transporting upwards from the low layer, and therefore the positive correlation between the moisture in front of the trough on 500 hPa and IIBT is more significant, compared to that in 700 hPa. The India-Burma trough is closely related to the water vapor advection in front of the trough, which is also reflected by IIBT.

Additionally, Figures 6(e) and 6(f) show that when the IIBT is more intense, the geopotential height in the India-Burma trough region decreases, whereas the air flow in the back of the Arabian Sea trough accumulates, with greater geopotential height values, which is consistent with the analysis of Figures 5, 6(a), and 6(b). The variations of the vertical velocity, specific humidity, and the geopotential height are

important indices, which reflects the variations of the India-Burma trough, especially the variations of specific humidity, which is the reflection of the air flow strength in front of the trough and an important factor affecting the precipitation of the low-latitude highlands. The significant correlations between IIBT and these meteorological elements, as well as the consistency in the correlation patterns, illustrate that IIBT can reflect the India-Burma trough structure.

*3.4. The Comparison between IIBT and Other India-Burma Trough Indices.* Wang et al. [12] used averaged vorticity of the area of 15°N–25°N and 80°E–100°E at 700 hPa to define the India-Burma trough index, whose correlation coefficient with IIBT is 0.46. Suo and Ding [3] used 700 hPa anomaly series of the mean geopotential height of the area of 15°N–25°N and 80°E–100°E to define the India-Burma trough index, whose correlation coefficient with IIBT is  $-0.48$ . These 2 correlation coefficients have passed the 99% significance test with critical value of 0.44. The correlation patterns of these 3 indices with GPCP grid point precipitation are displayed in Figure 7. From the correlation pattern between IIBT and GPCP precipitation (Figure 7(a)), it is evident that when the India-Burma trough becomes strong in winter and spring, the precipitation of the southeast corner of TP, southwestern China to the eastern India-Burma trough, and the Indo-China Peninsula increases, as well as the rainfall of the areas along the coastline in the Indian subcontinent, mainly restricted to 10°N–30°N and 80°E–105°E. But the precipitation in the Iran plateau area decreases, mainly confined to 25°N–35°N and 55°E–80°E. So, the correlation field between

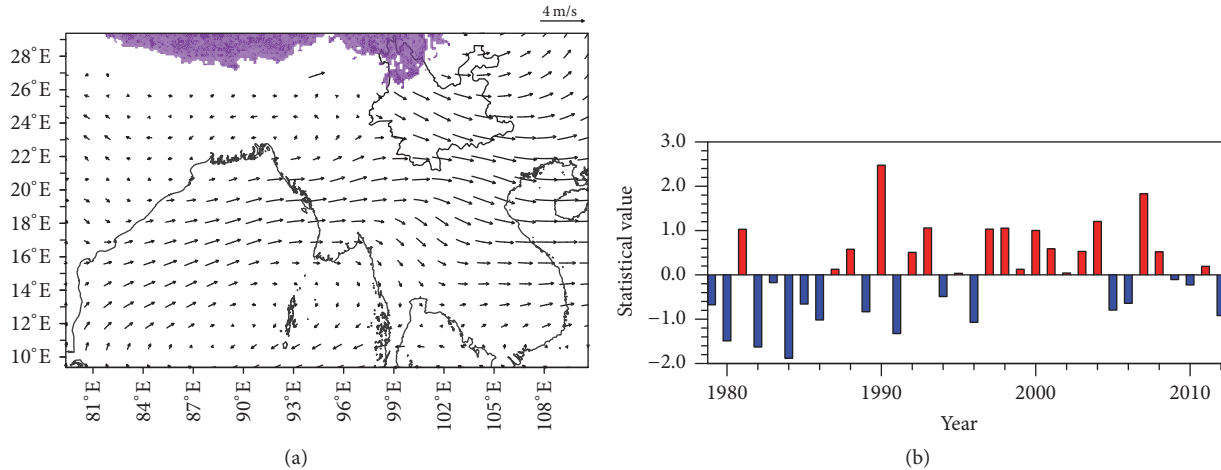


FIGURE 8: (a) In winter half year the wind field of 2010 minus the average wind field from 1979 to 2012 at 700 hPa (unit:  $\text{m s}^{-1}$ ). (b) the India-Burma trough index defined with vorticity.

IIBT and the precipitation takes on a dipolar pattern to the south of the TP. This dipole type appears in the same spatial position in Figures 6(a), 6(b), 6(c), 6(d), and 6(f), in a good agreement with each other, which indicates that IIBT well reflects the influence of the India-Burma trough strength on the meteorological elements in the low-latitude highlands in China, the southeast corner of the TP, the Indo-China peninsula, and the Indian subcontinent, as well as the impact degree of the precipitation there. Compared with Figure 7(a), the India-Burma trough index defined with vorticity reflects significantly less influence scope from the trough on the precipitation of the Indo-China peninsula and the Indian peninsula, as well as fewer areas of less precipitation in the Iran plateau. The dipole type (Figure 7(b)) similar to Figure 7(a) still exists, but very weak, which means that the index cannot reflect well the wide influence degree of the India-Burma trough on the precipitation in South Asia. The correlation between the India-Burma trough index defined with geopotential height and the grid point precipitation is shown in Figure 7(c), which can reflect the impact of the trough on the precipitation in Indo-China peninsula, but not for the rainfall in southwestern China. The water vapor transportation of the India-Burma trough is beneficial to the precipitation in South China and even serves as an important moisture source in the prerainy period. However, Figure 7(c) shows that the stronger India-Burma trough is unfavorable to the precipitation in South China. As shown in Figure 5, the Philippines and Malaysia are under the control of the subtropical high in winter and spring; possibly the subtropical high is an important factor for the amount of the rainfall there. Under the consideration of all these conditions, the India-Burma trough index defined with geopotential height seems unable to reflect the real impact degree of the trough on the surrounding areas.

Except for the Philippines and Malaysia, the areas passing the significance test in South Asia in Figure 7(a) are nearly the combination of Figures 7(b) and 7(c), IIBT can better reflect the important influence of the India-Burma trough

on the precipitation in South Asia, and the consistence of the dipole in Figures 6(a), 6(b), 6(c), 6(d), and 6(f) with Figure 7(a) reveals that IIBT can better describe the coordination between the trough and the surrounding circulation background.

#### 4. Conclusion and Discussion

The upward motion is closely associated with temperature advection and vorticity advection, which often vary with the change of the weather or climate. So, it can affect directly the related-area precipitation during the winter half year, which is an important source to local water supply for domestic water in autumn and early spring crop growth. To facilitate the understanding, the vertical velocity is multiplied by  $-1$ , and the vertical velocities in front of the trough on a total of 5 layers from 700 hPa to 500 hPa are summed up year by year spanning 1979 to 2012, which after standardization is defined as the index of India-Burma trough (IIBT).

IIBT can reflect the strength of India-Burma trough in the years with extreme climate events. As shown in Figure 8(a), in the winter and spring of 2009-2010, compared with the average state of 1979-2012, an anomalous anticyclone is excited in the India-Burma trough region, and the trough is evidently weak, which is in accordance with the situation in IIBT series (Figure 3(a)). In addition, IIBT negative anomaly years (1982, 2005, 2009, and 2010) also conform to this rule. Since the 1970s, dramatic changes occurred in many parts of the world [30, 31], with more extreme weather and climate events. The index defined by vorticity cannot reflect these events well (Figure 8(b)). Under such background, employing IIBT to describe the India-Burma trough can well characterize its annual variation.

IIBT reflects the relationship between the trough and the upstream fluctuation of the southern branch westerlies. When the anticyclone in the west of the South Asia high is enhanced, the zonal air flow along the periphery of the high is more likely to become northerlies; at the same time

the anticyclone in the east of South Asia high becomes weak, and the IIBT is more intense and the trough turns out to be stronger. And the relationship between the India-Burma trough and the upstream fluctuation is also reflected in the precipitation. When the trough grows strong, the precipitation of the Iran plateau decreases. IIBT also reveals the correlation between the trough and the surrounding weather and climate system, as well as the trough structure. When the trough grows strong, the peripheral air flows of the South Asia high and subtropical high become weak, and the sinking motion in the back of the Arabian trough is enhanced. The vertical motion in front of the India-Burma trough significantly becomes strong, and the specific humidity in front of the trough increases; meanwhile the geopotential height in the trough region decreases.

Through the correlation of IIBT and other India-Burma trough indices separately defined with vorticity and geopotential height, with the grid point precipitation, it is found that the correlation pattern of IIBT with precipitation is nearly the sum as the latter two with precipitation over South Asia. The correlation field takes on a dipole type to the south of the TP, which appears in the same spatial position of the correlation fields of IIBT with vertical velocity, specific humidity, and the mid-level geopotential height, very consistent with each other. The India-Burma trough is a major moisture source for the southwestern China in winter and spring. As shown in Figure 7, the India-Burma trough has important effects on the precipitation in southwestern China, which is also verified by the observational data from 148 stations in the low-latitude highlands (including Yunnan, the south of Sichuan, the west of Guangxi, and the west of Guizhou) in southwestern China. Spring is the most active stage of the India-Burma trough [3], and during this period the correlation field of the observational data of the meteorological station with IIBT has 106 (71.6% of the total) stations passing the 95% significance test, which reveals the influence of magnitude and degree of the trough on the spring precipitation; the correlation linked index defined with vorticity and precipitation also reflects the influence on rainfall from the trough, with 95 stations passing the 95% significance test, whereas the index defined with geopotential height fails to reach the accuracy, only with 62 stations passing the 95% significance test (figure omitted).

The correlation coefficient between IIBT and the PCI of the 1st EOF mode of the precipitation of these 148 stations is 0.55 (Figure 4). Through IIBT, the study on the specific impact of the India-Burma trough on the precipitation in South Asia is worth delving more deeply.

## Conflicts of Interest

The authors declare that there are no conflicts of interest regarding the publication of this paper.

## Acknowledgments

The monthly Modern-Era Retrospective Analysis for Research and Applications atmospheric circulation data is provided by Goddard Earth Sciences Data and Information

Sciences Center (GESDISC). The precipitation data used here is the Global Precipitation Climate Center (GPCC) monthly precipitation data (V6 and V4). The monthly precipitation data of 148 stations in low-latitude highlands is provided by the Climate Center of Yunnan Meteorological Administration. The authors acknowledge all the data sources. This study is sponsored by the National Key Research and Development Program of China Grant no. 2017YFC1404002, the National Natural Science Foundation of China (U1502233, Grant no. 41375082), and Yunnan Province Education Department Project (2017YJS106).

## References

- [1] J. C. Yang, S. Y. Tao, and T. C. Yeh, *Meteorology of the Tibetan Plateau*, China Science Press, 1960, pp. 280.
- [2] J. Qin, J. H. Ju, and M. E. Xie, "Weather and Climate in Low Latitudes Plateau," *China Meteorological Press*, p. 210, 1997 (Chinese).
- [3] M. Q. Suo and Y. H. Ding, "Structures and evolutions of the wintertime southern branch trough in the subtropical westerlies," *Journal of the Atmospheric Sciences*, vol. 33, pp. 425–442, 2009 (Chinese).
- [4] S. Y. Tao, "Influence of the India-Burma trough on the weather of southern China in winter," *Acta Meteorologica Sinica*, vol. 23, pp. 172–192, 1952 (Chinese).
- [5] T. M. Wang, G. X. Wu, and R. J. Wan, "Influences of the thermal and dynamical forcing of the Tibetan Plateau on the circulation over the Asian monsoon region," *Plateau Meteorol*, vol. 27, pp. 1–9, 2008 (Chinese).
- [6] J. H. He, C. H. Sun, Y. Y. Liu, J. Matsumoto, and W. Li, "Seasonal transition features of large-scale moisture transport in the Asian-Australian monsoon region," *Advances in Atmospheric Sciences*, vol. 24, no. 1, pp. 1–14, 2007.
- [7] X. Duan, Y. Tao, Xu. ML et al., "Influence of south branch trough of westerlies on weather of Yunnan province," *Plateau Meteorol*, vol. 31, no. 4, pp. 1059–1065, 2012 (Chinese).
- [8] T. F. Zhang, Y. B. Lu, J. Zhang et al., "Contrast analysis of 4 heavy snow events in Yunnan since," *Journal of Meteorological Science*, vol. 18, pp. 64–72, 2000.
- [9] D. L. Li, V. He, X. Tang, and Y. Hou, "Relationship between the intensity of surface heating over the Qinghai-Xizang Plateau and ENSO cycle," *Plateau Meteorol*, vol. 26, pp. 39–46, 2007 (Chinese).
- [10] H. Y. Zhao, X. H. Chen, X. W. Wan et al., "Climatic analysis and forecasting method of sand-dust storms in Northwest China," *Journal of Desert Research*, vol. 24, pp. 637–641, 2004 (Chinese).
- [11] Y. L. Zhang, G. Z. Fan, D. W. Zhou et al., "The climate characteristics analysis of the wintertime Southern Branch Trough," *Journal of Chengdu University of Information Technology*, vol. 27, no. 2, pp. 196–201, 2012 (Chinese).
- [12] T. Wang, S. Yang, Z. P. Wen, R. Wu, and P. Zhao, "Variations of the winter India-Burma Trough and their links to climate anomalies over southern and eastern Asia," *Journal of Geophysical Research: Atmospheres*, vol. 116, no. D23, pp. n/a–n/a, 2011.
- [13] B. Lu and H.-L. Ren, "SST-forced interdecadal deepening of the winter India-Burma trough since the 1950s," *Journal of Geophysical Research: Atmospheres*, vol. 121, no. 6, pp. 2719–2731, 2016.
- [14] J. Cao, P. Yao, L. Wang, and K. Liu, "Summer rainfall variability in low-latitude highlands of China and subtropical Indian

- Ocean dipole,” *Journal of Climate*, vol. 27, no. 2, pp. 880–892, 2014.
- [15] D. Barriopedro, C. M. Gouveia, R. M. Trigo, and L. Wang, “The 2009/10 drought in China: Possible causes and impacts on vegetation,” *Journal of Hydrometeorology*, vol. 13, no. 4, pp. 1251–1267, 2012.
- [16] J. Yang, D. Y. Gong, W. S. Wang, M. Hu, and R. Mao, “Extreme drought event of 2009/2010 over southwestern China,” *Meteorology and Atmospheric Physics*, vol. 115, no. 3-4, pp. 173–184, 2012.
- [17] W. J. Zhang, F. F. Jin, J. X. Zhao, L. Qi, and H. L. Ren, “The possible influence of a nonconventional El Niño on the severe autumn drought of 2009 in Southwest China,” *Journal of Climate*, vol. 26, no. 21, pp. 8392–8405, 2013.
- [18] L. Wang and W. Chen, “A CMIP5 multimodel projection of future temperature, precipitation, and climatological drought in China,” *International Journal of Climatology*, vol. 34, no. 6, pp. 2059–2078, 2014.
- [19] Y. Yin, D. Ma, S. Wu, and T. Pan, “Projections of aridity and its regional variability over China in the mid-21st century,” *International Journal of Climatology*, vol. 35, no. 14, pp. 4387–4398, 2015.
- [20] J. Q. Zhai, J. L. Huang, B. D. Su et al., “Intensity–area–duration analysis of droughts in China 1960–2013,” *Climate Dynamics*, vol. 48, no. 1-2, pp. 151–168, 2017.
- [21] C. Hao, J. Zhang, and F. Yao, “Multivariate drought frequency estimation using copula method in Southwest China,” *Theoretical and Applied Climatology*, vol. 127, no. 3-4, pp. 977–991, 2017.
- [22] J. M. Lü, J. H. Ju, J. Z. Ren, and W. W. Gan, “The influence of the Madden-Julian Oscillation activity anomalies on Yunnan’s extreme drought of 2009-2010,” *Science China Earth Sciences*, vol. 55, no. 1, pp. 98–112, 2012 (Chinese).
- [23] X. M. Wang, S. W. Zhou, and B. Zhou, “Causative analysis of continuous drought in southwest China from Autumn 2009 to Spring 2010,” *Meteorological Monthly*, vol. 38, no. 11, pp. 1399–1407, 2012.
- [24] X. Z. Liu and W. Zhou, “Modulation of the interannual variation of the India-Burma Trough on the winter moisture supply over Southwest China,” *Climate Dynamics*, vol. 46, no. 1-2, pp. 147–158, 2016.
- [25] X. Li, Y. Q. D. Chen, and W. Zhou, “Response of winter moisture circulation to the India-Burma trough and its modulation by the South Asian waveguide,” *Journal of Climate*, vol. 30, no. 4, pp. 1197–1210, 2017.
- [26] F. Y. Wei, *Modern climatic statistical diagnosis and prediction technology*, China Meteorological Press, 2nd edition, 2007, pp. 63–70.
- [27] C. Sun and S. Yang, “Persistent severe drought in southern China during winter-spring 2011: large-scale circulation patterns and possible impacting factors,” *Journal of Geophysical Research: Atmospheres*, vol. 117, no. 10, pp. 63–74, 2012.
- [28] NCC/CMA, “China Climate Impact Assessment. National climate center/China Meteorological Administration Rep 4 :19pp, 2012”.
- [29] H. Yang and S. Q. Sun, “The characteristics of longitudinal movement of the subtropical high in the western Pacific in the pre-rainy season in South China,” *Advances in Atmospheric Sciences*, vol. 22, no. 3, pp. 392–400, 2005.
- [30] K. E. Trenberth and J. W. Hurrell, “Decadal atmosphere-ocean variations in the Pacific,” *Climate Dynamics*, vol. 9, no. 6, pp. 303–319, 1994.
- [31] Intergovernmental Panel on Climate Change, *Summary for Policymakers of the Synthesis Report of the IPCC Fourth Assessment Report*, Cambridge University Press, UK, 2007.

## Research Article

# Evaluating Linkages between Atmospheric Blocking Patterns and Heavy Rainfall Events across the North-Central Mississippi River Valley for Different ENSO Phases

Jordan L. Rabinowitz <sup>1</sup>, Anthony R. Lupo,<sup>1,2</sup> and Patrick E. Guinan<sup>3</sup>

<sup>1</sup>Atmospheric Sciences Program, School of Natural Resources, University of Missouri, Columbia, MO, USA

<sup>2</sup>Department of Natural Resources Management and Land Cadastre, Belgorod State University, Belgorod 308015, Russia

<sup>3</sup>Missouri Climate Center, College of Agriculture, Food, and Natural Resources, University of Missouri, Columbia, MO 65211, USA

Correspondence should be addressed to Jordan L. Rabinowitz; [jlrxw6@mail.missouri.edu](mailto:jlrxw6@mail.missouri.edu)

Received 29 August 2017; Accepted 15 January 2018; Published 11 March 2018

Academic Editor: Tomeu Rigo

Copyright © 2018 Jordan L. Rabinowitz et al. This is an open access article distributed under the Creative Commons Attribution License, which permits unrestricted use, distribution, and reproduction in any medium, provided the original work is properly cited.

Over the last six to seven decades, there has been a substantial increase in atmospheric research to better understand the dynamics and evolution of atmospheric blocking events. It is well known that atmospheric blocking serves as a catalyst for increasing the frequency of atmospheric flow regime stagnation and forecast unpredictability. This study built upon the results of previous work by expanding upon the findings of various climatologies and case studies. This work analyzes specific trends observed in association with atmospheric blocking predominantly across the central and eastern Pacific Ocean. Such trends include the relationship between the size, duration, and onset position of atmospheric blocking events and the frequency, duration, and intensity of heavy rainfall events across the central United States. A strong focus is placed on examining the duration and spatial extent of atmospheric blocking which has been found to influence the intensity of heavy rainfall events. The goal is to further bridge the gap between the location and duration of blocking highs and the intensity, duration, and frequency of heavy rainfall events which occur downstream of such blocking events.

## 1. Introduction

Since the onset of the remote sensing era, there have been many advances in the analysis and forecasting of atmospheric blocking which is known to have a noticeable influence on the occurrence frequency and evolution of high-impact weather events such as cold waves [1] or the Russian heat wave of 2010 [2–4]. Over the past five to six decades, much research has been conducted in order to gain an understanding of the dynamics that contribute evolution of atmospheric blocking events. The work of [5] began this research by working to understand the climatological behavior of blocking and speculated that atmospheric blocking events and their dynamics may be likened to a mechanical analogue. Then researchers such as [6, 7] further elaborated upon the work of Rex (1950) through elaborating upon how atmospheric blocking events are generated through the interaction of transient, synoptic-scale perturbations with the planetary-scale environment.

In this context, blocking may be understood as resonance between the planetary waves to synoptic-scale perturbations (e.g., [7]) which act as sources of energy and vorticity. These studies and others showed that the nature of a given atmospheric blocking response may often depend on the location of the synoptic-scale perturbation relative to the planetary waves.

Studies of flow regime dynamics such as [8–11] found evidence for multiple persistent flow regimes in the Northern Hemisphere flow including regimes that represent blocking flows [8]. These studies describe only the mean structure of blocking, and others (e.g., [12]) described blocking as a soliton. Such studies, however, could not describe the evolution of blocking. Then [13] constructed a soliton model that described the evolution of blocking as a scale-interaction problem as described above. Further, [14, 15] used an analytic channel-type model to explore the phase transitions of a



FIGURE 1: A map of the study region. The approximate region is outlined with the thick line.

North Atlantic Oscillation- (NAO-) like pattern. They impose a low-frequency planetary-scale wave with a period of about two to three weeks on a zonal flow as well as a synoptic-scale perturbation of about three days in length to describe the transitions between the positive and negative phases of the NAO and the presence and role of blocking in these transitions. The model was extended by [16] to demonstrate the interactions among the mean flow, planetary waves, and synoptic eddies and proposed a new mechanism to explain the onset or destruction of blocking regimes.

In addition to studies that examined the synoptic and dynamic behavior of atmospheric blocking, investigators have related blocking to the weather and climate of regions within and adjacent to these events. For example, [13] built a relationship between large-scale temperature regimes across entire oceanic basins, the prevalence of atmospheric blocking events just to the south of Alaska, and the downstream impacts of such blocking events on precipitation frequency and intensity across the central and eastern United States. A few studies have examined the relationship of blocking to the seasonal character of weather, such as temperature and precipitation amounts, across the central United States [14–16].

This work more closely investigates how different pre-blocking factors affect the spatial extent and intensity of heavy rainfall events across the region of concern. For this work, the study region is the North-Central Mississippi River Valley (Figure 1) and the period examined was between 1 January 2000 to 31 December 2015. This work is unique in that it will examine the character and impact of individual heavy rainfall events across the North-Central Mississippi River Valley and relate these to the climatological character of blocking (e.g., frequency, duration, and intensity) in the Pacific Ocean Basin. This study will also examine the linkage between interannual variability as related to El Nino and Southern Oscillation (ENSO) for heavy rainfall and blocking. Previous studies of heavy snowfall and the connection to large-scale flow regimes and well as interannual variability have been done for this region [18]. Lastly, the onset and occurrence of atmospheric blocking continue to present major forecasting problems [3].

The predominant issue has been the ability (or lack thereof) of operational forecasters to accurately anticipate the onset and decay of atmospheric blocking events [3]. Through garnering an improved understanding of the link between atmospheric blocking and heavy rainfall events in our region, the atmospheric research community will be able to generate a more efficient “roadmap” for improving the anticipation of heavy rain events.

## 2. Data and Methodology

**2.1. Data.** The data used in this analysis for blocking are archived at the University of Missouri and may be accessed online [20]. The data integrated into this study from this blocking archive included the following parameters: block intensity (BI), block duration (BD), block size (BS), blocking onset lead-time (BOLT), and longitude at block onset (LABO). Other indexes that describe blocking character such as those derived by [21, 22] could be used here. However, the dataset used here was readily available and has been used in many studies by this research group. A comparison of these indexes is beyond the scope of this study.

The block intensity (BI) parameter was developed and later modified for automated use by [17]. Briefly, BI normalizes the central height value of a block (MZ) by the gradient of the height field surrounding the event (RC) [17] and averaged over the block lifetime. The calculation of BI was represented by the following equation:

$$BI = 100 * \left( \left( \frac{MZ}{RC} \right) - 1 \right). \quad (1)$$

Additionally, recent study [23] demonstrated that BI can be related to dynamic quantities such as enstrophy and entropy and thus related to flow regime stability and predictability.

The block duration (BD) parameter was included via the criteria first established by [5, 22] and modified, whereby a blocking event is verifiable only if a blocking high pressure persists for a minimum of five days as evaluated by flow at the 500 mb level. The intent behind evaluating BD is to study observed differences between the respective ENSO phases and the persistence of the blocking events formed between 2000 and 2014. This BD analysis is an extension of previous work (e.g., [17]). The block size (BS) parameter was included based on a framework wherein they designated the BS value as the half-wavelength distance (measured in units of km). The BS parameter was included to assess if a relationship existed between BS and event rainfall duration. The analysis related to the BS parameter expands on pertinent results from previous work [13].

The blocking onset lead-time (BOLT) parameter is a newly coined parameter used to distinguish blocking events which had an association between block onset and the occurrence of heavy rain. The definition for the BOLT parameter is such that only blocking events existing for at least two days prior to the day of a heavy rainfall event are considered. Another important parameter was the “longitude at block onset” (LABO) parameter which was used to assess possible relationships between the location of blocking events (i.e., the longitudinal position within the Pacific Ocean where

TABLE 1: List of ENSO years 2000–2015: see [19] for definition; ENSO year begins 1 October of the given year.

El Nino	Neutral	La Nina
2002	2000-2001	1999
2006	2003-2005	2007
2009	2008	2010
2014-2015	2011-2013	

blocking events were centered) and the duration/intensity of rainfall events. For the LABO parameter, the Pacific Ocean was divided into four regions to differentiate between the various blocking events. These four regions were designated as the eastern Pacific Ocean (between 120°W and 140°W), the east central Pacific Ocean (which between 140°W and 180°W), the west central Pacific Ocean (between 160°E and 180°E), and the western Pacific Ocean (between 140°E and 160°E).

Finally, each heavy rainfall event that occurred concurrently with a Pacific Ocean blocking event is referenced throughout the following text as an event during a given ENSO phase whether they occurred with the same blocking event or not. Also, the distribution of the respective ENSO phases is shown in Table 1, and ENSO is defined using the Japanese Meteorological Agency (JMA) criterion [19]. This definition has been used by many studies of interannual variability in the broader region (e.g., [15] and references therein) and will facilitate comparing these results with those studies. Furthermore, any heavy rainfall event which was considered to be admissible for this study had to be a minimum 24-hour rainfall threshold of 50.8 mm (2.00 inches) or more at the Saint Louis Weather Service Forecast Office (STL WFO). This definition is consistent with that used by [24].

### 3. Characteristics of Atmospheric Blocking: Implications for Downstream Flow Regimes

*3.1. Overall Climatology: Heavy Rain Events Associated with Blocking.* All 16 events are listed in Table 2. Of these, nine are summer season events, three events occurred during both the winter and spring, and only one was a fall season event. There was no statistically significant relationship between BI, BD, BS, or any of these variables and rainfall amounts. This is likely due to the small sample size since there was a statistically significant relationship between the respective variables and rainfall amounts. Additionally, while [9, 17] found that there were more winter season blocking events than summer season events within the Pacific Ocean Basin, it was the summer season, which resulted in more blocking events associated with heavy rain since the summer season is the associated with the largest number of heavy rain events. Also, winter season events were generally stronger, while summer events were comparatively weak within the region as found by [17].

An analysis of the synoptic maps demonstrated that the heavy rain events were associated with synoptic-scale

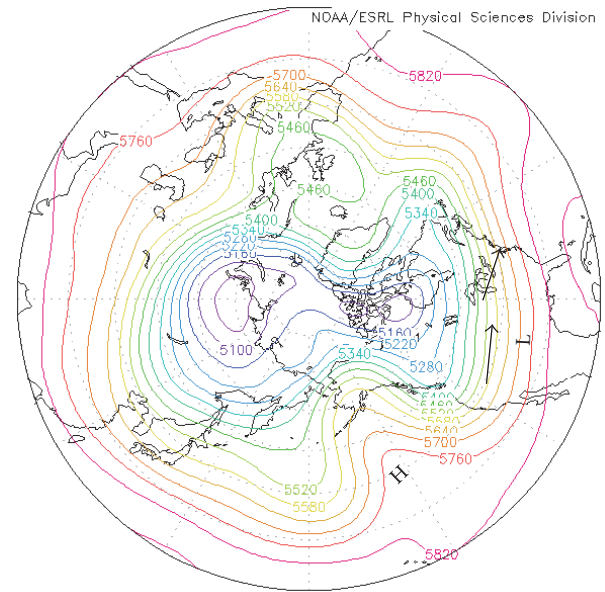


FIGURE 2: The Northern Hemisphere 500 hPa heights (m) for 16–24 November 2010 contoured every 60 m. The location of the block is noted with an H and the location of the surface feature associated with the heavy rain event of 24 November 2010 is marked with L. The black arrows represent the 300 hPa jet maximum for 24 November 2010.

transients, and the jet stream was strong over the central United States (not shown). Figure 2 shows an example for the 24 November 2010 heavy rain event (Event #15 in Table 2). There was no preference for the surface feature to be located west or east of the region, or the attendant surface fronts to be warm, cold, or a stationary front.

*3.2. ENSO Related Interannual Variability.* There were five El Nino events which occurred during the study period, and only two of these El Nino years were associated with four heavy rain events associated with a blocking event (Table 2). Each of these events was summer season events, and these events were stronger and more persistent than the typical summer season event. The mean BI was 2.39 and the standard deviation was 0.95. The mean for these four events was slightly stronger than the typical summer season Pacific Region blocking events found by [17] (BI = 2.11). The BD for these events was 13 days, the BS was 2078 km (standard deviation = 340 km), and the BOLT was 6 days. The onset location for each of these blocking events associated with heavy rain; three of these events were positioned across the east Pacific Ocean (i.e., with a blocking onset longitude of 150°W (two locking events) and 130°W). The last remaining El Nino event was located in the west Pacific Ocean (i.e., with a blocking onset longitude of 130°E).

There were only three La Nina events, which occurred between the years 2000–2015, and all three years were associated with at least two blocking events that featured heavy rain in our region (Table 2, seven total). These seven heavy rain events were found among all seasons of the year. The mean

TABLE 2: Breakdown of analyzed heavy rain events associated with atmospheric blocking included blocking parameters are the block intensity [17], block duration, and block size. The event number, date (dd mm yy), season (W, Sp, Su, and F), and ENSO phase are shown in column one (E is El Nino, L is La Nina, and N is Neutral).

Event number	Intensity	Duration	Size	Onset location
(1) 18 02 00 L W	4.22	12	1712	150°W
(2) 24 06 00 L Su	1.47	14	2658	175°E
(3) 12 05 02 N Sp	2.45	9	1470	130°W
(4) 06 08 02 N Su	2.43	8	2614	160°W
(5) 10 06 03 E Su	3.2	18.5	1812	150°W
(6) 12 06 03 E Su	3.2	18.5	1812	150°W
(7) 26 06 03 E Su	3.2	11	2151	130°W
(8) 04 01 04 N W	4.51	9.5	2658	150°W
(9) 30 07 04 N Su	1.49	5	2983	140°E
(10) 11 06 05 N Su	1.77	9.5	3765	140°E
(11) 19 07 07 E Su	1.75	7.5	2166	130°E
(12) 05 02 08 L W	2.68	10.5	1538	170°E
(13) 18 03 08 L Sp	3.68	13	1189	170°E
(14) 26 05 08 L Sp	2.78	14.5	1908	150°W
(15) 24 11 10 L F	4.14	8	2827	180°
(16) 25 06 11 L Su	1.99	11.5	3003	140°E

BI was 2.99 and an associated standard deviation of 1.06, and these values were very close to the 30-year climatological values for each quantity [17], and the individual events were above their respective Pacific Region seasonal mean as often as they were below the season mean. The mean BD was 12 days and the mean BS was 2119 km (standard deviation = 705 km), while the BOLT was 6.5 days. Among the seven La Nina heavy rain event that occurred concurrently with a Pacific blocking event, four of the events occurred with blocking events positioned across the west central Pacific Ocean, and one more over the west Pacific. Of the two remaining La Nina events occurred with blocking events positioned across the eastern Pacific Ocean. The greater number of La Nina year blocking found to be associated with heavy rain agrees with [17] and references therein, who found that in the Pacific Region blocking was more frequent and stronger.

Lastly, there were nine Neutral years during the study period, but only three of these years were associated with heavy rain events that featured a Pacific Region blocking event. There were five of these heavy rain events in total, occurring over most seasons. Among those five events, the mean BI was 2.53 and the standard deviation was 1.18. The mean BD was only eight days and the BS was 2698 km (standard deviation = 805 km), while the BOLT was only 4 days. Among the five Neutral year heavy rain events that occurred in association with a Pacific blocking event, two of the five events occurred with a blocking event positioned across the eastern Pacific Ocean, and one was located over the east central Pacific Ocean Basin. Only two of the five Neutral year events occurred with blocking events positioned across the west Pacific Ocean.

**3.3. Discussion.** When examining the block intensity, it was clear that only the El Nino year blocking events were stronger than their respective sample when compared to a similar

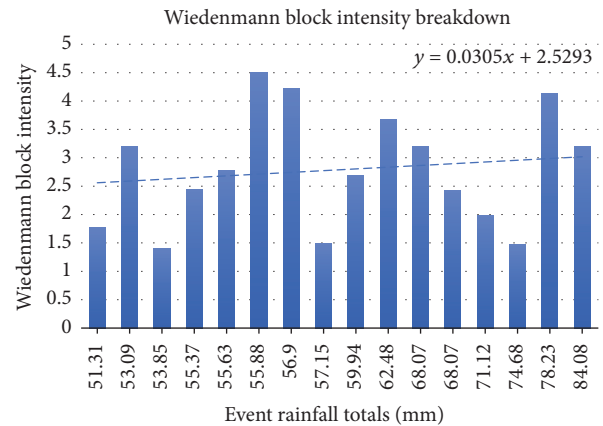


FIGURE 3: Bar plot of the block intensity [17] for all 16 analyzed blocking events with event rainfall totals (measured in millimeters) and block intensity.

seasonal and regional sample from [17]. The Neutral season events were the weakest and of the shortest duration and had the lowest BOLT parameter. Examining the correlation coefficient between BI and event rainfall total indicated there was only a slight positive relation ( $CC = 0.11$ ), but not statistically supported at standard levels of confidence (Figure 3). The events in Figure 3 were reordered for the purpose of organizing the event rainfall totals from lowest-to-highest in order to demonstrate the relationship. Additionally, the average heavy rainfall event totals from highest to lowest were 65.53 mm (La Nina events), 64.77 mm (El Nino events), and 57.56 mm (Neutral-ENSO events). This relationship between heavy rain totals and BI did not mirror precisely the decreasing order of BI for the respective ENSO phases. This reflects the variability among the BI values (e.g.,

[25]). However, a closer inspection of BI values versus the heavy rainfall event totals indicated a possible relationship since the Neutral year BI values were weakest when compared to the relevant sample from [17], and the higher standard deviation likely reflects the small sample size and the fact these occurred in all seasons. One heavy rain-blocking event was identified as an anomaly (4 January 2004 event) which was the strongest event in the study (i.e., a BI value of 4.52 compared to the Neutral-ENSO blocking event BI average of 2.53). However, this event was a winter season event.

Through evaluating the statistical results above, it is evident that block intensity may not be a reliable parameter for use in medium-range forecasting. The fact that a smaller BI value during Neutral years correlated with smaller heavy rainfall totals indicated that there may be a connection between these variables as found for seasonal precipitation and blocking [14, 15]. In order to ascertain whether there is a correlation between block intensities, it is imperative to study many more events in this (and other regions to further expand these findings) for this parameter to be more valuable in operational forecasting.

When examining the BD parameter, the duration of El Nino and La Nina year blocking events associated with heavy rain persisted longer than their climatological counterparts, while the Neutral year blocking events persistence of eight days is similar to Pacific Region block persistence [17] (Table 2). The BS parameter demonstrated that the Neutral year events were larger than the La Nina and El Nino year events, which were of similar size. Thus, the lack of a relationship here is not surprising. Also, recall that the lowest mean value for heavy rainfall events was associated with Neutral year events. However, this inverse relationship is not statistically significant.

During Neutral years, the lowest average event rainfall totals correlating with the lowest BD values was surprising since three of the five events had a tropical origin. Since tropical cyclones (TCs) are often steered by large-scale deep-layer atmospheric flow, TCs are sensitive to upstream blocking events ([13, 26, 27]). TCs positioned near blocking events are often affected in terms of both trajectory and the water vapor transport by TCs towards the US mainland [28].

The BOLT parameter was developed here and is similar to the findings of [29], and the mean BOLT values for all cases were about 5.5 days. The results for this parameter mirrored those of BD outcome in that El Nino and La Nina had the longest BD and BOLT and were associated with heavier rainfall events, while the Neutral year events had the shortest values and the lowest associated precipitation. In order to study the BOLT parameter from a different angle, a column plot was generated with the increasing event rainfall totals plotted on the abscissa and the BOLT values on the ordinate (Figure 4). Among the sixteen heavy rainfall events that occurred concurrently with Pacific blocking events, there was no seasonal preference for the occurrence of larger versus smaller BOLT values.

When examining the LABO, it is important to note that, during La Nina years, there was a stronger preference for blocking events associated with heavy rain occurring west of the International Dateline (180°). For El Nino years the

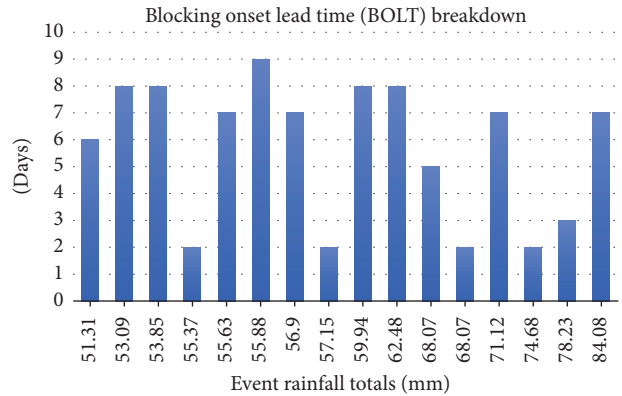


FIGURE 4: Bar plot of block onset lead times for all 16 analyzed blocking events with event rainfall totals (measured in millimeters) and number of days.

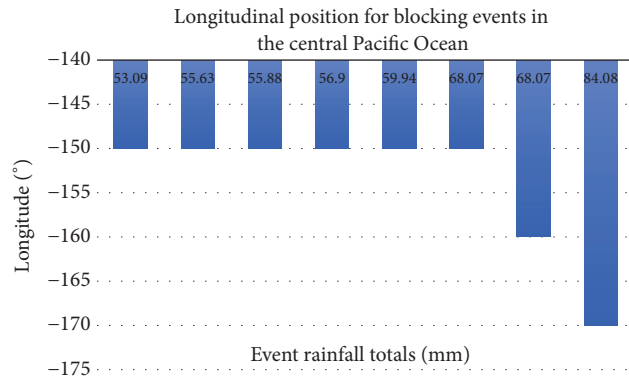


FIGURE 5: Bar plot of blocking events across the central Pacific Ocean with event rainfall totals (measured in millimeters) and longitudinal position (° west or east).

opposite was true, and for ENSO Neutral years, there was no preference (Figures 5–7). Supplemental analysis of those blocking events which developed across the central Pacific Ocean (via a clustered column plot) illustrated an increasing trend in event rainfall totals as the position of the blocking events moved from east to west across the central Pacific Ocean (Figure 5). A plausible explanation is that, by going further west across the central Pacific Ocean, there was a larger fetch over which warm, moist tropical air could accumulate before being transported downstream ([21, 30, 31]) or from the Gulf of Mexico via the atmospheric rivers (“Maya Express”) [32].

#### 4. Summary and Conclusions

In this study, sixteen heavy rainfall events that were associated Pacific Region blocking were studied here during the period 2000–2015. The Pacific Region blocking data were provided by the archive at the University of Missouri, which contains the character of all Northern Hemisphere blocking events, which have occurred since 1 January 2000. The rainfall data for this study were provided by the STL WFO, and the study region was the North-Central Mississippi River Basin.

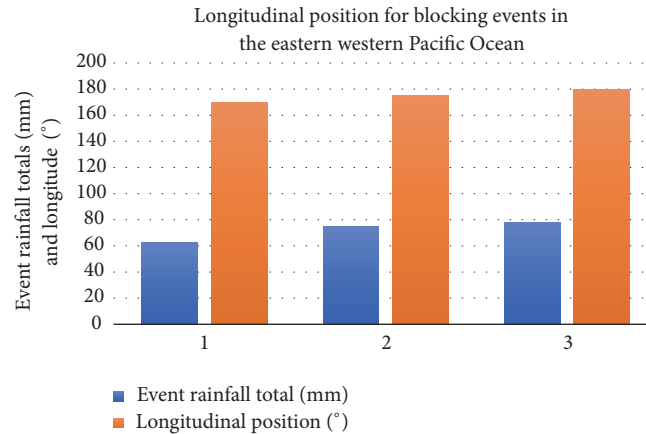


FIGURE 6: Bar plot of blocking events across the eastern-portion of the western Pacific Ocean with event rainfall totals (measured in millimeters and denoted by the blue bars) and longitudinal position ( $^{\circ}$  west or east and denoted by the orange bars).

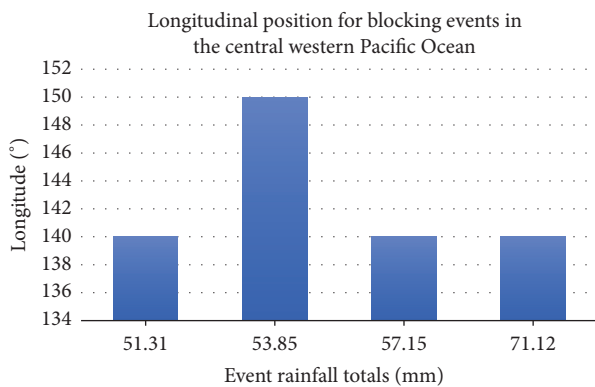


FIGURE 7: Bar plot of analyzed blocking events across the central-portion of the western Pacific Ocean with event rainfall totals (measured in millimeters) and longitudinal position ( $^{\circ}$  west or east).

Among the various blocking parameters evaluated in this study, there were several pertinent findings that emerged. All La Nina years were associated with two or more blocking events that were accompanied by heavy rainfall. This is significant since [17] showed that only seven blocking events per year occurred within the Pacific Ocean Basin. Such occurrences were comparatively rare during El Nino or Neutral years; however, some of these years were associated with multiple occurrences. Many researchers showed that the Pacific Ocean Basin was more active in terms of blocking activity [24] and references therein during La Nina years, and this is associated with a more active storm track (e.g., [16, 17]). Thus, the greater number of blocking events associated with heavy rain in the central USA is consistent with the idea that there are more opportunities for simultaneous occurrence of each.

Although there was a low positive correlation that was not statistically significant, there was a tendency for larger BI values to be correlated with heavier rainfall event totals. However, only El Nino year blocking events (associated with heavy precipitation) were stronger than their comparative

sample. Also, La Nina and El Nino years tended to be associated with longer-lived events and a longer period between block onset and the heavy rain (BOLT). Another major finding was found in association with the longitude at block onset (LABO) parameter. Throughout the LABO parameter data, there was a consistent trend defined by blocking events forming further west in the Pacific Ocean being correlated with heavier rainfall totals. It is hypothesized that with the further westward positioning of blocking high pressure systems, this favored stronger transport of warm, moist air into the region of concern (i.e., chiefly via “Maya Express” atmospheric rivers emanating from the Gulf of Mexico and/or western/central Caribbean).

Finally, the results indicated that there is still much work to be done to better understand blocking dynamics and the connection to heavy rainfalls in the central USA. Additionally, a longer study period might provide more insight into the mechanisms responsible for these connections and provide guidance for forecasters in this region.

## Conflicts of Interest

There were no conflicts of interest tied to this paper whatsoever in any capacity.

## Acknowledgments

This work was partially funded by USDA Grant, “Rainfall Rates in North-Central Missouri’s LTAR.”

## References

- [1] J. Sillmann, C.-M. Mischa, M. Kallache, and R. W. Katz, “Extreme cold winter temperatures in Europe under the influence of North Atlantic atmospheric blocking,” *Journal of Climate*, vol. 24, no. 22, pp. 5899–5913, 2011.
- [2] R. Dole, M. Hoerling, J. Perlwitz et al., “Was there a basis for anticipating the 2010 Russian heat wave?” *Geophysical Research Letters*, vol. 38, no. 6, Article ID L06702, 2011.

- [3] M. Matsueda, "Predictability of Euro-Russian blocking in summer of 2010," *Geophysical Research Letters*, vol. 38, no. 6, Article ID L06801, 2011.
- [4] I. I. Mokhov, "Specific features of the 2010 summer heat formation in the European territory of Russia in the context of general climate changes and climate anomalies," *Izvestiya - Atmospheric and Ocean Physics*, vol. 47, no. 6, pp. 653–660, 2011.
- [5] D. F. Rex, "Blocking action in the middle troposphere and its effect upon regional climate," *Tellus*, vol. 2, no. 4, pp. 275–301, 1950.
- [6] S. J. Colucci, "Explosive cyclogenesis and large-scale circulation changes: implications for atmospheric blocking," *Journal of the Atmospheric Sciences*, vol. 42, no. 24, pp. 2701–2717, 1985.
- [7] J. P. Burkhardt and A. R. Lupo, "The planetary- and synoptic-scale interactions in a southeast Pacific blocking episode using PV diagnostics," *Journal of the Atmospheric Sciences*, vol. 62, no. 6, pp. 1901–1916, 1985.
- [8] J. G. Charney and J. G. Devore, "Multiple flow equilibria in the atmosphere and blocking," *Journal of the Atmospheric Sciences*, vol. 36, no. 7, pp. 1205–1216, 1979.
- [9] K. Mo and M. Ghil, "Cluster analysis of multiple planetary flow regimes," *Journal of Geophysical Research: Atmospheres*, vol. 93, pp. 10927–10952, 1988.
- [10] F. Molteni, S. Tibaldi, and T. N. Palmer, "Regimes in the wintertime circulation over northern extratropics. I: Observational evidence," *Quarterly Journal of the Royal Meteorological Society*, vol. 116, no. 491, pp. 31–67, 1990.
- [11] P. Smyth, K. Ide, and M. Ghil, "Multiple regimes in northern hemisphere height fields via mixture model clustering," *Journal of the Atmospheric Sciences*, vol. 56, no. 21, pp. 3704–3723, 1999.
- [12] J. C. McWilliams, "An application of equivalent modons to atmospheric blocking," *Dynamics of Atmospheres and Oceans*, vol. 5, no. 1, pp. 43–66, 1980.
- [13] M. L. Carrera, R. W. Higgins, and V. E. Kousky, "Downstream weather impacts associated with atmospheric blocking over the Northeast Pacific," *Journal of Climate*, vol. 17, no. 24, pp. 4823–4839, 2004.
- [14] A. R. Lupo, E. P. Kelsey, D. K. Weitlich, N. A. Davis, and P. S. Market, "Using the monthly classification of global SSTs and 500 hPa height anomalies to predict temperature and precipitation regimes one to two seasons in advance for the mid-Mississippi region," *National Weather Digest*, vol. 32, no. 1, pp. 11–33, 2008.
- [15] R. G. Newberry, A. R. Lupo, A. D. Jensen, and R. A. Zalipynis, "An analysis of the spring-to-summer transition in the west central plains for application to long range forecasting," *Atmospheric and Climate Sciences*, vol. 6, no. 3, pp. 375–393, 2016.
- [16] J. S. Renken, J. J. Herman, T. R. Bradshaw, P. S. Market, and A. R. Lupo, "The utility of the bering sea and east asia rules in long-range forecasting," *Advances in Meteorology*, vol. 2017, Article ID 1765428, pp. 1–14, 2017.
- [17] J. M. Wiedenmann, A. R. Lupo, I. I. Mokhov, and E. A. Tikhonova, "The climatology of blocking anticyclones for the Northern and Southern Hemispheres: block intensity as a diagnostic," *Journal of Climate*, vol. 15, no. 23, pp. 3459–3473, 2002.
- [18] C. L. Berger, A. R. Lupo, P. Browning, M. Bodner, M. D. Chambers, and C. C. Rayburn, "A climatology of northwest Missouri snowfall events: long-term trends and interannual variability," *Physical Geography*, vol. 23, no. 6, pp. 427–448, 2003.
- [19] Center for Ocean and Atmosphere Prediction Studies (COAPS), 2017, <http://coaps.fsu.edu>.
- [20] University of Missouri Blocking Archive, 2017, <http://weather.missouri.edu/gcc>.
- [21] P. Davini, C. Cagnazzo, S. Gualdi, and A. Navarra, "Bidimensional diagnostics, variability, and trends of northern hemisphere blocking," *Journal of Climate*, vol. 25, no. 19, pp. 6496–6509, 2012.
- [22] H. Lejenas and H. Okland, "Characteristics of Northern Hemisphere blocking as determined from a long time series of observational data," *Tellus A: Dynamic Meteorology and Oceanography*, vol. 35, no. 5, pp. 350–362, 1983.
- [23] A. Jensen, A. Lupo, I. Mokhov, M. Akperov, and D. Reynolds, "Integrated regional enstrophy and block intensity as a measure of kolmogorov entropy," *Atmosphere*, vol. 8, no. 12, p. 237, 2017.
- [24] J. S. Kastman, P. S. Market, S. M. Rochette, and A. R. Lupo, "Assessing upper tropospheric jet streak proximity using the rossby radius of deformation," *Atmosphere*, vol. 8, no. 1, article no. 2, 2017.
- [25] T.-W. Park, Y. Deng, W. Li, S. Yang, and M. Cai, "Mass footprints of the north pacific atmospheric blocking highs," *Journal of Climate*, vol. 28, no. 12, pp. 4941–4949, 2015.
- [26] E. Atallah, L. F. Bosart, and A. R. Aiyer, "Precipitation distribution associated with landfalling tropical cyclones over the eastern United States," *Monthly Weather Review*, vol. 135, no. 6, pp. 2185–2206, 2007.
- [27] T. J. Galarneau Jr., L. F. Bosart, and R. S. Schumacher, "Predecessor rain events ahead of tropical cyclones," *Monthly Weather Review*, vol. 138, no. 8, pp. 3272–3297, 2010.
- [28] S.-Y. Wang and T.-C. Chen, "The late-spring maximum of rainfall over the U.S. central plains and the role of the low-level jet," *Journal of Climate*, vol. 22, no. 17, pp. 4696–4709, 2009.
- [29] J. L. Pelly and B. J. Hoskins, "A new perspective on blocking," *Journal of the Atmospheric Sciences*, vol. 60, no. 5, pp. 743–755, 2003.
- [30] R. L. Molinari, "Air mass modification over the eastern Gulf of Mexico as a function of surface wind fields and loop current position," *Monthly Weather Review*, vol. 115, no. 3, pp. 646–652, 1986.
- [31] A. Donohoe, J. Marshall, D. Ferreira, and D. Mcgee, "The relationship between ITCZ location and cross-equatorial atmospheric heat transport: From the seasonal cycle to the last glacial maximum," *Journal of Climate*, vol. 26, no. 11, pp. 3597–3618, 2013.
- [32] J. L. Rabinowitz, A. R. Lupo, P. S. Market, and P. E. Guinan, "The relationship between Atmospheric Rivers, HYSPLIT backward trajectories, upper-air soundings and heavy rainfall events in the North-Central Mississippi River Valley. Under Revision," *Hydrological Processes*, December 2017.